NATIONAL AND KAPODISTRIAN UNIVERSITY OF ATHENS

SCHOOL OF SCIENCE

DEPARTMENT OF CHEMISTRY

MASTER'S DEGREE PROGRAM
"PHYSICAL CHEMISTRY"

MASTER'S THESIS

Probing Multinucleon Transfer in ^{40}Ar + ^{64}Ni Collisions at 15 MeV/nucleon

KONSTANTINOS GKATZOGIAS
CHEMIST

ATHENS

FEBRUARY 2025

MASTER'S THESIS

Probing Multinucleon Transfer in $^{40}Ar + ^{64}Ni$ Collisions at 15 MeV/nucleon

KONSTANTINOS A. GKATZOGIAS

A.M.: 7111182200002

SUPERVISING PROFESSOR:
George A. Souliotis, Professor, NKUA

EXAMINATION COMMITTEE

George A. Souliotis, (Professor, Department of Chemistry, NKUA)

Demeter Tzeli, (Associate Professor, Department of Chemistry, NKUA)

Anthoula Chrysa Papageorgiou, (Assistant Professor, Department of Chemistry, NKUA)

DATE OF EXAMNATION 20/02/2025

ABSTRACT

We present a detailed analysis of the mass and the momentum per nucleon distributions of ejectiles from the reaction of a ^{40}Ar beam at 15 MeV/nucleon with a ^{64}Ni target. The experimental data were obtained in a previous work with the MARS separator at the Cyclotron Institute of Texas A&M University. The experimental distributions are compared with two dynamical models, the Deep-Inelastic Transfer (DIT) model and the Constrained Molecular Dynamics (CoMD) model, followed by the de-excitation code GEMINI. Both models describe the experimental data to some extent and further optimization is underway in efforts to deepen our understanding of the mechanisms taking place in the production of exotic neutron-rich nuclides in the Fermi energy regime.

SUBJECT AREA: Heavy-ion Nuclear Reactions

KEYWORDS: Mass Distributions, Momentum Distributions, Peripheral Collisions, Fermi Energy

ΠΕΡΙΛΗΨΗ

Παρουσιάζουμε μια λεπτομερή ανάλυση κατανομών της μάζας και της ορμής ανά νουκλεόνιο των θραυσμάτων που προκύπτουν από την αντίδραση δέσμης ^{40}Ar σε ενέργεια 15 MeV/νουκλεόνιο με στόχο ^{64}Ni. Τα πειραματικά δεδομένα συλλέχθηκαν σε προηγούμενη εργασία της ομάδας μας, χρησιμοποιώντας τον φασματογράφο MARS του Cyclotron Institute του Πανεπιστημίου Texas A&M. Οι πειραματικές κατανομές συγκρίνονται με δύο θεωρικά μοντέλα, το μοντέλο βαθιάς ανελαστικής μεταφοράς (Deep Inelastic Transfer - DIT) και το μοντέλο περιορισμένης μοριακής δυναμικής (Constrained Molecular Dynamics - CoMD), ακολουθούμενο από τον κώδικα αποδιέγερσης GEMINI. Και τα δύο μοντέλα περιγράφουν σε κάποιο βαθμό τα πειραματικά δεδομένα. Παρουσιάζονται συγκρίσεις μεταξύ των μοντέλων και περιγράφεται η διαδικασία βελτιστοποίησης τους σε μια προσπάθεια εμβάθυνσης της κατανόησης των μηχανισμών που λαμβάνουν χώρα κατά την παραγωγή εξωτικών νουκλιδίων πλούσιων σε νετρόνια στην περιοχή ενεργειών Fermi.

ΘΕΜΑΤΙΚΗ ΠΕΡΙΟΧΗ: Πυρηνικές Αντιδράσεις Βαρέων Ιόντων

ΛΕΞΕΙΣ-ΚΛΕΙΔΙΑ: Κατανομές Μαζών, Κατανομές ορμών, Περιφερειακές συγκρούσεις, Ενέργεια Fermi

ACKNOWLEDGEMENTS

I am deeply grateful to my supervisor and mentor, Prof. G.A. Souliotis (Professor of Physical Chemistry, Chemistry Department, National and Kapodistrian University of Athens), for his invaluable guidance, exceptional teaching, and our outstanding collaboration.

I would also like to express my appreciation to my fellow group members – Olga, Stergios, Konstantina, Theodoros, Chryssi, Eirini, and Eleftheria – for their support, excellent teamwork, and the insightful discussions we shared.

Lastly, I would like to thank my family and friends for their support in every step of this journey.

CONTENTS

LIST OF FIGURES

LIST OF TABLES

CHAPTER 1
INTRODUCTION

The scientific importance of nuclear physics, was originally established in the late 19th century with the discovery of radioactivity by Henry Becquerel. This breakthrough, along with other significant milestones in the 20th century – such as J.J. Thomson's identification of the electron in 1897, the development of quantum theory in the 1920s, James Chadwick's discovery of the neutron in 1932, and the Bethe-Weizsäcker semi-empirical formula in 1935 – lead to the rapid expansion of the field. Today, nuclear physics is regarded as a foundation of modern research, addressing key questions related to nuclear structure, cosmology, astrophysics, and the synthesis of chemical elements in the cosmos.

An impressive accomplishment in nuclear physics is the synthesis, isolation, and analysis of the properties of approximately half of the ~ 7,000 theoretically predicted nuclei. A key focus is the study of nuclei far from the valley of nuclear stability, near the boundaries of the nuclide chart, also known as nuclear drip lines. Nuclei within the region of nuclear stability are mostly stable and naturally abundant. However, as we move toward the drip lines, nuclei become unstable, exhibiting unique properties that depend on their position in the nuclide chart. The two theoretical drip lines are the proton drip line and the neutron drip line [1]. These drip lines represent regions where the addition of another nucleon (proton or neutron, respectively) cannot lead to a bound system. These boundaries occur through theoretical calculations. The drip lines can be clearly seen in the chart of nuclides in Figure 1.

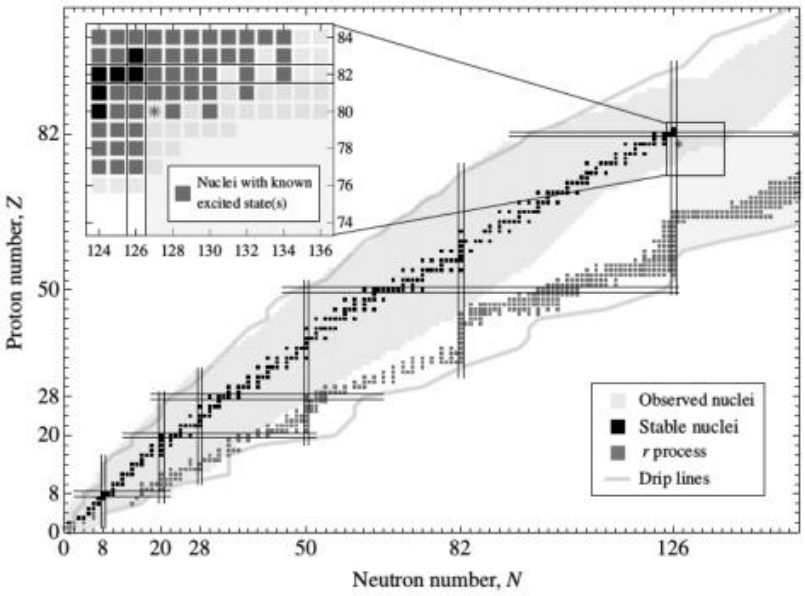

Figure 1: Chart of nuclides [*2*].

In Figure 1, one can observe the fact that most neutron-deficient nuclei, near the proton drip line, have been extensively synthesized and studied. However, the same level of research has not been achieved for neutron-rich nuclei. Investigating nuclei near the neutron drip line is a key focus of nuclear physics research, as it can provide valuable insight into changes in nuclear structure and properties as the N/Z ratio (where N is the number of neutrons and Z is the number of protons) increases. Furthermore, neutron-rich nuclei are of great importance due to their involvement in nucleosynthetic processes in the stars, such as the r-process [3,4].

The r-process, or rapid neutron capture process, is responsible for synthesizing most nuclei heavier than iron, particularly the very neutron-rich isotopes of heavy elements. According to the Canonical r-process model (CAR) [5], events with extremely high neutron density ($Nn \geq 10^{20}$ neutrons/cm^3), high temperatures ($T \geq 10^9$ K), and very short neutron irradiation times (on the order of a few seconds) can explain the abundance of r-nuclides observed in the solar system.

These conditions however require the presence of nuclei far on the neutron-rich side of the valley of nuclear stability, where typical neutron separation energies are around 2 – 3 MeV. Such conditions are met in astrophysical events like supernovae and neutron star mergers [6]. In these environments, the high temperatures produce high-energy gamma-ray photons, which cause a process known as photodisintegration. During this process, nuclei lose particles, such as neutrons, due to irradiation by these photons.

In the r-process, the sequence begins with a relatively light nucleus, such as one in the iron region, undergoing rapid neutron capture to form neutron-rich nuclei. This process continues until the newly formed nucleus becomes so unstable that it undergoes beta decay, before capturing additional neutrons. This marks the final stage of the process, referred to as freeze-out.

Reactions involving n-rich nuclei provide valuable insights into the role of isospin (the N/Z ratio) in the equation of state for asymmetric nuclear matter [7 – 9]. This is crucial for studying objects like neutron stars, which are primarily composed of neutrons. For example, statistical mechanics models have been used to investigate the distribution of nuclear energy levels [10].

A significant advancement in nuclear science is the use of exotic nuclei as beams, a field that has seen rapid development in recent years. This approach enables the study of radioactive projectiles with energies exceeding the Coulomb barrier, despite challenges such as extremely low production cross-sections, the need to separate numerous by-products, and the short half-lives of these nuclei, which make handling them difficult.

Nevertheless, the scientific community has successfully established two major methods for producing radioactive ion beams (RIBs): the Isotope Separation On-Line (ISOL) method and the in-flight method. These techniques allow for the rapid and selective transport of the desired nuclide from its production site to the experimental setup [11].

This work focuses on studying the yields, momentum distributions, angular distributions and excitation energy distributions of projectile-like fragments produced from the reaction of a ^{40}Ar beam with a ^{64}Ni target at 15 MeV/nucleon. The experimental data discussed

were obtained in a previous study using the MARS separator at the Cyclotron Institute of Texas A&M University.

The thesis is structured into six chapters. The next chapter introduces fundamental concepts related to nuclear structure and reactions. Chapter 3 provides a brief overview of the experimental setup and procedures used for data collection. Chapter 4 presents the theoretical models applied in the analysis. In Chapter 5, the results and comparisons of experimental data and theoretical calculations are discussed. Finally, the thesis concludes with a summary and the conclusions derived from the study.

CHAPTER 2
THEORETICAL CONCENPTS

2.1: Nuclear Properties

In this chapter we will discuss the general properties of nuclei. A very large number of nuclei have been studied over the years and the general size, shape, mass and relative stability of these nuclei follow patterns that can be understood by two complementary models of nuclear structure. The average size and stability of a nucleus can be described by the average binding of nucleons together in a macroscopic model, while the detailed energy levels and decay properties can be understood with a quantum mechanical or microscopic model. In this chapter, a brief review of some quantities is given to help understand and interpret the experimental data.

2.1.1: Binding energy and semi-empirical mass equation

Various classical and quantum mechanical models have been proposed to describe the structure of a nucleus. These include the Fermi gas model, the shell model and the liquid drop model. The latter is a classical model, in which the nucleus is described as a set of particles interacting with each other through short-range forces and behaving like molecules in a liquid drop. The key quantity in this model is the binding energy (BE), which is defined as the energy required to separate the nucleus into its individual nucleons and is given by the formula:

$$\mathrm{BE(A,Z)} = \left[\mathrm{Zm_p} + \mathrm{Zm_e} + \mathrm{Nm_n} - \mathrm{M(A,Z)}\right]\mathrm{c}^2 \qquad (2.1)$$

where m_p, m_n, m_e are the masses of the proton, neutron and electron, respectively, and M (A, Z) is the mass of a nucleus with atomic number Z and mass number A. The binding energy can be calculated using the Bethe-Weizsäcker semi-empirical mass equation as follows:

$$\mathrm{BE(A,Z)} = \mathrm{a_v A} - \alpha_s \mathrm{A}^{\frac{2}{3}} - \mathrm{a_c}\frac{\mathrm{Z}^2}{\mathrm{A}^{\frac{1}{3}}} - \mathrm{a_\alpha}\frac{(\mathrm{A}-2\mathrm{Z})^2}{\mathrm{A}} \pm \delta(\mathrm{A}) \qquad (2.2)$$

For nuclei with even N, Z, δ(A) takes the value $+\frac{\alpha_p}{A^{1/2}}$, for nuclei with odd N, Z it takes the value $-\frac{\alpha_p}{A^{1/2}}$, while for nuclei with odd A it equals zero.

A recent set of coefficient values are α_v = 15.753 MeV, α_s = 17.804 MeV, α_c = 0.72 MeV, α_α = 23.69 MeV and α_p = 11.0 MeV. These constants have been derived experimentally using an extensive database of nuclear masses.

Each term has a different origin, resulting from the interactions that determine the shape and properties of the nucleus. The physical meaning of the terms is as follows:

i. Volume term

Each of the nucleons in the nucleus interacts with its surrounding nucleons through the strong nuclear interaction. This term contributes positively to the binding energy.

ii. Surface term

Nucleons on the surface of the nucleus do not interact with the same number of nucleons as the inner nucleons and therefore contribute less to the binding energy. The surface area of a nucleus is equal to $S = 4\pi R^2$, with $R = r_0 A^{1/3}$, so the term to be subtracted is proportional to $A^{2/3}$.

iii. Coulomb term

This term expresses the destabilizing contribution of the Coulomb repulsive force between positively charged protons. For a homogeneous sphere, the Coulomb energy is equal to $E_c = \frac{3}{5}\frac{e^2}{4\pi\varepsilon_0}\frac{Z^2}{R}$. Substituting $R = r_0 A^{1/3}$, it follows that $E_c = \frac{Z^2}{A^{1/3}} a_c$.

iv. Asymmetry term

This term has quantum mechanical origin and reflects the reduced binding energy of nuclei where N ≠ Z ≠ A/2 compared to symmetric nuclei (N = Z). Protons and neutrons are fermions and therefore follow Pauli's exclusion principle, according to which two fermions with the same quantum numbers cannot coexist in the same orbital. Considering that nucleons are distributed in specific energy states in pairs with opposite spin, obeying Pauli's exclusion principle, we observe that in the case where N ≠ Z, the maximum energy state in which one kind of nucleon will be in will be higher than the other. This occurs since the extra nucleons will occupy higher energy states destabilizing the nucleus, relative to the one with N = Z.

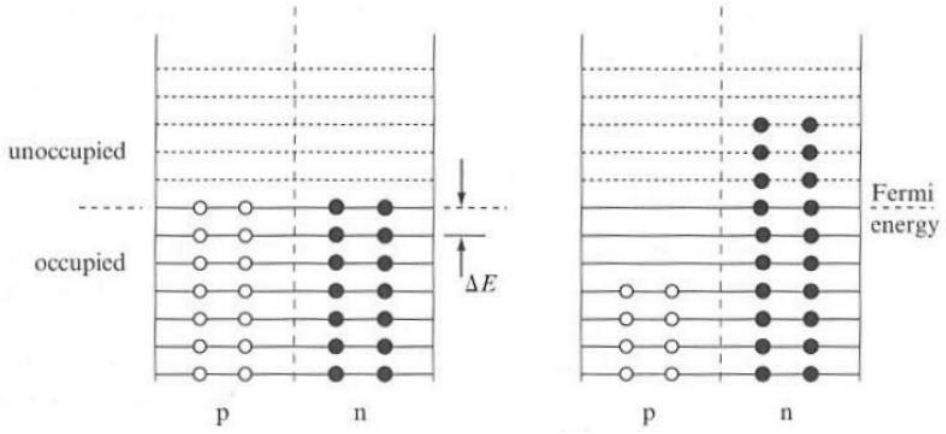

Figure 2: Distribution of nucleons in energy levels for N = Z and N > Z.

v. Pairing term

The latter term also has quantum mechanical origins and represents the stability of a nucleus and its dependence on the coupling of nucleons. Nucleons in an energy state tend to couple in pairs of zero spin. The pairing contribution is positive when the proton and neutron numbers are even, and hence all nucleons are coupled together, negative when both N, Z are odd, and zero when only one of the two is even. Of the stable nuclei, the largest proportion are even-even followed by even-odd, while only four odd-odd nuclei are stable.

An important quantity for the nucleus is the binding energy per nucleon:

$$\frac{\mathrm{BE(A,Z)}}{\mathrm{A}} \tag{2.3}$$

The higher the binding energy per nucleon for a nucleus, the more stable the nucleus is. The most stable nuclei are in the region with Z ~ 28 and A ~ 60. The lighter nuclei can approach this stable region by fusion processes while the heavier nuclei can approach this stable region by radioactive decay or fission processes. Figure 3 represents various values of binding energy per nucleon with respect to mass number. The shape of the diagram is due to the short range of the strong nuclear interaction and the increase in the Coulomb energy contribution as the number of protons in heavier nuclei increases.

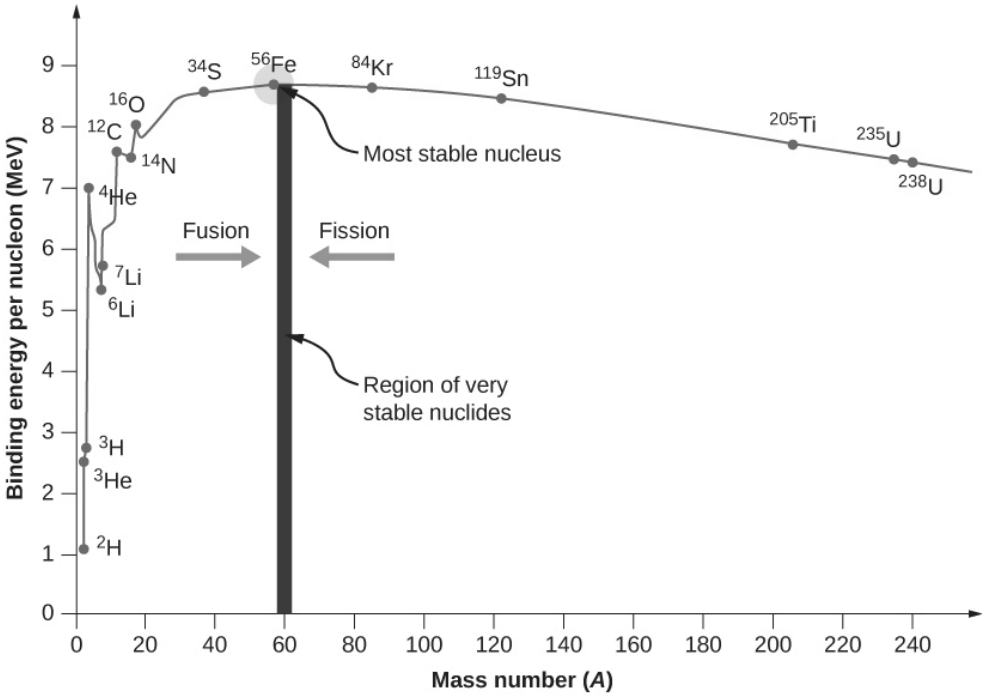

Figure 3: Binding energy per nucleon versus mass number [12].

2.1.2: Q-value

We consider the nuclear reaction p + T → R + x, where the projectile nucleus, p, collides with the stationary target nucleus, T, and after the collision a projectile-like fragment x (quasi-projectile) is created which is emitted at an angle θ, as shown in Figure 4. The remaining target-like fragment (quasi-target) R is emitted at an angle φ.

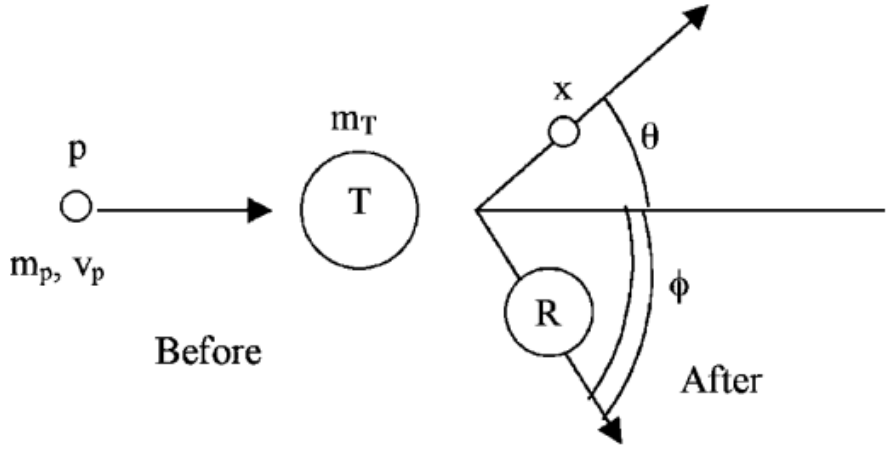

Figure 4: Schematic diagram of the kinematics in a two-body nuclear reaction [13].

where m_i and v_i are the mass and velocity of the i^{th} species.

Because of the principle of conservation of energy, we get

$$\left(m_p c^2 + T_p\right) + \left(m_T c^2 + T_T\right) = \left(m_R c^2 + T_R\right) + \left(m_x c^2 + T_x\right) \tag{2.4}$$

where T_i are the kinetic energies of the particles and m_i are their masses. We define the Q_{value} of the reaction as the difference between the total mass of reactants and products.

$$Q = \left(m_{initial} - m_{final}\right)c^2 \tag{2.5}$$

Incorporating the relation of the energy conservation principle into the definition of Q_{value} yields:

$$Q = \Delta T = T_{final} - T_{initial} \tag{2.6}$$

Since Q is equal to the difference between the kinetic energy of products and reactants, it follows that for exothermic reactions Q > 0, while for endothermic reactions Q < 0. From the conservation of momentum, we have:

$$\mathbf{p_p} = \mathbf{p_x} + \mathbf{p_R}$$

On the x-axis: $m_p v_p = m_x v_x \cos\theta + m_R v_R \cos\varphi$

On the y-axis: $0 = m_x v_x \sin\theta + m_R v_R \sin\varphi$

Combining the above relations with the definition of Q_{value}, we obtain the Q equation:

$$Q = T_x\left(1 + \frac{m_x}{m_R}\right) - T_p\left(1 + \frac{m_p}{m_R}\right) - 2\sqrt{\frac{m_p}{m_R}\frac{m_x}{m_R}T_pT_x}\cos\theta \tag{2.7}$$

From the calculation of the Q_{value}, the excitation energy of the system during the reaction can be calculated.

$$E^* = Q_{gg} - Q \tag{2.8}$$

The ground state to ground state Q_{value} (Q_{gg}) represents the value that Q would have if it was calculated with the masses of the ground states of the products. The final products of the reaction share the total excitation energy by following one of the following two options. The first is to share E* equally among the products.

$$E_x = E_R = {}^{E^*}/_2 \tag{2.9}$$

The other option for sharing the excitation energy depends on the mass of the product in each case and is called thermal sharing [14].

$$E_x = E^*\frac{A_x}{A_x + A_R} \tag{2.10}$$

2.1.3: Cross Section

One of the most important quantities in the study of nuclear reactions is the cross section. The cross section is defined as the probability of a reaction taking place and is calculated according to the following relation:

$$P = n\sigma x \tag{2.11}$$

where P is the probability of the reaction, n is the number of nuclei per unit volume, σ is the cross section and x is the thickness of the target. The cross section has units of surface area and is measured in barn (1 barn = 100 fm^2).

The fragments resulting from the projectile-target reaction are emitted at specific angles. For this reason, we refer to the differential cross section dσ/dΩ, where dΩ is the solid angle in which the products are detected.

$$\frac{d\sigma}{d\Omega} = \frac{dP}{d\Omega}\frac{1}{nx} \tag{2.12}$$

The double differential cross section in terms of angle and energy is defined as follows:

$$\frac{d^2\sigma}{d\Omega dE} = \frac{d^2P}{d\Omega dE}\frac{1}{nx} \tag{2.13}$$

We can also calculate the geometric cross section, from which we can derive the probability of the reaction taking place in cases where the energy of the beam is large enough so that we may ignore the Coulomb repulsion.

$$\sigma = \pi R^2 \tag{2.14}$$

where R is the sum of the radii of the two nuclei.

2.1.4: Grazing angle

The purpose of this study is to examine peripheral reactions. Therefore, the products of interest are those emitted at angles close to the grazing angle. The impact parameter of the reaction is defined as b, which is the vertical distance between the two nuclei. Schematic diagram of a grazing collision (high energy case, no Coulomb deflection).

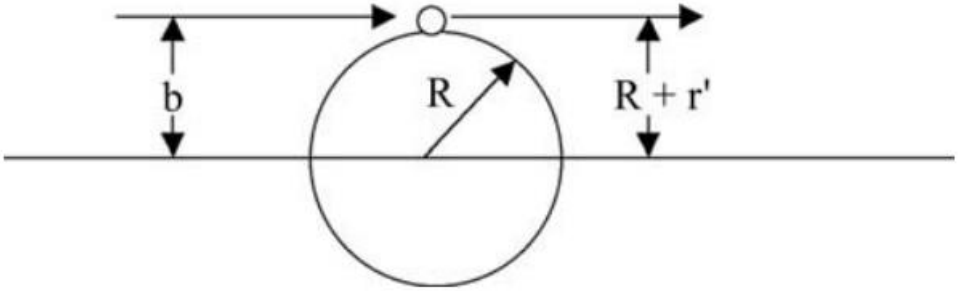

Figure 5: Schematic diagram of a grazing collision (high energy case, no Coulomb deflection).

The minimum distance between the two nuclei during the collision is denoted as r_{min}. For Coulomb scattering, considering the principle of conservation of energy and angular momentum, the following expression for r_{min} is obtained:

$$r_{min} = \frac{e^2 Z_1 Z_2}{4\pi\varepsilon_0}\frac{1}{2T}\left[1 + \frac{1}{\sin\left(\frac{\theta}{2}\right)}\right] \tag{2.15}$$

where T is the initial kinetic energy of the projectile, and θ is the scattering angle, which will be equal to the contact angle if r_{min} equals the sum of the radii.

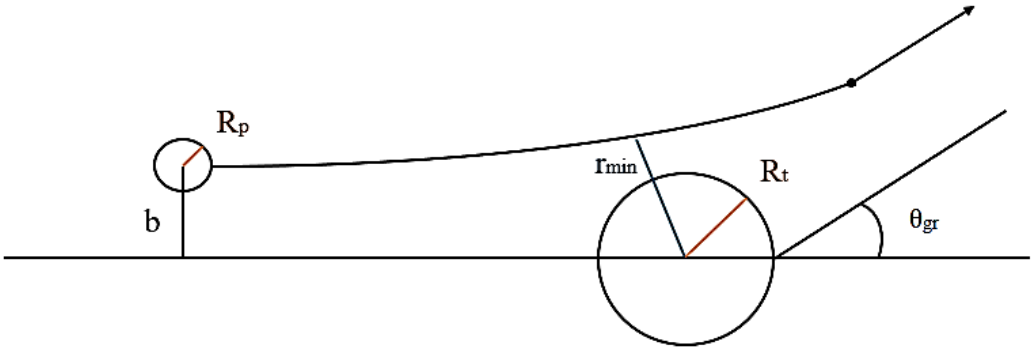

Figure 6: Schematic diagram of a grazing collision in which Coulomb scattering occurs.

2.2: Nuclear Reaction Mechanisms

Nuclear reactions can be divided by their energy into low (< 20 MeV/nucleon), medium (20 – 200 MeV/nucleon) and high energy reactions (> 200 MeV/nucleon). At low energies, the main interaction between nuclei is the average potential between neighboring nucleons. At high energies, on the other hand, the interaction between nucleons plays a more important role. The present work deals with low energy reactions well above the Coulomb barrier energy. These reactions are further categorized by means of the interaction distance between the two nuclei, i.e. the impact parameter b. Figure 7 shows the different mechanisms that can take place depending on this parameter. Some of them are briefly discussed below θ = 4°.

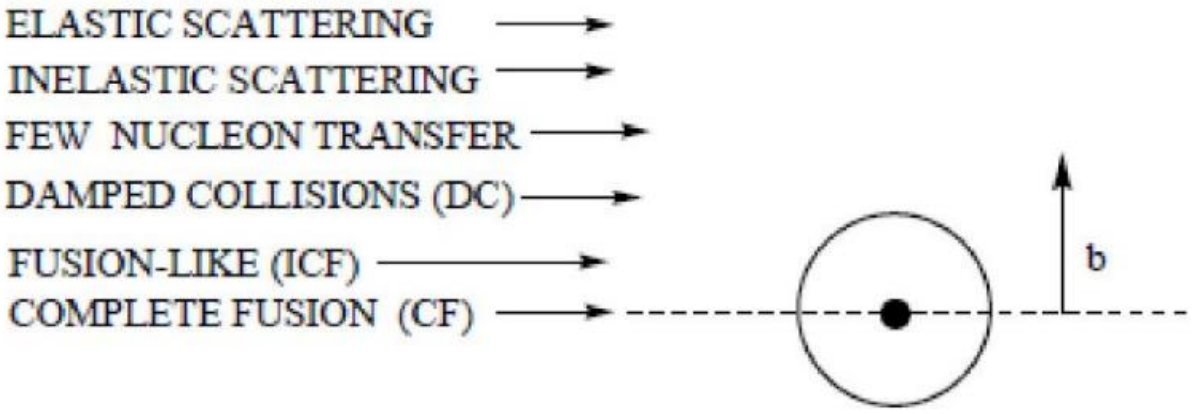

Figure 7: Nuclear reactions for different values of the impact parameter b.

2.2.1: Elastic scattering

In peripheral collisions with large values for the impact parameter, elastic scattering takes place. During elastic scattering, only Coulomb interactions are acting on the system, resulting in the conservation of the kinetic energy of the nuclei, as well as their atomic and mass numbers. In this case, the projectile can be observed to deflect at some angle, which depends on the Coulomb repulsion between the nuclei.

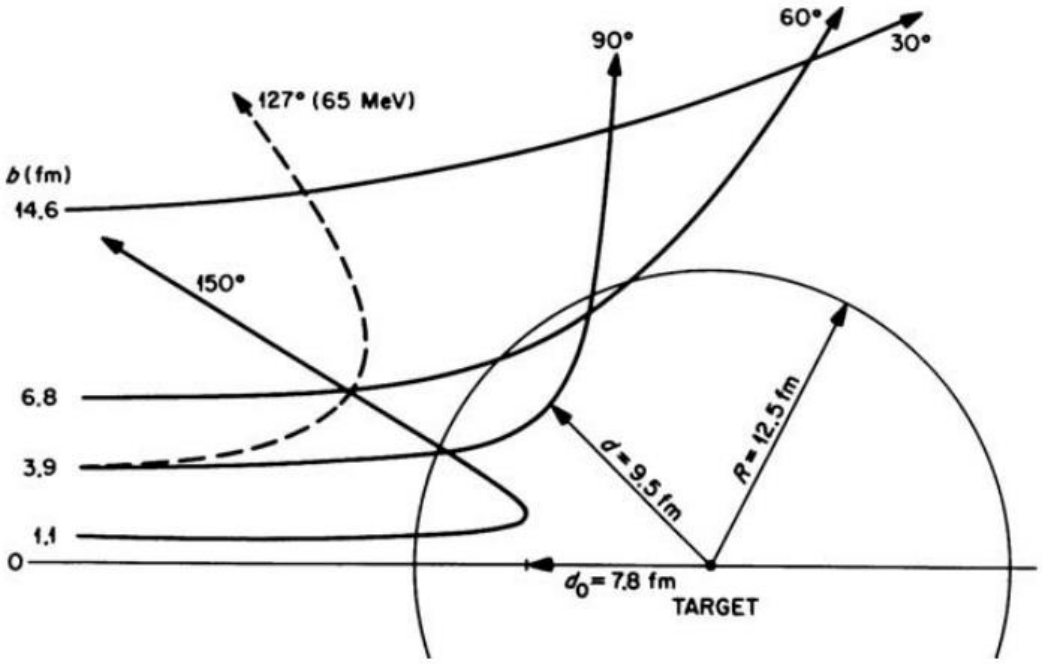

Figure 8: Schematic depiction of some representative projectile trajectories for the ^{16}O interaction with ^{208}Pb at 30 MeV.

2.2.2: Direct reactions

A different type of nuclear reactions, for smaller values of the impact parameter b, are direct reactions. These reactions occur when the nuclei interact through their surfaces and the time required for this interaction is equal to the time it would take the projectile to pass the target. In the case of heavy ions, the reactions are considered quasi-elastic. The products of such reactions occur at low excitation energies. These reactions are of particular importance because they provide important information about the structure of the nucleus.

Direct reactions can be divided into inelastic reactions and nucleon transfer reactions. In inelastic reactions, no nucleon transfer occurs during the reaction, but the kinetic energy of the projectile is not kept constant, and the resulting products are excited. Nucleon transfer reactions occur at lower values of the impact parameter, where the nuclei are

overlapping. In this case, either pick-up or removal, take place. In Figure 9, a neutron pick-up reaction is illustrated.

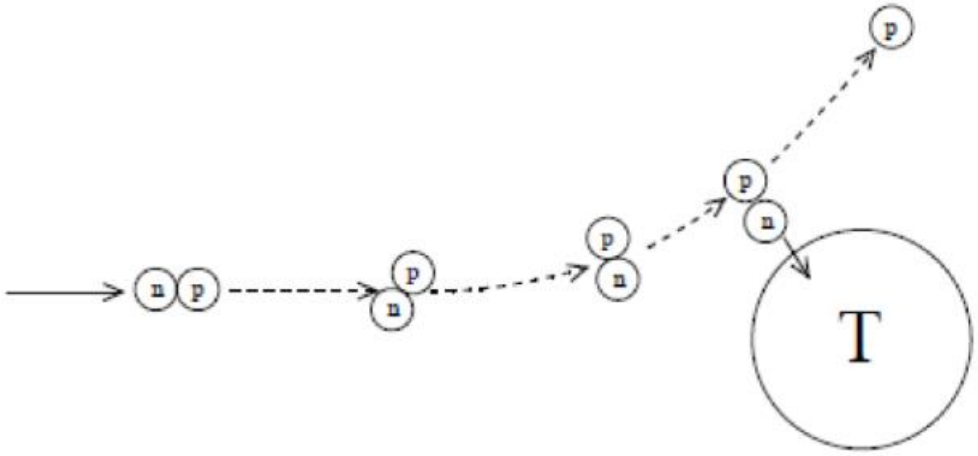

Figure 9: Neutron transfer reaction from the projectile to the target.

2.2.3: Deep inelastic transfer

Full inelastic collisions or multinucleon transfer reactions take place when the collision parameter takes intermediate values (semi-peripheral and peripheral collisions), and the overlap of nuclei is relatively large to the point of competing with Coulomb repulsion. By balancing the two forces, it is possible to create a di-nuclear target-projectile system.

The lifetime of these di-nuclear systems is sufficient to rotate through some angle and transfer nucleons, energy and momentum. During the rotation of the nuclear system, the ions rotate as a single entity. The angular momentum is large enough to prevent fusion, so they separate with kinetic energy that depends on their angular momentum, gaining additional kinetic energy due to Coulomb repulsion. Much of the kinetic energy is converted into excitation energy through nucleon collisions and mass transfer, so that the fragments appear with a significant energy reduction. The smaller the impact parameter, the longer the rotation time, thus enhancing nucleon transfer. This transfer is achieved through a "window" that opens between nuclei when they are at nuclear interaction distances, as shown in Figure 10. After the transfer, a wide variety of fragments with masses similar to those of the projectile and target are produced, the so-called quasi-projectile and quasi-target fragments, respectively. This phenomenon provides the possibility to produce and study a plethora of exotic isotopes far from the valley of stability.

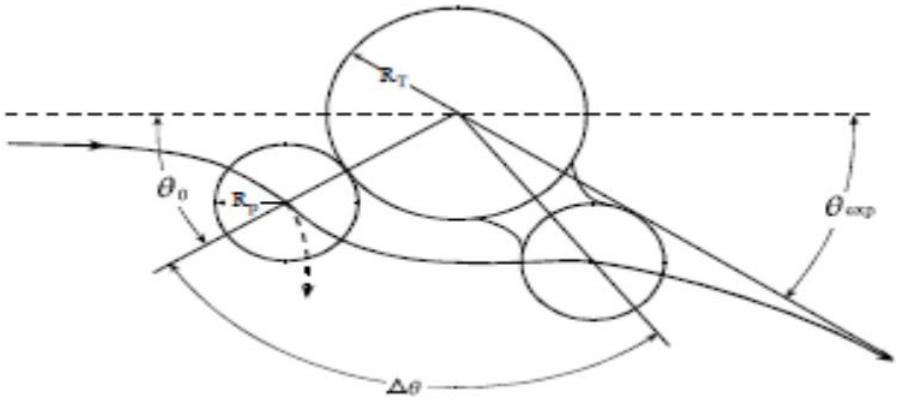

Figure 10: Schematic illustration of rotation of the di-nuclear system in a deep inelastic collision.

2.2.4: Projectile Fragmentation

Projectile fragmentation is a type of reaction that takes place in high-energy peripheral collisions. This process can be broken down into two stages. In the first stage, a projectile and target collision occurs within a time range of 10^{-23} s. During this stage, primary fragments are produced which exhibit high excitation energies. The second stage involves the de-excitation of the excited primary fragments through the emission of nucleons, light nuclei or gamma rays. The de-excitation stage may last from 10^{-18} s to 10^{-20} s.

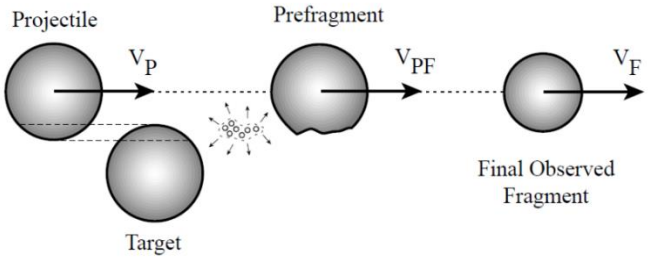

Figure 11: Illustration of projectile fragmentation reaction.

CHAPTER 3
EXPERIMENTAL SETUP

Reactions that occur through nucleon exchange mechanisms take place at low energies, ranging between the Coulomb barrier [15] and the Fermi energy (10 – 40 MeV/nucleon) [16,17]. The energy range in which the reactions studied in this paper take place is the 15 – 25 MeV/nucleon region. In this energy range, close to the Fermi energy, the N/Z ratio of the fragments produced is enhanced, as they also have sufficiently high velocities to achieve effective separation in magnetic spectrometers.

The experimental setup in which the experiment took place is the MARS spectrometer [18], located at the Cyclotron Institute at Texas A&M University. Through this experimental setup, the products of the ^{40}Ar + ^{64}Ni reaction at the energy of 15 MeV/A were collected and identified [14,19,20].

3.1: Description of the MARS Spectrometer

In the first stage, the acceleration of the beam takes place. The ion beam was produced by an ECR (Electron Cyclotron Resonance) ion source and accelerated by the superconducting K500 cyclotron until it reached the appropriate energy (15 MeV/nucleon). The ^{40}Ar beam was then directed to a 2 mg/cm^2 thick ^{64}Ni target and then to the spectrometer.

The MARS spectrometer is equipped with magnetic quadrupoles, Q_i, for focusing the beam and magnetic dipoles, D_i, for separating the fragments. After the beam interacts with the target, the fragments produced pass through two magnetic quadrupoles to be focused and a magnetic dipole, where horizontal dispersion is obtained.

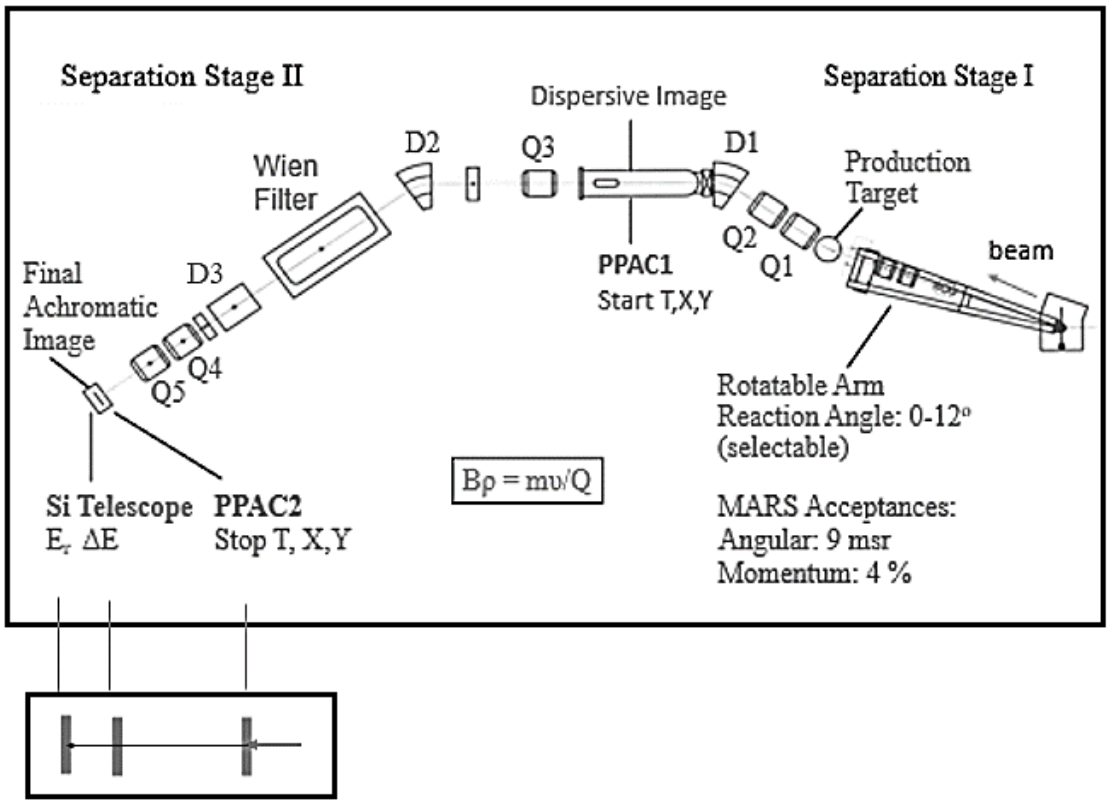

Figure 12: Schematic representation of the MARS spectrometer [21].

The K500 cyclotron is a circular accelerator, where particles move in circular orbits with the help of a constant magnetic field and pass in an iterative manner through the same acceleration space, maintaining a constant frequency. In cyclotrons there are only two electrodes to achieve high potentials as opposed to linear accelerators which required a significantly larger number. These electrodes are semi-circular in shape reminiscent of the English letter D; hence they are called 'dees'. The dees are closely spaced, with the space in between being under high vacuum conditions. The electrodes are activated by means of an alternating voltage source of frequency, v_{cyc}, in resonance with the frequency of the ions. Entering the electrodes, the ions move in circular orbits under the influence of the constant magnetic field, B. Subsequently, they enter the accelerating space, accelerate, and acquire more energy, and subsequently follow an orbit of greater radius. This is done in an iterative manner, up to the limiting value R, determined by the size of the electrodes [22]. At this point, the beam has reached its maximum energy value and is transferred to the experimental set-up. The notation K500 on the cyclotrons is characteristic of the apparatus and refers to K = 500 with K being the following quantity:

$$\mathrm{K} = \frac{(\mathrm{B}\rho)^2}{2\mathrm{m_n}} \tag{3.1}$$

where m_n = 931.5 MeV/c and the quantity Bρ is called magnetic rigidity, as will be discussed below. K is an important quantity as the value of the beam energy depends directly on this parameter:

$$\left(\frac{E}{A}\right)_{max} = K\left(\frac{q}{A}\right)^2 \tag{3.2}$$

where q is the charge of the ions and A is their mass number. We mention here that the spectrometer arm is used so that the beam strikes the target at the desired angle, in our case at 4° relative to the optical axis of the spectrometer.

The products produced by the beam-target reaction pass through two quadrupoles Q1 and Q2 to be focused and then through the magnetic dipole D1 where they are separated. The magnetic dipoles Di bend the trajectory of the fragments passing through them, as the magnetic field inside them is perpendicular to the axis of motion. In addition, the spectrometer is equipped with a Wien filter, which rejects any fragments that have a velocity outside the specified range. The maximum angular acceptance of the spectrograph is 9 msr and the momentum acceptance is 4%. Also, an aluminum foil with a surface density of 1 mg/cm^2 is placed at the entrance of the Q1 quadrupole. Its role is to re-equilibrate the charge of the ionic states of the reaction products. In front of the quadrupole Q1, and at 31.5 m from the target, there is a 2×2 cm window defining a horizontal angular acceptance of Δθ = 3.6° (±1.8°) and a corresponding vertical Δφ = 3.6°. This establishes a permissible solid angle ΔΩ = 4 msr. For the reaction studied in this work, the beam of ^{40}Ar ions collided with the target at an angle of 4°, as we mentioned, with respect to the optical axis, thus the products were collected over a polar angle range of 2.2° – 5.8°. This follows from the definition of a solid angle, according to which:

$$\Delta\Omega = \frac{\Delta S}{R^2} \tag{3.3}$$

$$\Delta\Omega = \frac{2 \times 2\ \text{cm}^2}{31.5\ \text{cm}^2} \tag{3.4}$$

$$\Delta\Omega = 4.03 \times 10^{-3}\ \text{srad} \approx 4\ \text{msr} \tag{3.5}$$

The beam ions that did not interact with the target ended up in a Faraday cup that provided the measurement of the beam current.

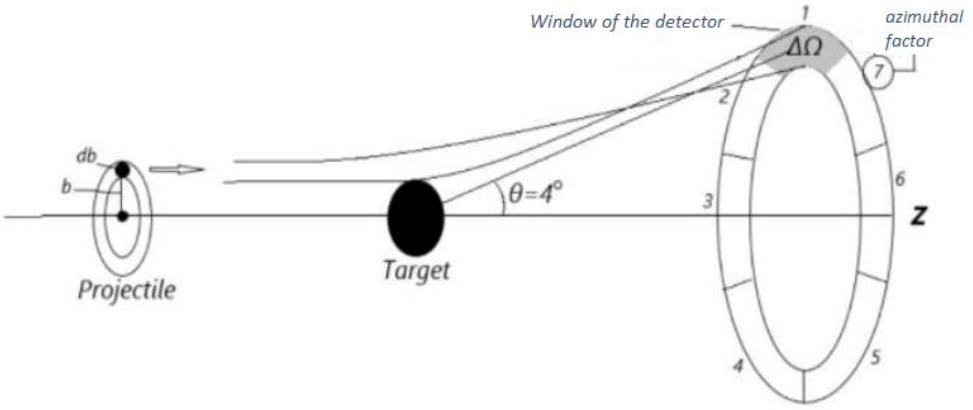

Figure 13: Collision between projectile and target. Detection of products at an angle of θ = 4°, detection window ΔΩ = 4 msr.

In the following section, we briefly review the principle of magnetic spectrometry. Fragments passing through a magnetic dipole are subjected to a Lorentz force, which has a magnitude of:

$$F = qvB \tag{3.6}$$

where q is the charge, v is the velocity of the fragment and B is the intensity of the magnetic field. Since the motion of the fragments of mass m is circular with radius ρ, there is also a centripetal force F_c equal to:

$$F_c = \frac{mv^2}{\rho} \tag{3.7}$$

Since the magnetic force will also be centripetal, equating relations (3.5) and (3.6), yields the fundamental relation of magnetic spectrometry, in which the term Bρ is called the magnetic rigidity (with unit 1 Tesla·m):

$$qvB = \frac{mv^2}{\rho} \tag{3.7}$$

Consequently:

$$B\rho = \frac{mv}{q} = \frac{P}{q} \tag{3.8}$$

and equivalently:

$$B\rho = \left(\frac{P}{A}\right)\left(\frac{A}{q}\right) \tag{3.9}$$

The radius of curvature of the trajectory that each fragment will traverse is proportional to the ratio A/q, so if the fragment velocity and the trajectory radius are known, then for a

given magnetic field strength, separation of the fragments can be achieved, according to A/q.

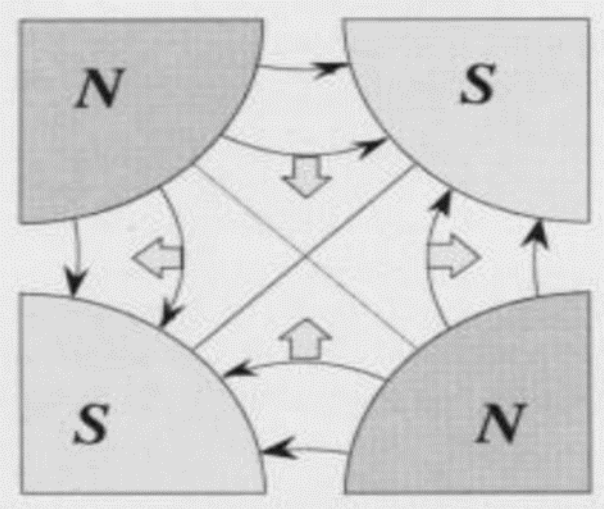

Figure 14: Schematic representation of the magnetic quadrupole. The magnetic quadrupole consists of two opposite north and two opposite south magnetic poles. The formed magnetic field focuses the beam at its center in one direction and defocuses the beam in the other direction.

The detectors are located in the dispersive image plane and the achromatic image plane at the end of the setup. More specifically, the first of the two parallel plate avalanche counters (PPAC) is located in the dispersive image [23]. Such detectors provide information on the position of the fragments on the x, y (z is the beam axis) axes, i.e., the radius of their trajectory, and through this the magnetic rigidity. Furthermore, the speed of the fragments can also be measured by measuring the time of flight (TOF) between two such detectors, where the first PPAC gives the start signal and the second, located in the final achromatic image, gives the stop signal. Thus, knowing the time (usually a few hundred ns) and the distance between them (13 m), the speed of the fragment of interest can be calculated.

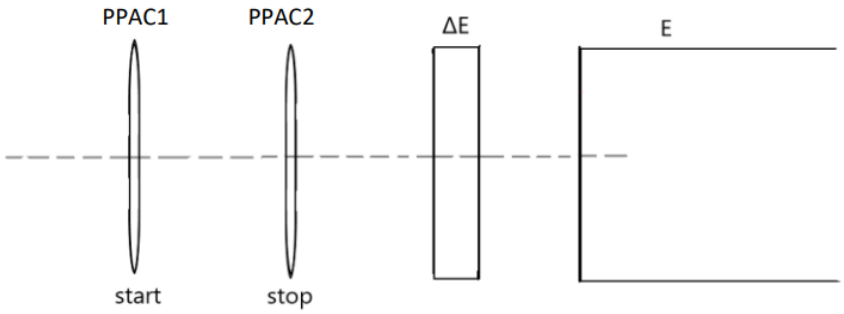

Figure 15: Schematic TOF time measurement device.

After passing through the two PPAC detectors, the products pass through the final Focal plane detector detection system, which has dimensions of 5×5 cm. This system consists of two silicon detectors, a thin one, denoted as ΔE (~ 50 μm) and a thick one, denoted as E (1 mm). When the fragments pass through the ΔE detector, their kinetic energy is reduced. The rate of kinetic energy loss depends on the atomic number and the velocity, according to the Bethe-Bloch relation [24 – 26].

$$\frac{dE}{dx} \propto \frac{Z^2}{v^2} \tag{3.10}$$

The fragments then arrive at the detector E, where they stop due to its large thickness and deposit their residual kinetic energy, E_r. Therefore, the total energy of each fragment will be the sum of ΔE and E_r:

$$E = \Delta E + E_r \tag{3.11}$$

Moreover, the total energy (that is the kinetic energy) of the fragment is given by:

$$E = \frac{1}{2} m v^2 \tag{3.12}$$

Combining the above two relations, we obtain:

$$\frac{1}{2} A m_n v^2 = \Delta E + E_r \tag{3.13}$$

$$A = \frac{2(\Delta E + E_r)}{m_n} \tag{3.14}$$

Thus, by finding the energy loss (ΔE) and the residual energy of the fragment (E_r), mass number of the fragment in question can be determined.

Simultaneously, based on relation (3.10), we obtain:

$$Z^2 \propto v^2 dE \Rightarrow Z \propto v\sqrt{dE} \tag{3.15}$$

From relation (3.15), the atomic number of the fragments is determined [24]. Based on the above relation, the atomic number for an event with a given velocity (v) and energy loss (ΔE) is calculated from the following empirical relation:

$$Z = a_0(v) + a_1(v) v\sqrt{dE} + a_2(v)(v\sqrt{dE})^2 \tag{3.16}$$

where $a_0(v)$, $a_1(v)$, $a_2(v)$ are coefficients which depend on the velocity of the fragments and are determined via a procedure described in [17,24].

The mass number of fragments can be obtained in a different way by using the parameter q, i.e. the fragment charge. The charge can be found from the following relation:

$$q = \frac{P}{B\rho} = \frac{mv}{B\rho} \tag{3.17}$$

As the charge must be an integer, finding the integer value q_{int} of each event is done by gating the experimental data. More specifically, a gate of range Δq = 0.4 units is set in the

distribution of the found charge values for each selected magnetic rigidity value in the experiment. Thus, based on relation (3.9) it can be assumed that:

$$\frac{A}{q} = \frac{B\rho}{\left(P/A\right)} \tag{3.18}$$

and the mass number is obtained as:

$$A = \left(\frac{A}{q}\right) q_{int} \, . \tag{3.19}$$

It is worth pointing out that this way of calculating the mass number is more accurate as it is characterised by a resolution of about 0.5% [24].

In order to measure the properties of the nuclei produced, an electron and/or gamma-ray detector may be additionally placed behind the silicon ΔE–E detector, but this apparatus was not used in the measurements above.

The calibration of the spectrometer was performed using low intensity ^{40}Ar and ^{86}Kr beams with an energy of 15 MeV/A at an angle of 0°.

3.3: Cross section

In this chapter, we will present the analytical way of calculating the total cross section in the full angular range where the experiment was conducted (2.2° – 5.8°):

$$\sigma = \int_{2.2^\circ}^{5.8^\circ} \left(\frac{d\sigma}{d\Omega}\right) d\Omega$$

$$\sigma = \int_{2.2^\circ}^{5.8^\circ} \left(\frac{d\sigma}{d\Omega}\right) (2\pi \sin\theta \, d\theta)$$

$$\sigma = \int_{2.2^\circ}^{5.8^\circ} \left(\frac{d\sigma}{d\Omega}\right) (2\pi \sin(4.0^\circ) \, d\theta)$$

however, Δθ = 3.6° therefore:

$$\sigma = \left(\frac{d\sigma}{d\Omega}\right)_{4.0^\circ} \left[2\pi \sin\left(\frac{4.0^\circ}{180^\circ}\right)\left(\frac{3.6^\circ \pi}{180^\circ}\right)\right]$$

$$\sigma = 0.0275 \left(\frac{d\sigma}{d\Omega}\right)_{4.0^\circ} \tag{3.20}$$

where $\left(\frac{d\sigma}{d\Omega}\right)_{4.0^\circ}$, is the differential cross section measured in the experiment at 4°, in units of mb/sr. The derivative $0.0275 \left(\frac{d\sigma}{d\Omega}\right)_{4.0^\circ}$ expresses in turn the cross section which takes into account the azimuthal symmetry of the experiment and refers to the entire circular disk defined by the two angles and units mb. This quantity will be defined as the Measured

Cross Section in our experimental yield data. According to the relation (3.20) converted in units of mb/msr, the total cross section is given by:

$$\sigma = 27.5 \left(\frac{d\sigma}{d\Omega}\right)_{4.0°} \tag{3.21}$$

We can interpret the factor 27.5 as ~ 4 msr × 7, where factor 7 corresponds to the integration over the azimuthal angle of the circular disk of the spectrometer.

Figure 16 illustrates a schematic representation of the angular acceptance windows of the MARS spectrometer. The red square refers to the angle window at 4°, while the circular disk to which the red square belongs refers to the measured cross-section of 4°.

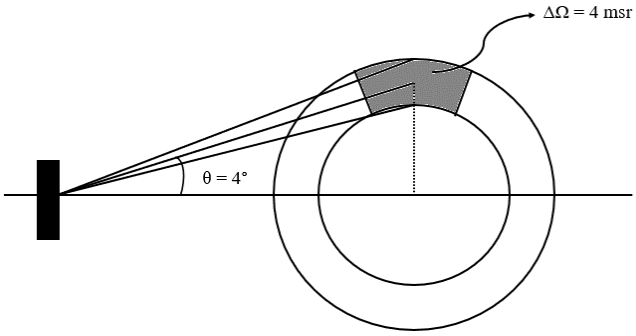

Figure 16: Schematic representation of the angular acceptance windows of the spectrometer, where the 4° window is shown.

CHAPTER 4
DESCRIPTION OF THEORETICAL MODELS

Experimental data and their understanding are essential for advancing our understanding of nuclear processes. Equally important is the development of theoretical models aimed at understanding the mechanisms behind these processes. It is obvious that a continuous effort is being made to optimize these models, to verify their accuracy thoroughly and, consequently, to be able to make predictions for future experiments. The next section provides an overview of the models used in this study. In particular, two models, namely the deep inelastic transfer (DIT) model [27] and the constrained molecular dynamics (CoMD) model [28], were used to describe the dynamical stage of the reaction. After the dynamical phase of the reaction, the deexcitation of the primary fragments was described using the GEMINI statistical deexcitation code [29].

4.1: Complete Inelastic Transfer Model, DIT

4.1.1: General description of the model

One of the models used for the calculations is the Deep Inelastic Transfer model (DIT), by Tassan-Got [27]. DIT is a phenomenological model that describes the stochastic exchange of nucleons in peripheral and semi-peripheral reactions by Monte Carlo method [30]. The target and the projectile are considered as spheres moving in Coulomb orbits until they are in the range of nuclear interaction, where the system can then be described as two Fermi gases in contact.

During this interaction between projectile and target, a 'window' opens in the inter-nuclear potential, within which stochastic nucleon exchange is allowed. In the resulting binuclear system, the relative kinetic energy, due to its gradual energy degradation, is converted into excitation energy of the resulting fragments. The fragments can be excited vibrationally, rotationally, or thermally [31].

The total excitation energy of the fragments can be distributed to the fragments based on the Linear Response Theory. According to this theory, the system is considered as a unit and its variables evolve in interaction with a tank in thermal equilibrium. Consequently, the binuclear system is characterized by a common temperature. Because of this, the excitation energy of the system is distributed among the fragments as a function of their mass. In the DIT model, however, it is assumed that the only possible excitation of the system arises from the exchange of nucleons. It follows that for symmetric flow, the excitation energy of each pair of products will also be symmetric and, consequently, the excitation energy is equally distributed between the products. As mentioned above, the DIT model assumes that the system is energetically degraded only through the process of nucleon exchange, while collisions between nucleons are not considered.

4.1.2: Important quantities

In this chapter, an analysis of the quantities incorporated in this model will be carried out; nucleon donor is considered as nucleon 1 and nucleon acceptor as nucleon 2. In addition, the prime symbol ' will be placed on any quantity that is associated with the system after the nucleon transfer is completed.

Due to the principle of conservation of energy for the system under consideration, the following relationship applies to the respective changes in the different types of energy:

$$\Delta\delta_1 + \Delta\delta_2 + \Delta E_1^* + \Delta E_2^* + \Delta K + \Delta U_{int} = 0 \tag{4.1}$$

where $\Delta\delta_1$, $\Delta\delta_2$ are the changes in the excess mass of the nuclei, ΔE_1^*, ΔE_2^* are the changes in the excitation energies. ΔK is the relative change in kinetic and ΔU_{int} is the relative change in the dynamical energy of the binuclear system.

For the excess mass changes, we consider:

$$\Delta\delta_1 = \delta_1' - \delta_1 = S_1 - \delta_a \tag{4.2}$$

$$\Delta\delta_2 = \delta_2' - \delta_2 = -(S_2' - \delta_a) \tag{4.3}$$

$$\Delta\delta_1 + \Delta\delta_2 = S_1 - S_2' \tag{4.4}$$

where δ_α denotes the excess mass of a transferred nucleon, and S_1 and S_2' are the proton or neutron separation energies for the two nuclei, before and after the nucleon transfer, respectively. The excitation energies of the nuclei can be expressed as follows:

$$\Delta E_1^* = E_1^{*\prime} + E_1^* = \varepsilon_{F1} - \varepsilon_1 \tag{4.5}$$

$$\Delta E_2^* = E_2^{*\prime} + E_2^* = \varepsilon_2 - \varepsilon_{F2}' \tag{4.6}$$

where ε_1 and ε_2 are the kinetic energies of the transferred nucleon in each nucleus and ε_{F1} and ε_{F2} are the Fermi energies of the nuclei. The sum of the Fermi energy with the binding energy equals the potential well depth at infinity, from the relation $S_i + \varepsilon_{Fi} = U_{i\infty}$ therefore holds:

$$\Delta\delta_1 + \Delta\delta_2 = S_1 - S_2' = (\varepsilon_{F1} - \varepsilon_{F2}') + (U_{2\infty} - U_{1\infty}) \tag{4.7}$$

Using this relation in (4.1) it follows:

$$\Delta K = -\Delta U_{int} - (\varepsilon_2 - \varepsilon_1) + (U_{2\infty} - U_{1\infty}) \tag{4.8}$$

where ΔK is the relative change in kinetic energy and ΔU_{int} is the relative change in dynamic energy of the binuclear system.

By requiring the wells of the two nuclei to be isobaric it follows that:

$$\Delta K = -\Delta U_{int} - (\varepsilon_2 - \varepsilon_1) \tag{4.9}$$

In the DIT model, the potential energy change ΔU_{int} takes a zero value when the nucleon being transferred is a neutron and a non-zero value when it is a proton. This occurs since, in the case of proton transfer, the Coulomb interaction is considered. For the case where neutron transfer takes place, $\Delta U_{int} \approx 0$.

This leads to the formula:

$$\varepsilon_2 = \varepsilon_{02} - \Delta U_{\text{int}} \tag{4.10}$$

where ε_{02} represents the kinetic energy of the nucleon, if $\Delta U_{\text{int}} \approx 0$.

The change in dynamic energy is given by:

$$\Delta U_{\text{int}} = 1.44 \frac{Z_1 - Z_2 - 1}{d} \tag{4.11}$$

where d is the distance between nuclei in fm.

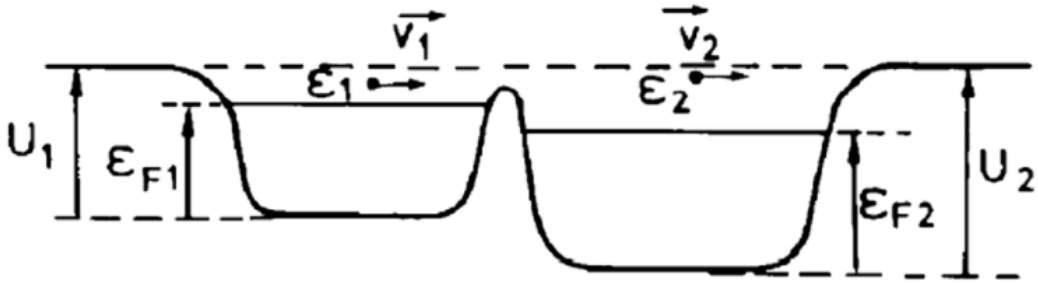

Figure 17: Schematic representation of the potentials for nuclei 1 and 2 [9].

The y-axis is the axis of the beam. Therefore, the only component of angular momentum and spin that varies is the z component.

$$\Delta S_1 = -l_1$$

$$\Delta S_2 = l_2$$

$$\Delta L = -(l_2 - l_1) \tag{4.12}$$

where S_1 and S_2 are the spins of the two nuclei, L is the orbital angular momentum, and l_1 and l_2 are the orbital angular momentum of the transferred nucleon in the donor and acceptor nuclei, respectively.

When the projectile is in the range of the nuclear interaction, a "window" opens between the two systems to achieve stochastic nucleon transfer. According to Randrup [32], the velocity of the nucleon when it passes into nucleus 2 will be affected not only by its initial velocity in 1, but also by the relative velocity of the binuclear system. More specifically:

$$\overrightarrow{v_2} = \overrightarrow{v_1} + v_{\text{rel}} \tag{4.13}$$

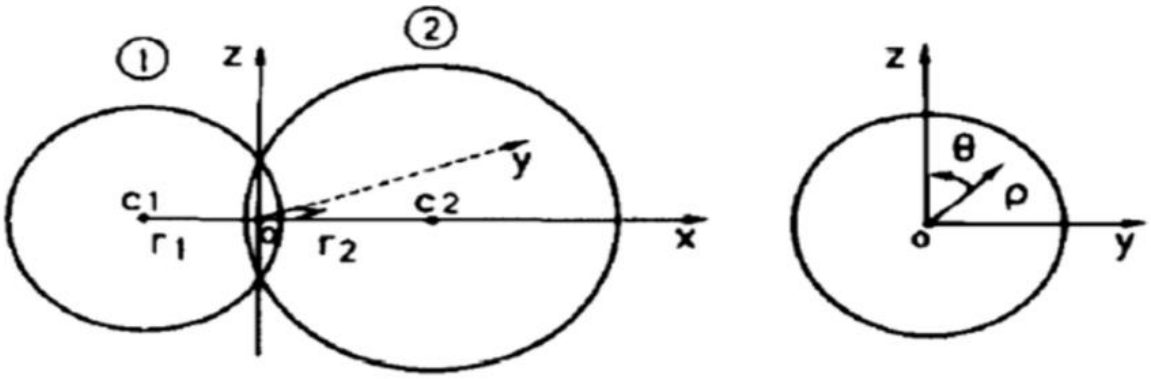

Figure 18: Geometric representation of the binuclear system. The relative velocity of the donor nucleus 1 with respect to the acceptor nucleus 2 is on the xy plane. ρ,θ define the window in which the nucleon transfer takes place.

An important quantity considered in the DIT is the transfer probabilities. The probability of transferring a neutron or proton from nucleus 1 to nucleus 2 is given by the equation:

$$P = \int \Phi T n_1 (1 - n_2) d^5\sigma \tag{4.14}$$

where $d^5\sigma = \rho d\rho d\theta d^3p$, with $(\rho d\rho d\theta)$ the elementary surface in polar coordinates.

Φ is defined as the flux, the number of passing nucleons on a vertical surface per unit of time:

$$\Phi = \frac{dN}{dSdt} \tag{4.15}$$

Multiplying the numerator and denominator by dx gives the following formula, which relates the flow to the Fermi gas density, ρ_F:

$$\Phi = \frac{dN}{dSdx}\frac{dx}{dt} = \rho_F v_x \tag{4.16}$$

As the model considers the phase space, two nucleons will be in an elementary cell of volume h^3.

$$\frac{dN}{dVd^3p} = \frac{2}{h^3} \tag{4.17}$$

$$\rho_F = \frac{2}{h^3} d^3p \tag{4.18}$$

Consequently:

$$\Phi = \rho_F v_x = \frac{2}{h^3} v_x d^3p \tag{4.19}$$

The number of nucleons passing through vertical surface, dS, will be:

$$\Phi dS = \frac{2}{h^3} v_x d^3p dS = \frac{2}{h^3} v_x d^3p \rho d\rho d\theta \tag{4.20}$$

Substituting the flux in relation (4.14) for the nucleon transfer probability, we obtain:

$$P = \int \frac{2}{h^3} v_x \rho T n_1 (1 - n_2)\, d\rho d\theta d^3p \tag{4.21}$$

T represents the barrier transmittance which depends on the potential of the nucleon within the window. This potential will be the sum of the Coulomb and Wood-Saxon potentials. The n_1, n_2 express the probability of occupying an energy level for nuclei 1 and 2 respectively and can be calculated as:

$$n_i = \frac{1}{1 + \exp\left[E_i^* - \varepsilon_{Fi} - \frac{S_i l_i}{\Im})/T_i\right]} \tag{4.22}$$

where $\Im$ is the moment of inertia. The contribution of rotation during excitation of the system is expressed by the term $S_i l_i/\Im$.

The cross-section in the model is calculated, for a given angular momentum l, from the following formula:

$$\sigma_l = \pi \lambda\!\!\!^{-2} (2l + 1) P, \qquad \lambda\!\!\!^{-} = \frac{\hbar}{p} \tag{4.23}$$

For the total cross section:

$$\sigma_{tot} = \pi \lambda\!\!\!^{-2} \sum_{l=0}^{l_{max}} (2l + 1) P \tag{4.24}$$

when the transfer is successful (P=1):

$$\sigma_{tot} = \pi \lambda\!\!\!^{-2} l_{max} \tag{4.25}$$

where l_{max} is the maximum angular momentum value where nucleon transfer can take place.

For each angular momentum value, several events are calculated. These events are distributed equidistantly over the surface of the target, assuming that the target has a circular cross-section perpendicular to the beam axis and by selecting a number of events proportional to the radius of the circle. The radius of the circle will be equal to the impact factor b. The impact parameter will be equal to the sum of the radii of the two nuclei and from this the angular momentum will be obtained according to the relation:

$$b = l \lambda\!\!\!^{-} \tag{4.26}$$

Assuming an equal distribution, the number of events will be proportional to the angular momentum, n(l)= $f_n l$, where f_n is a real number; the total number of events will be calculated as:

$$N = \sum_{l=0}^{l_{max}} n(l) \approx \frac{l_{max}^2 f_n}{2} \tag{4.27}$$

For a given reaction channel, the cross-section is calculated as:

$$\sigma = \sigma_{tot}\frac{n}{N} \tag{4.28}$$

Finally, inserting relations (4.25) and (4.27) into (4.28) yields the average cross section per event (mb/event), which as it turns out does not depend on angular momentum.

$$\frac{\sigma}{n} = \pi\lambda\!\!\!^{-2}\frac{2}{f_n} \tag{4.29}$$

The b (barn) is the unit of cross section, has surface dimensions and is defined as:

$$1\ \text{barn} = 1\text{fm}^2 = 10^{-30}\text{m}^2$$

$$1\ \text{mb} = 10^{-33}\text{m}^2 = 10^{-27}\text{cm}^2$$

From relation (4.29), it can be understood that with proper adjustment of f_n can successfully simulate events with very low cross sections.

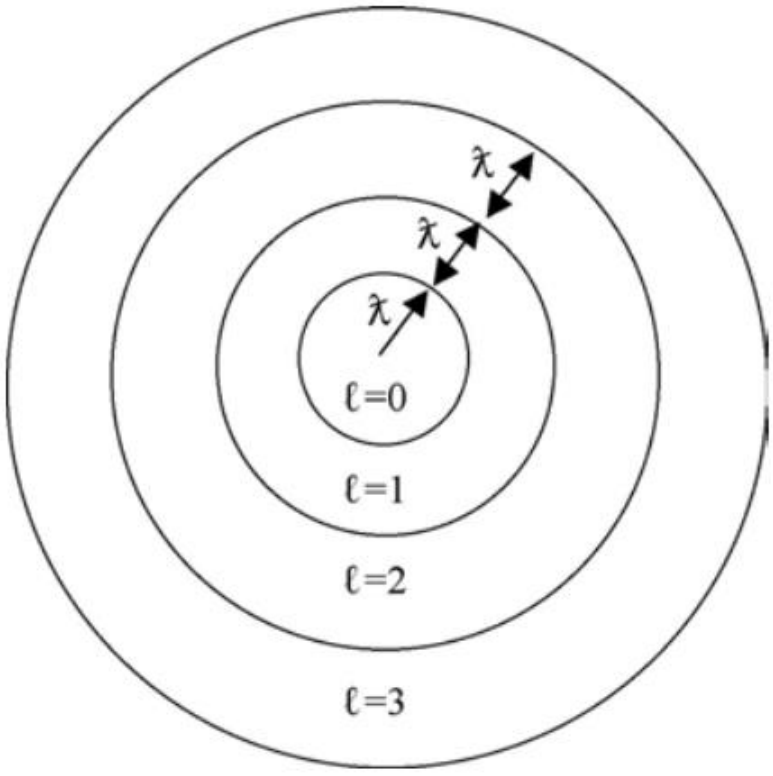

Figure 19: Schematic representation of angular momentum rings of the target nucleus.

4.2: Constrained Molecular Dynamics Model, CoMD

4.2.1: General description of the model

The second model used to describe the dynamic stage of the reactions is the microscopic Constrained Molecular Dynamics (CoMD) model [28,31,33,34]. This model developed by Bonasera and Papa was designed to study the dynamics of reactions at low energies (from Fermi energy, 35 MeV/nucleon, and lower), to describe and study heavy ion collisions [28]. Based on QMD (Quantum Molecular Dynamics) methods [35], it assumes that nucleons are described by Gaussian wave packets that satisfy the uncertainty principle and have σ_r ranges. It is an improved version of molecular dynamics calculations, since, unlike traditional QMD methods, this one considers the fermionic nature of the system through Pauli's exclusion principle, achieved by a restriction in phase space. In the CoMD model, although the antisymmetrization of the wavefunction of the N-particle system is not explicitly applied, this important constraint related to the way the nucleons occupy space in phase space is imposed. In this way, Pauli's principle is effectively restored at each time step of the classical evolution of the system. Short-range and repulsive nucleon-nucleon interactions are described as independent collisions between nucleons which are determined by the active nucleon-nucleon scattering cross section, the available space in phase space and the Pauli principle.

4.2.2: Important quantities

The nucleons in this model behave as Gaussian wave packets. More specifically, for the i_{th} nucleon:

$$\varphi_i(\vec{\mathbf{r}}) = A\exp\left[-\frac{(\vec{r}-\langle\vec{r_i}\rangle)^2}{4\sigma_r^2}+\frac{i}{\hbar}\vec{r}\langle\vec{p_i}\rangle\right] \tag{4.30}$$

where $A=\frac{1}{(2\pi\sigma_r^2)^{3/4}}$ constant, $\langle\vec{r_i}\rangle$, $\langle\vec{p_i}\rangle$ the mean values of the position and momentum of the i_{th} nucleon and are respectively the position-momentum centers of the wave packet and σ_r is the position uncertainty of the wave packet. The total wave function of the N-particle system is expressed as the product of the individual wave functions, as follows:

$$\Phi(\vec{r}) = \prod_i \Phi_i(\vec{r}) \tag{4.31}$$

In the theoretical study of nuclear structure and nuclear reactions it is necessary to have a probability distribution for the positions and momenta of nucleons at the same time. However, it is not possible to determine the position and momentum of a microscopic system at the same time. It is, instead, possible to interchange between the representations in position and momentum space, which is performed by Fourier transformation. For this reason, CoMD uses an alternative formulation of quantum mechanics, that of phase space which is based on the Wigner transformation. This distribution for a particle is expressed as:

$$f_i(\vec{r},\vec{p}) = \frac{1}{\pi^3\hbar^3}\exp\left[-\frac{(\vec{r}-\langle\vec{r_i}\rangle)^2}{2\sigma_r^2} - \frac{2\sigma_r^2(\vec{p}-\langle\vec{p_i}\rangle)^2}{\hbar^2}\right] \quad (4.32)$$

Considering the dispersion of the momentum, the distribution function takes the form:

$$f_i(\vec{r},\vec{p}) = \frac{1}{\pi^3\hbar^3}\exp\left[-\frac{(\vec{r}-\langle\vec{r_i}\rangle)^2}{2\sigma_r^2} - \frac{2\sigma_r^2(\vec{p}-\langle\vec{p_i}\rangle)^2}{2\sigma_p^2}\right] \quad (4.33)$$

The total distribution of N particles will be expressed as the sum of the individual functions f_i:

$$f(\vec{r},\vec{p}) = \sum_i f_i(\vec{r},\vec{p}) \quad (4.34)$$

With the Gaussian description, the time-dependent Schrödinger equation leads to the classical Hamiltonian equations of motion for the centroids of nucleon wave packets:

$$\frac{d}{dt}\langle\vec{p_i}\rangle = -\frac{\partial H}{\partial\langle\vec{r_i}\rangle} \quad (4.35)$$

$$\frac{d}{dt}\langle\vec{r_i}\rangle = -\frac{\partial H}{\partial\langle\vec{p_i}\rangle} \quad (4.36)$$

For a system of A particles with mass m, the total energy H will consist of the sum of the kinetic energies, the effective potential for the nucleon-nucleon interaction and an additional term, which expresses the Gaussian range in momentum space:

$$H = \sum_i \frac{\langle\vec{p_i}\rangle^2}{2m} + A\frac{3\sigma_p}{2m} + V_{eff} \quad (4.37)$$

The constant term $A\frac{3\sigma_p}{2m}$ results from the diffusion of momentum in phase space due to the corresponding uncertainty of momentum. This diffusion is ultimately represented in the kinetic energy of the system. Because it has a constant value, it is not considered in the CoMD calculations [34].

The dynamic part of the Hamiltonian will be discussed in detail in the following section.

4.2.3: Effective Veff potential

In the CoMD model, the potential of the nuclear system is described as a Skyrme-type interaction [36], with the addition of a surface term. Based on the Liquid Drop Model, the operator is divided into the following subterms:

$$V_{eff} = V_{vol} + V_{surf} + V_{coul} + V_{sym} + V^{(3)} \quad (4.38)$$

Each individual subterm is broken down as follows:

$$V_{vol} = \langle V_{vol} \rangle = \frac{T_0}{2\rho_0} \sum_{i=1, j \neq i}^{A} \rho_{ij}$$

$$V_{surf} = \langle V_{surf} \rangle = \frac{C_s}{2\rho_0} \sum_{i=1, j \neq i}^{A} \nabla^2_{\langle r_i \rangle} \rho_{ij}$$

$$V_{coul} = \langle V_{coul} \rangle = \sum_{i=1, j \neq i}^{A} \frac{1}{\left\| \langle \vec{r_i} \rangle - \langle \vec{r_j} \rangle \right\|} \operatorname{erf}\left(\frac{\left\| \langle \vec{r_i} \rangle - \langle \vec{r_j} \rangle \right\|}{2\sigma_r} \right) \tag{4.39}$$

$$V_{sym} = \langle V_{sym} \rangle = \frac{\alpha_{sym}}{2\rho_0} \sum_{i=1, j \neq i}^{A} \left(2\delta_{\tau_i, \tau_j} - 1 \right) \rho_{ij}$$

$$V^{(3)} = \langle V^{(3)} \rangle = \frac{T_3}{\rho_0^{\mu}(\mu + 1)} \sum_{i=1, j \neq i}^{A} \rho_{ij}^{\mu}$$

The first term, V_{vol}, corresponds to the volume term of the liquid drop model. The second term, V_{surf}, expresses the destabilization of surface nucleons relative to internal ones, as they do not have a constitutive force of zero due to having fewer neighboring nucleons exerting attractive forces upon them. The Coulomb term, V_{coul}, represents the electrostatic interactions between protons. The fourth one, V_{sym}, incorporates the asymmetry term between nucleons with the same isospin value. Finally, the term $V^{(3)}$, simulates the simultaneous interactions of three nucleons.

In the above relations, erf(x) is the error function, δ_{ij} is the Kronecker delta, τ_i, τ_j are the isospin projections of the nucleons on the z-axis and T_0, T_3, μ are the parameters of the equation of state of the symmetric nuclear matter.

$$\tau_i = \frac{1}{2}, \text{ for neutrons}$$

$$\tau_i = -\frac{1}{2}, \text{ for protons.}$$

The parameter α_{sym} represents the density dependence of the symmetry energy and ρ_0 is the density of nuclear matter with a value $\rho_0 = 0.165$ fm^{-3}. To express the i_{th} nucleon probability as a function of its position, the density integral takes the following form:

$$\rho_i(\vec{r}) = \int f_i(\vec{r}, \vec{p}) d^3p \tag{4.40}$$

In addition, ρ_{ij} is defined as the superposition integral, or interaction density:

$$\rho_{ij} = \int \rho_i(\vec{r_i}) \rho_j(\vec{r_j}) \delta(\vec{r_i} - \vec{r_j}) d^3r_i \, d^3r_j \tag{4.41}$$

which shows the probability of two nucleons occupying the same nuclear space.

The value of the free parameter C_s in the surface term determines its contribution. The surface term, as well as T_0, T_3 and μ, determine the compressibility of nuclear matter, denoted by K. The compressibility is defined as the change in energy for a change in density and is calculated from the following relation:

$$K = 9\rho_0^2 \frac{\partial^2}{\partial \rho^2}\left(\frac{E}{A}\right) \tag{4.42}$$

According to the authors of the CoMD model, the appropriate value for compressibility is K = 200 MeV.

4.2.4: Method of imposing the Pauli principle

As mentioned earlier, the CoMD model includes a constraint on the position occupied by a nucleon in phase space [37]. Through this constraint, Pauli's exclusion principle is restored, checking the antisymmetry of the wave functions describing the nucleons. As a result, the fermionic nature of the nucleons in the system is stochastically restored. This constraint requires that the occupation probability, $\overline{f_i}$, given by the following relation, is less than unity for each nucleon:

$$\overline{f_i} \leq 1$$

$$\overline{f_i} \equiv \sum_j \delta_{\tau_i,\tau_j}\, \delta_{s_i,s_j} \int_{h^3} f_j(\vec{\mathbf{r}}, \vec{\mathbf{p}}) d^3r d^3p \tag{4.43}$$

where s_i is the z component of the spin and τ_i is the z component of the isospin, of a nucleon i. The integration is performed on a volume h^3 in the phase space around the point $(\langle\overrightarrow{r_i}\rangle, \langle\overrightarrow{p_i}\rangle)$. For each particle i, at each step of the calculation the constraining factor $\overline{f_i}$ is checked. In the case where its value is greater than 1, a set K_i is determined that includes particles at distances $3\sigma_r$ and $3\sigma_p$ in position and momentum space, respectively. The momentum of these particles is changed so that the total momentum is kept constant. Then, the factor $\overline{f_i}$ is checked again and the set K_i is accepted only if the value of $\overline{f_i}$ has been reduced to a value less than 1.

Figure 20 illustrates an example of enforcing the Pauli constraint. The dotted circles represent the elementary cell in phase space. The volume of each cell is considered as a superposition of the cells in momentum space and position space; therefore, it is calculated as follows:

$$V_\varphi = 8L^3\left(\frac{\hbar\pi}{L}\right)^3 = h^3 \tag{4.44}$$

The arrows show the direction of the projection of the spin on the z-axis. At the top of the figure, cell (1) has $\overline{f_i} > 1$, so the constraint needs to be applied. After the necessary nucleon scattering, the configuration depicted at the bottom is obtained, where for each cell h^3 the constraint applies. The second configuration, which is considered acceptable, is equivalent to the first since there was no change in total momentum and kinetic energy.

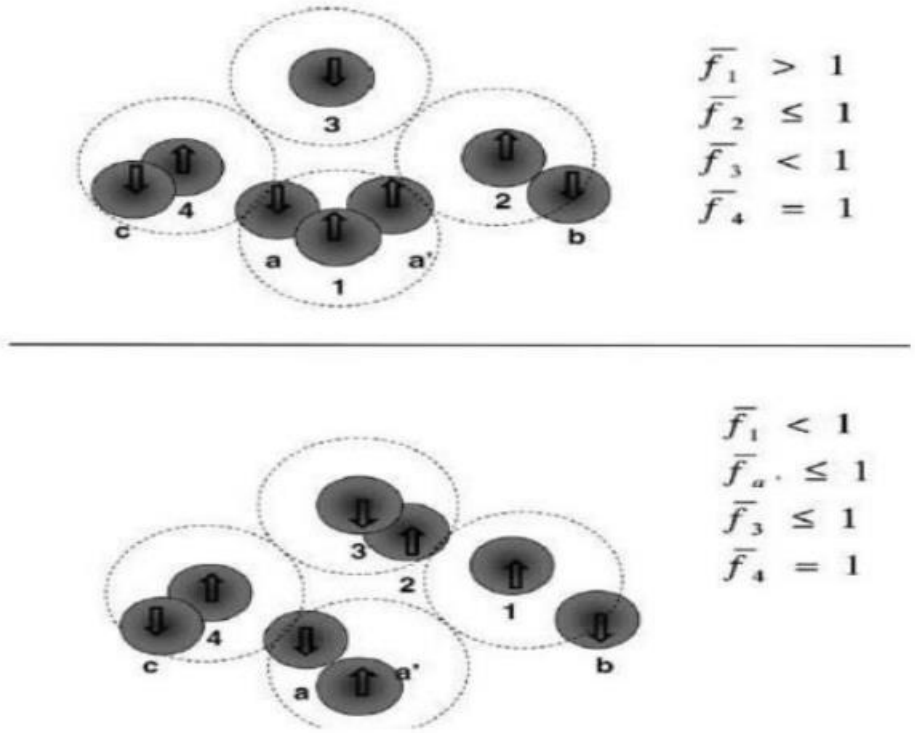

Figure 20: Schematic representation of 8 nucleons in the momentum space before (top) and after (bottom) applying the constraint.

A second method of imposing the fermionic nature of the system involves considering the small-range repulsions between nucleons as individual collisions, which depend on the scattering cross section, the free phase space and the Pauli principle. For each collision, the constraint factor $\overline{f_1}$ is checked and for values less than 1 the collision is considered acceptable. Due to the Gaussian approximation of the system, the constraint $\overline{f_1}$ is expressed by the empirical relation (4.45). In the calculations presented in this study, this constraint is further enhanced by reducing the value of a parameter within the code named: “paulm”.

$$\overline{f_1} = \frac{128}{\text{paulm}} \overline{f_1} \qquad (4.45)$$

The value suggested by the authors of the model for the paulm parameter is 96.

4.3: GEMINI De-excitation Model

Charity's GEMINI model [29,33,38] was used for the decay of the projectile-like fragments. GEMINI is a statistical decay code developed to study sequential binary decay of complex nuclei. The code is based on the Monte Carlo method to observe the decay chain of each nucleus undergoing sequential decays until the final products do not decay further.

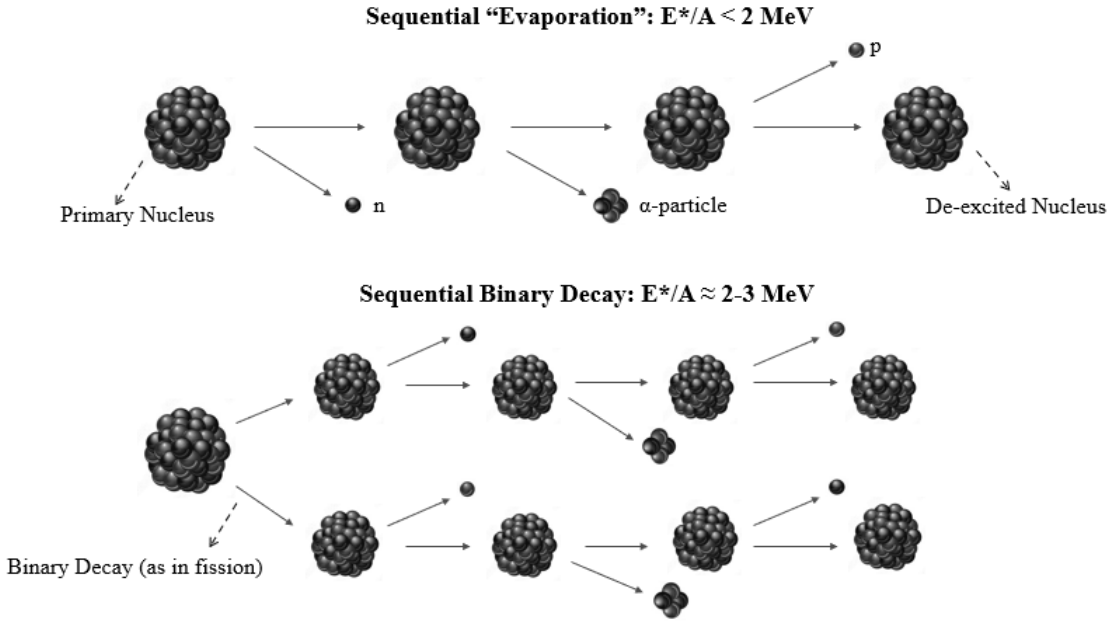

Figure 21: Fragment de-excitation mechanisms considered by the GEMINI code.

The decay and de-excitation of an excited nucleus is based on probabilities. The distribution of de-excitation of a nucleus (Z_0, A_0) into a final product (Z_1, A_1) can be calculated by means of the Breit-Wigner resonance function:

$$P = \frac{2J_R + 1}{(2J_0 + 1)(2J_1 + 1)} \cdot \frac{\Gamma^2}{(E - E_R) + \Gamma^2/_2} \qquad (4.46)$$

where J_R and E_R are the spin and the resonance energy, while Γ represents the decay range, which is related to the average lifetime τ of the decayed state by $\Gamma\tau = \hbar$. Γ is expressed as:

$$\Gamma = \frac{2\pi}{\hbar}|V'_{fi}|^2 \rho(E_f) \qquad (4.47)$$

based on Fermi's golden rule.

For fragments with Z ≤ 2, the energy range of the decay Γ is calculated following the Hauser-Feshbach formalism [39,40]. The process followed to de-excite these nuclei is called evaporation. Considering an excited system (Z_0, A_0) with spin J_0, which decays by emitting a particle (Z_1, A_1) with J_1 and transitions to a final state (Z_2, A_2) with spin J_2, the decay width can be given by the relation:

$$\Gamma_{J2}(Z_1, A_1, Z_2, A_2) = \frac{2J_1 + 1}{2\pi\rho_0} \sum_{I=|J_0-J_2|}^{J_0+J_2} \int_0^{E^*-B-E_{rot}(J_2)} T_l(\varepsilon)\rho_2(U_2, J_2)d\varepsilon \quad (4.48)$$

where l and ε are angular momentum and kinetic energy of the emitted particle, ρ_0 and $\rho_2(U_2, J_2)$ are the energy state densities of the emitted particle and the residual nucleus respectively, and U_2 is the thermal energy of excitation.

$$U_2 = E^* - B - E_{rot}(J_2) - \varepsilon \quad (4.49)$$

B denotes the binding energy and E_{rot} the rotational energy of the final system. The barrier transmission $T_l(\varepsilon)$ is defined as:

$T_l(\varepsilon) = 0$, when

$$\varepsilon \leq E_{coul} + \frac{h^2 l(l+1)}{2\mu R^2} \quad (4.50)$$

$T_l(\varepsilon) = 1$, when

$$\varepsilon > E_{coul} + \frac{h^2 l(l+1)}{2\mu R^2} \quad (4.51)$$

where R is the absorptive radius and μ is the reduced mass of the di-nuclear system.

To describe the decay of heavier fragments, with A ≥ 12, the Moretto formalism is applied, which is based on the saddle point formulation. The range of decay Γ is approximated as follows:

$$\Gamma(Z_1, A_1, Z_2, A_2) = \frac{1}{2\pi\rho_0} \int_0^{E^*-E_{sad}(J_0)} \rho_{sad}(U_{sad}, J_0)d\varepsilon \quad (4.52)$$

where $T_l(\varepsilon) = 1$. ρ_{sad} and U_{sad} denote the density of energy states and the thermal excitation energy of the saddle point, respectively:

$$U_{sad} = E^* - E_{sad}(J_0) - \varepsilon \quad (4.53)$$

$$\rho(U, J) = (2J + 1)\left(\frac{\hbar^2}{2I}\right)^{3/2} \frac{\sqrt{\alpha}}{12U^2} e^{2\sqrt{\alpha U}} \quad (4.54)$$

where α = 8.5 MeV^{-1} is the level density parameter, and I is the moment of inertia of the final system. The above expression of the energy density is derived from Fermi gas theory.

CHAPTER 5
EXPERIMENTAL DATA AND COMPARISONS TO CALCULATIONS

In this section, we present comparisons of the DIT and CoMD calculations with experimental data obtained using the MARS spectrometer. Additionally, we analyze the influence of specific parameters within the CoMD model on the calculations. This study aims to systematically describe the experimental data using the CoMD model, leveraging its many-body approach, which avoids assumptions about the dynamics and thus offers a microscopic description of the process. For simplicity, we will refer to the combined DIT/GEMINI calculations as DIT calculations and the CoMD/GEMINI calculations as CoMD calculations.

The calculations focus on reactions involving a ^{40}Ar beam and a ^{64}Ni target. For these reactions, we present the cross sections of the projectile-like fragments and the momentum distributions for various channels, including neutron pickup, proton removal, neutron removal, charge exchange, and peak isotopes.

It is important to highlight that the experimental data were obtained within the spectrometer's angular window of 4 msr, positioned at a reaction angle of 4°.

Following our group standard calculations different parameters were varied, so as to explore a better depiction of the experimental data with the CoMD model.

As stated before, according to the authors of the CoMD model, the appropriate value for compressibility is K = 200 MeV. Due to literature data [41], the value chosen for our standard calculations is K = 254 MeV. In this dissertation, a comparison of this value with the nuclear compressibility values K = 200 MeV and K = 308 MeV is performed. The higher the value of the compressibility parameter of nuclear matter is, the more incompressible the matter becomes, meaning, it takes a greater amount of energy to compress nuclear matter.

The second parameter we altered was the “ISIG” parameter of the CoMD model. Our group standard for this parameter is the value 0. At this value the nucleon-nucleon differential cross sections, $d\sigma/d\Omega$, in the code follow an isotropic distribution with respect to all angles. By setting the parameter to ISIG=20, an anisotropic distribution of the differential active cross sections $d\sigma/d\Omega$ is determined, where enhanced nucleon-nucleon backward scattering is considered [42].

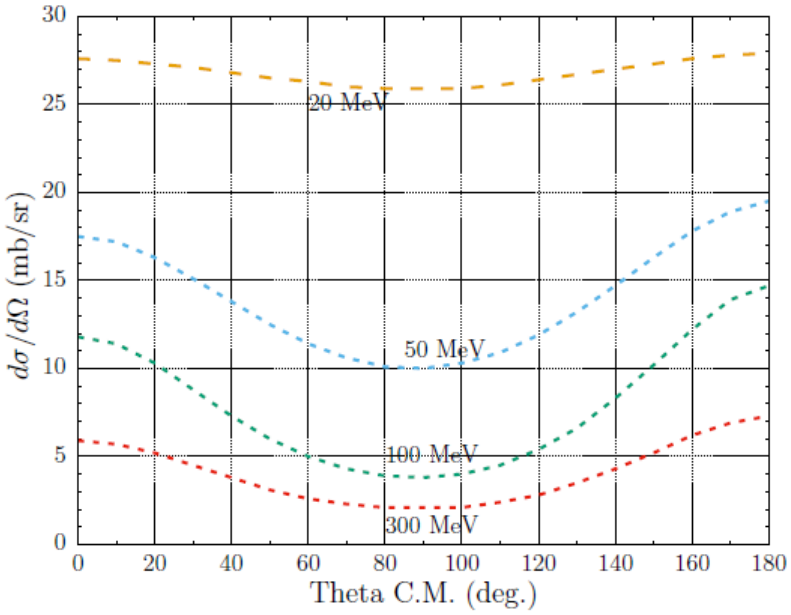

Figure 22: Distributions of proton-neutron differential cross sections versus angle. Each line represents the differential cross section dσ/dΩ, for various values of energy in the laboratory reference frame. The yellow line shows the dσ/dΩ for E_{lab} = 20 MeV, the blue for E_{lab} = 50 MeV, the green for E_{lab} = 100 MeV and the red for E_{lab} = 300 MeV.

In Figure 22, we show the differential cross sections versus angle in the center-of-mass reference frame (cm frame) for different energy values in the laboratory reference frame (laboratory frame). The dσ/dΩ for E_{lab}=20 MeV is shown in yellow line, blue for E_{lab}=50 MeV, green for E_{lab}=100 MeV and red for E_{lab}=300 MeV. The use of the anisotropic distribution seems to enhance the events at angles close to 0° and 180° degrees. The asymmetry at 180° corresponds to charge transfer processes and can cause enhancement of the cross sections in the channels where single charge exchange (SCE) and double charge exchange (DCE) take place.

Pairing is also a parameter that is examined. Our default value is pair = 0 and calculations have been obtained for pair = 4 [43].

Another parameter that was tested was the “paulm” parameter that enforces the Pauli Exclusion Principle. The value suggested by the authors of the model for the paulm parameter is 96. In previous studies of the group, calculations have been carried out with a reduction to the value of 87. In the present study, to examine the stricter enforcement of the Pauli constraint, calculations in which the parameter value has been further reduced to paulm = 80 have been included.

A different approach has also been implemented by separating the CoMD events of specific calculations to breakup and transfer events only. This allows for a comparison of

the CoMD transfer calculations with the DIT calculations which can only consider transfer events, unlike CoMD.

Finally as for the symmetry potential, which varies as a function of density, calculations are presented that were performed with three different versions: The standard CoMD calculations with the standard potential and the parameter isyn = 2 which depends on the density, ρ. Then the stiff potential, isyn = 1, which depends on the 2nd power of density, ρ^2 and the soft potential, isyn = 3, which depends on the square root of density, $\sqrt{\rho}$.

5.1 Mass Distributions

In this section, we present the observed mass distributions of selected projectile fragments with atomic numbers Z = 13 – 20, produced in the reaction of ^{40}Ar (15 MeV/nucleon) with ^{64}Ni. These experimental results are compared with theoretical calculations performed using the DIT and CoMD models. The diagrams display the mass number (A) on the x-axis and the total cross-section (σ, in millibarns) on the y-axis. The measured distributions within the solid angle window of $\Delta\Omega$ = 4 msr were integrated over the azimuthal angle, effectively scaling the data by a factor of 7. This allowed us to calculate the production cross-sections for each isotope in the polar angular range $\Delta\theta$ = 2.2° – 5.8°.

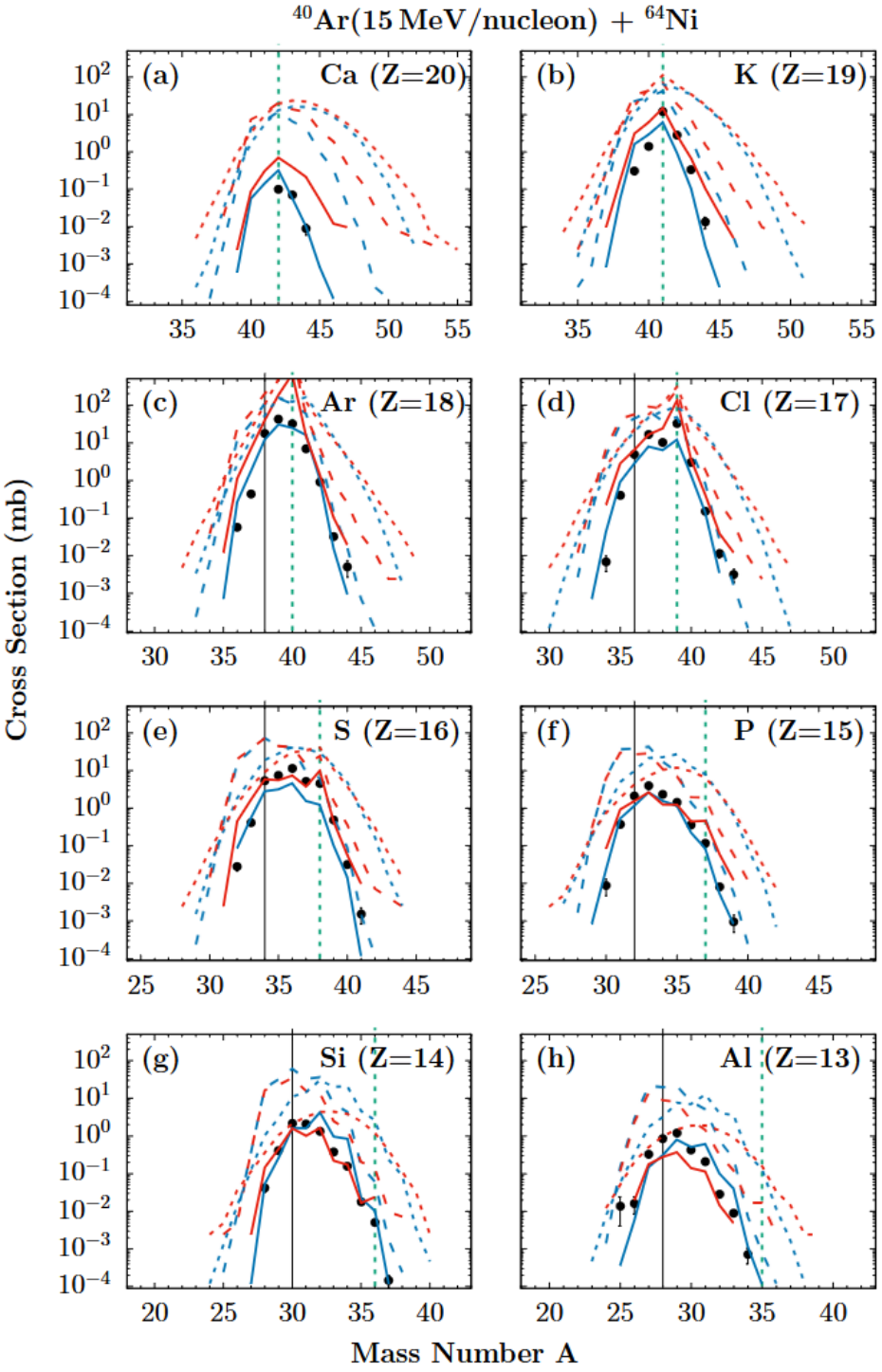

Figure 23: Production cross sections (mass distributions) of elements with Z = 13 - 20 from the reaction ^{40}Ar (15 MeV/nucleon) + ^{64}Ni. Black points: experimental data. DIT calculations: Dotted (blue) lines: primary fragments, Dashed (blue) lines: final (cold) fragments, Full (blue) lines: final fragments filtered for angular acceptance and magnetic rigidity. CoMD calculations: Dotted (red) lines: primary fragments, Dashed (red) lines: final (cold) fragments, Full (red) lines: final fragments filtered for angular acceptance and magnetic rigidity. The vertical dashed (green) lines indicate the initiation of neutron pickup. On the left of the vertical black lines the data are obtained with incomplete magnetic rigidity coverage.

Figure 23 illustrates the mass distributions for the final, de-excited fragments resulting from the reaction, based on experimental data [19] (depicted as black points), for atomic numbers Z = 13 – 20. The vertical green dashed line marks the onset of neutron pickup. The mass distributions are compared with calculations based on the DIT and the CoMD model.

The beam energy in the DIT model is adjusted to 14.68 MeV/nucleon to account for the energy loss as the beam passes through the target. The DIT calculations were performed with a large dataset (15 million events) to minimize statistical uncertainties. As noted in the literature [27], the DIT model does not account for particle emission prior to the thermal equilibration of the primary hot fragment (pre-equilibrium emission). Consequently, the primary fragments are highly excited. To address this, an empirical correction was applied to the DIT calculations by reducing the excitation energy of the primary fragments to $E^*_{corrected} = 0.75E^*$.

The DIT calculations are represented by solid blue lines for the final, de-excited fragments filtered for angular acceptance and magnetic rigidity, by dashed blue lines for total cold fragments and by dotted blue lines for the primary, hot fragments that have not undergone de-excitation.

The results demonstrate that the DIT model provides a satisfactory representation of the experimental mass distributions across all studied channels. The final, de-excited fragment distributions closely match the experimental data. Additionally, the primary fragment distributions exhibit higher cross-section values than the final fragments. This difference is attributed to the de-excitation process, during which primary fragments lose nucleons and/or other particles to form the final fragments.

For CoMD calculations, optimized configurations and ground-state parameters from [33] were employed, referred to as "standard" calculations. These simulations were based on 3×10^6 events with a beam energy of 14.68 MeV/nucleon, a Pauli constraint enhancement parameter of paulm = 87, nuclear matter compressibility K = 254 MeV, and an impact parameter range of b = 0 – 14 fm. The reaction system was evolved over t = 600 fm/c (2 zs), sufficient to capture the dynamic phase without significant fragment de-excitation.

The CoMD calculations are represented by solid red lines for the final, de-excited fragments filtered for angular acceptance and magnetic rigidity, by dashed red lines for total cold fragments and by dotted red lines for the primary, hot fragments that have not undergone de-excitation.

The CoMD model successfully describes the experimental mass distributions. Primary fragments exhibit higher cross-sections compared to de-excited fragments due to nucleon or particle emission during de-excitation. The dataset for standard CoMD is approximately 2 million events.

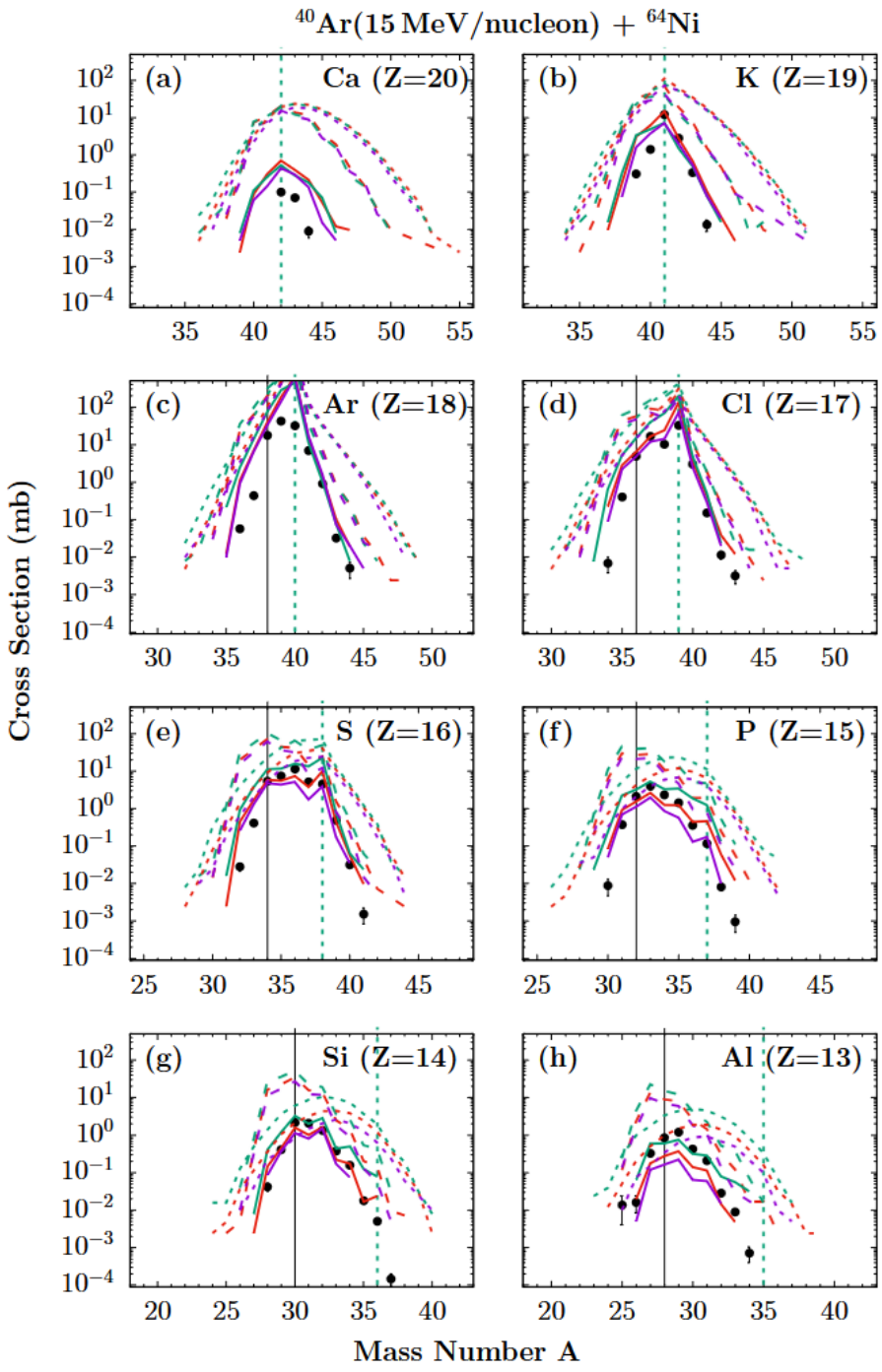

Figure 24: Production cross sections (mass distributions) of elements with Z = 13 - 20 from the reaction ^{40}Ar (15 MeV/nucleon) + ^{64}Ni. Black points: experimental data. CoMD calculations: Dotted (red) lines: primary fragments, Dashed (red) lines: final (cold) fragments, Full (red) lines: final fragments filtered for angular acceptance and magnetic rigidity. CoMD calculations K = 200: Dotted (green) lines: primary fragments, Dashed (green) lines: final (cold) fragments, Full (green) lines: final fragments filtered for angular acceptance and magnetic rigidity. CoMD calculations K = 308: Dotted (purple) lines: primary fragments, Dashed (purple) lines: final (cold) fragments, Full (purple) lines: final fragments filtered for angular acceptance and magnetic rigidity. The vertical dashed (green) lines indicate the initiation of neutron pickup. On the left of the vertical black lines the data are obtained with incomplete magnetic rigidity coverage.

In Figure 24, the effect of nuclear compressibility (K) is explored. Standard calculations with K = 254 MeV (red lines) are compared with calculations for K = 200 MeV (soft compressibility, green lines) and K = 308 MeV (hard compressibility, purple lines). While all compressibility values yield similar results, soft compressibility (K = 200 MeV) slightly overestimates the neutron-rich side, whereas hard compressibility (K = 308 MeV) better matches this region but underestimates other parts. The dataset for CoMD with K = 200 MeV is approximately 0.65 million events and for K = 308 MeV 1 million events.

In Figure 25 we examine the parameters pair = 4 and ISIG = 20. Nucleon-nucleon collisions are taken into account by the ISIG parameter. Standard calculations with pair = 0 and ISIG = 0 represented with red lines are compared with calculations for pair = 4 represented with green lines and ISIG = 20 represented with purple lines. All calculations seem to be more or less in agreement with the experimental data. The dataset for CoMD with ISIG = 20 is approximately 3 million events and for the pair = 4 1.8 million events.

In Figure 26 we test the parameters isyn = 1 and isyn = 3 that represent the symmetry potential from Bethe-Weiszaeker equation. Stiff density dependence is described by the parameter isyn = 1 and soft density dependence by the parameter isyn = 3. Calculations with stiff density dependence are represented by green lines and purple lines represent the calculations for soft density dependence. All calculations seem to be more or less in agreement with the experimental data and especially the isyn = 1 which improves the description of the data. The dataset for isyn = 1 is 3.6 million events and for isyn = 3 is 3.3 million events.

In Figure 27 standard CoMD calculations have been divided into breakup and transfer events. Purple lines represent the breakup mechanism and green lines the transfer mechanism. These calculations are compared with the DIT calculations and we observe that the transfer mechanism lays closer to the DIT, as the DIT model does not account for breakup mechanism.

In Figure 28 standard CoMD calculations are compared with CoMD calculations with enhanced Pauli constraint represented by green lines in accordance with the red lines for “standard” CoMD. The standard value of paulm = 87 was reduced to paulm = 80, enhancing the enforcement of the Pauli principle at each time step. The enhanced CoMD calculations slightly improve the mass distribution description, but occasionally overestimates experimental data, particularly on the neutron-rich side. The dataset for CoMD, paulm = 80 is 0.75 million events.

In Figure 29 CoMD calculations with enhanced Pauli constraint (paulm = 80) have been once again divided into breakup and transfer events. Again we observe that the transfer calculations are closer to the DIT calculations for the aforementioned reasons.

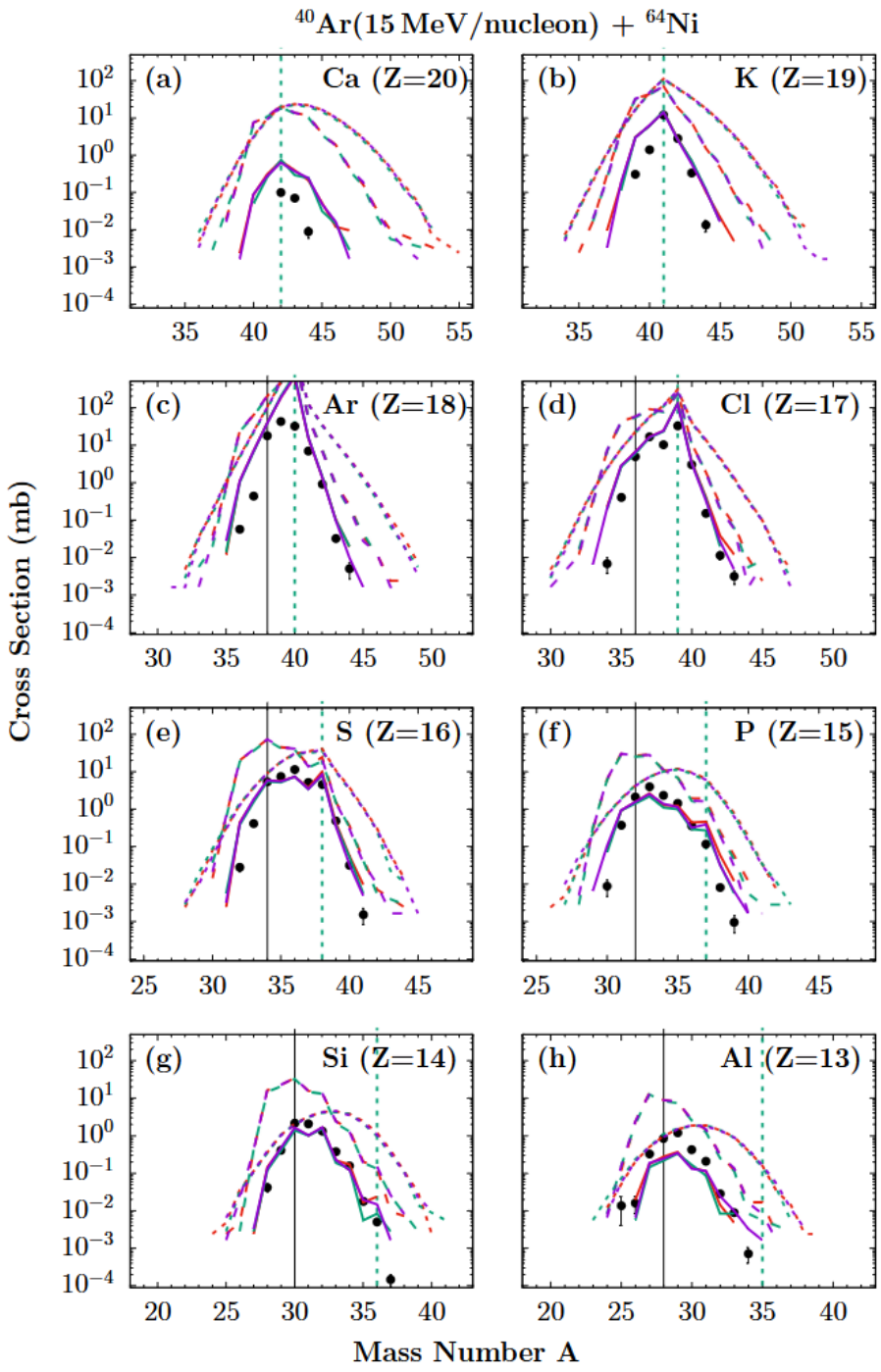

Figure 25: Production cross sections (mass distributions) of elements with Z = 13 - 20 from the reaction ^{40}Ar (15 MeV/nucleon) + ^{64}Ni. Black points: experimental data. CoMD calculations: Dotted (red) lines: primary fragments, Dashed (red) lines: final (cold) fragments, Full (red) lines: final fragments filtered for angular acceptance and magnetic rigidity. CoMD calculations pair = 4: Dotted (green) lines: primary fragments, Dashed (green) lines: final (cold) fragments, Full (green) lines: final fragments filtered for angular acceptance and magnetic rigidity. CoMD calculations ISIG = 20: Dotted (purple) lines: primary fragments, Dashed (purple) lines: final (cold) fragments, Full (purple) lines: final fragments filtered for angular acceptance and magnetic rigidity. The vertical dashed (green) lines indicate the initiation of neutron pickup. On the left of the vertical black lines the data are obtained with incomplete magnetic rigidity coverage.

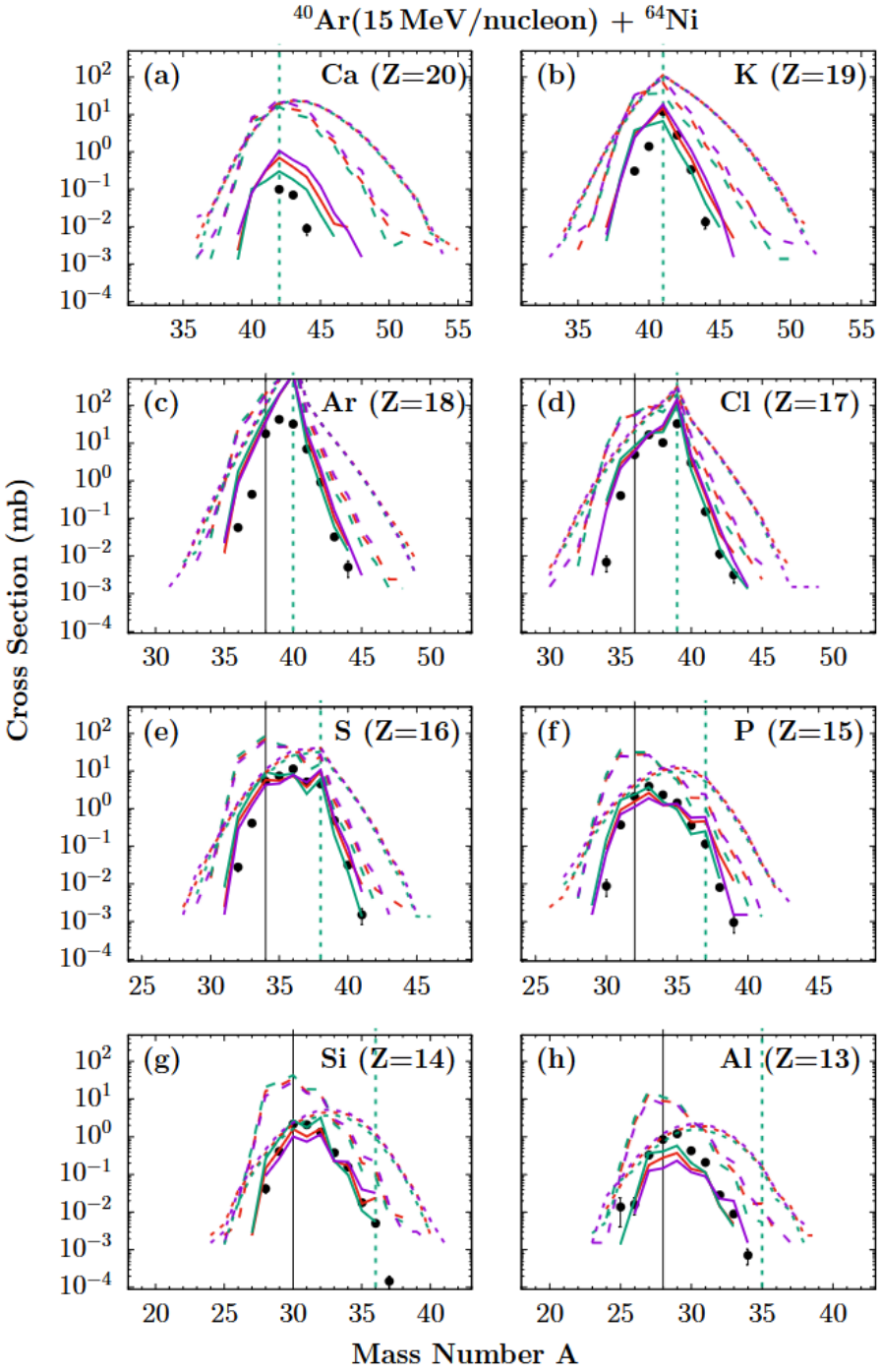

Figure 26: Production cross sections (mass distributions) of elements with Z = 13 - 20 from the reaction ^{40}Ar (15 MeV/nucleon) + ^{64}Ni. Black points: experimental data. CoMD calculations: Dotted (red) lines: primary fragments, Dashed (red) lines: final (cold) fragments, Full (red) lines: final fragments filtered for angular acceptance and magnetic rigidity. CoMD calculations isyn = 1: Dotted (green) lines: primary fragments, Dashed (green) lines: final (cold) fragments, Full (green) lines: final fragments filtered for angular acceptance and magnetic rigidity. CoMD calculations isyn = 3: Dotted (purple) lines: primary fragments, Dashed (purple) lines: final (cold) fragments, Full (purple) lines: final fragments filtered for angular acceptance and magnetic rigidity. The vertical dashed (green) lines indicate the initiation of neutron pickup. On the left of the vertical black lines the data are obtained with incomplete magnetic rigidity coverage.

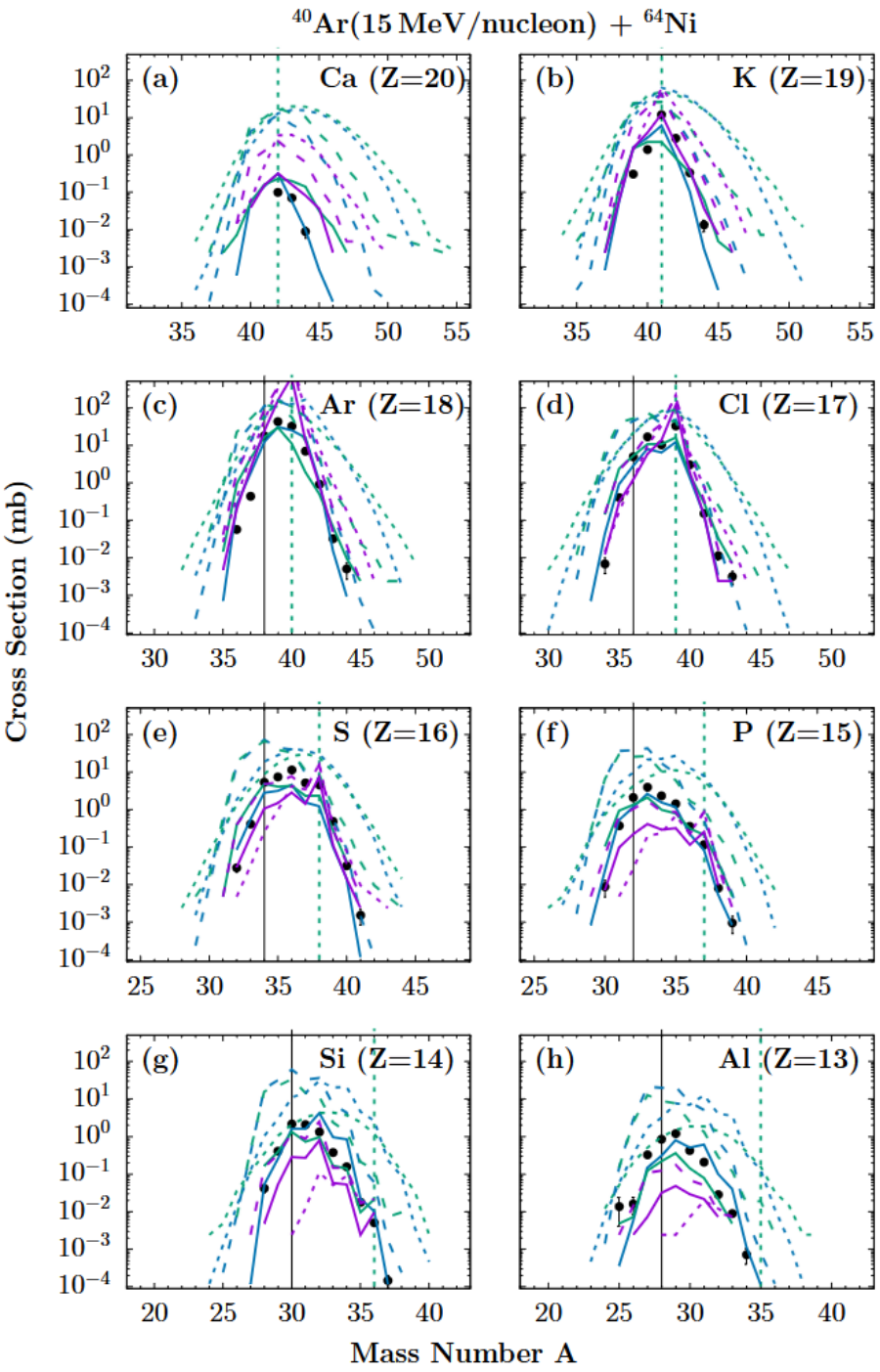

Figure 27: Production cross sections (mass distributions) of elements with Z = 13 - 20 from the reaction ^{40}Ar (15 MeV/nucleon) + ^{64}Ni. Black points: experimental data. DIT calculations: Dotted (blue) lines: primary fragments, Dashed (blue) lines: final (cold) fragments, Full (blue) lines: final fragments filtered for angular acceptance and magnetic rigidity. CoMD calculations transfer: Dotted (green) lines: primary fragments, Dashed (green) lines: final (cold) fragments, Full (green) lines: final fragments filtered for angular acceptance and magnetic rigidity. CoMD calculations breakup: Dotted (purple) lines: primary fragments, Dashed (purple) lines: final (cold) fragments, Full (purple) lines: final fragments filtered for angular acceptance and magnetic rigidity. The vertical dashed (green) lines indicate the initiation of neutron pickup. On the left of the vertical black lines the data are obtained with incomplete magnetic rigidity coverage.

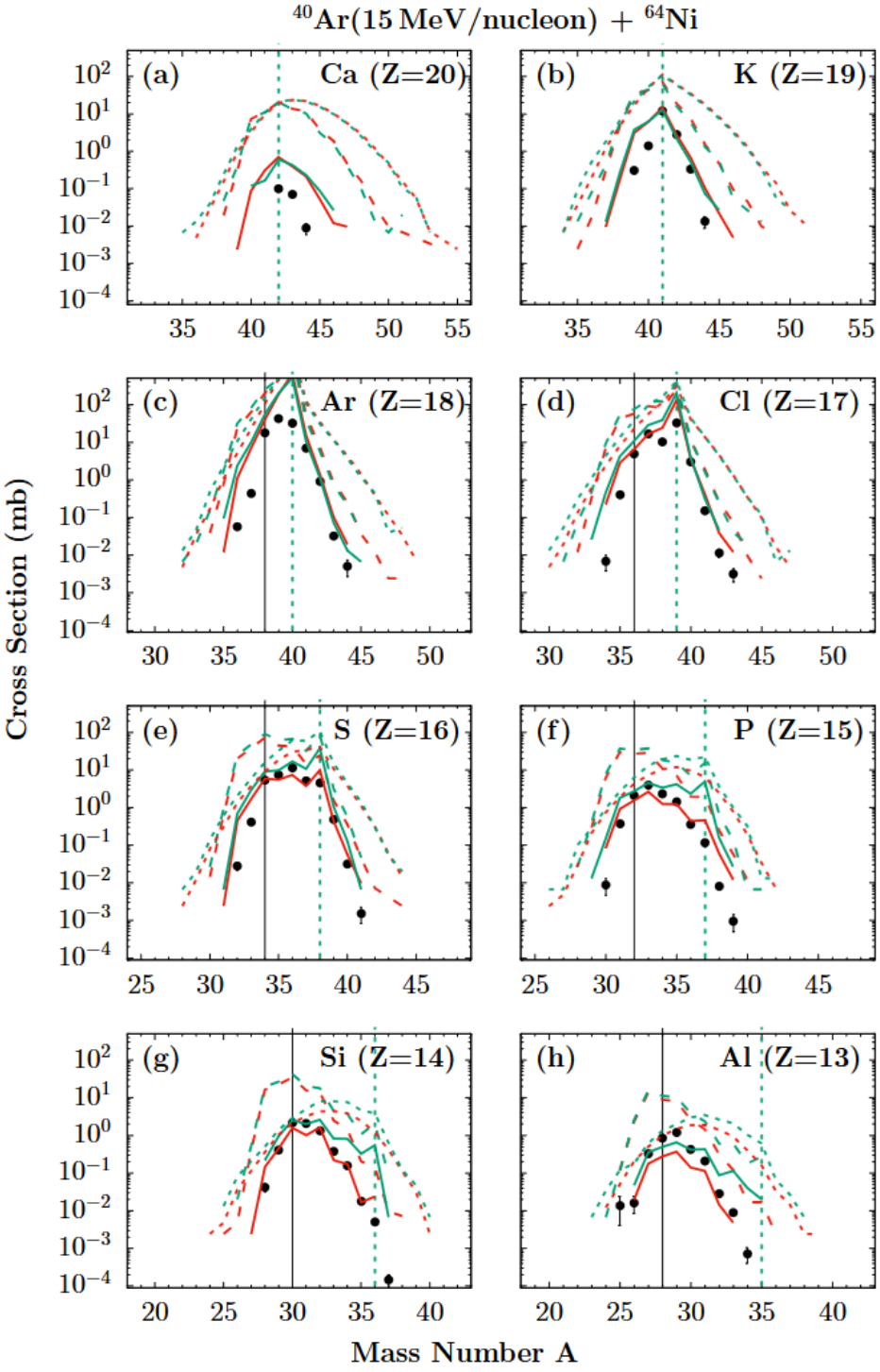

Figure 28: Production cross sections (mass distributions) of elements with Z = 13 - 20 from the reaction ^{40}Ar (15 MeV/nucleon) + ^{64}Ni. Black points: experimental data. CoMD calculations: Dotted (red) lines: primary fragments, Dashed (red) lines: final (cold) fragments, Full (red) lines: final fragments filtered for angular acceptance and magnetic rigidity. CoMD calculations paulm = 80: Dotted (green) lines: primary fragments, Dashed (green) lines: final (cold) fragments, Full (green) lines: final fragments filtered for angular acceptance and magnetic rigidity. The vertical dashed (green) lines indicate the initiation of neutron pickup. On the left of the vertical black lines the data are obtained with incomplete magnetic rigidity coverage.

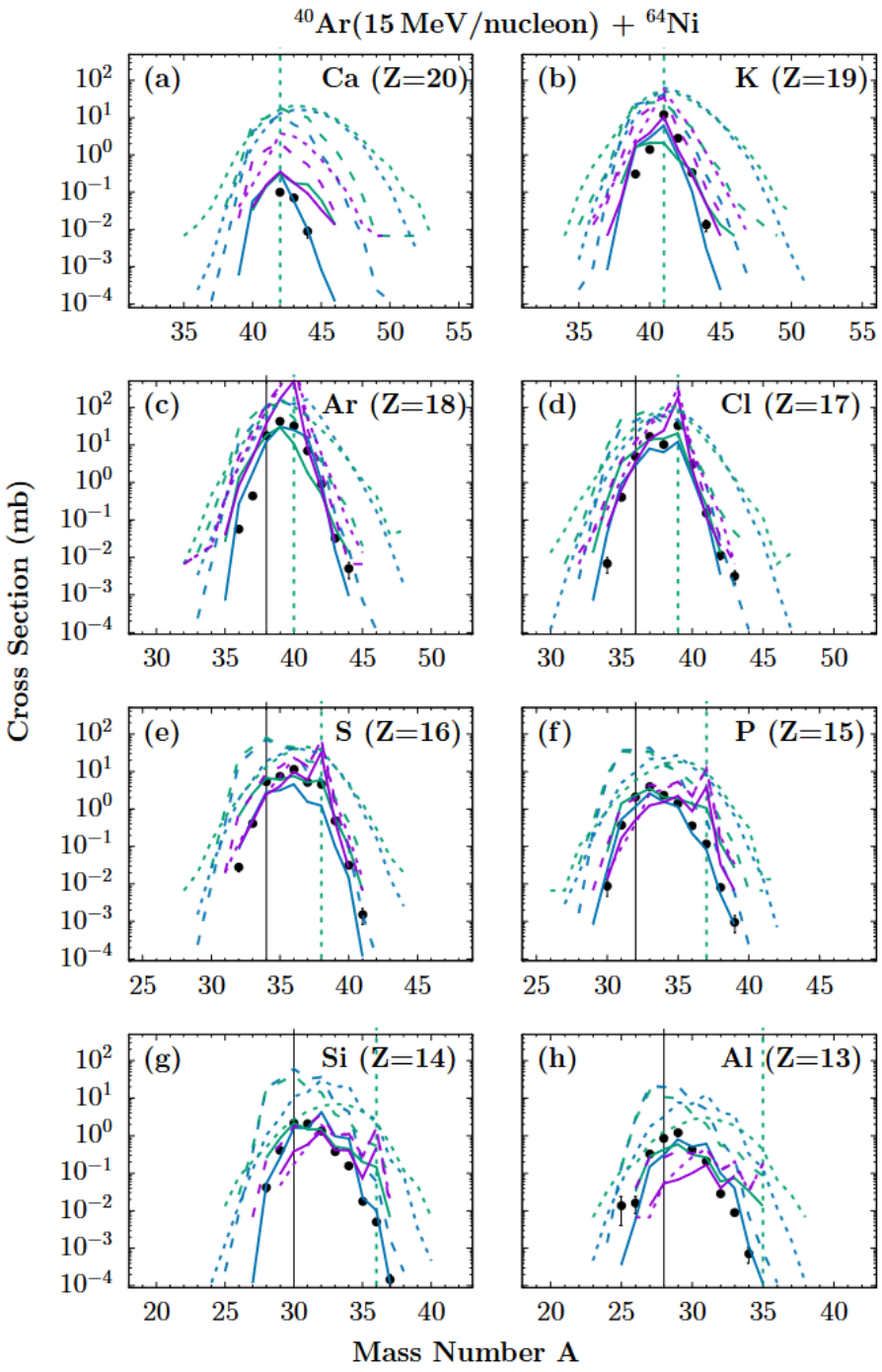

Figure 29: Production cross sections (mass distributions) of elements with Z = 13 - 20 from the reaction ^{40}Ar (15 MeV/nucleon) + ^{64}Ni. Black points: experimental data. DIT calculations: Dotted (blue) lines: primary fragments, Dashed (blue) lines: final (cold) fragments, Full (blue) lines: final fragments filtered for angular acceptance and magnetic rigidity. CoMD calculations paulm = 80, transfer: Dotted (green) lines: primary fragments, Dashed (green) lines: final (cold) fragments, Full (green) lines: final fragments filtered for angular acceptance and magnetic rigidity. CoMD calculations paulm = 80, breakup: Dotted (purple) lines: primary fragments, Dashed (purple) lines: final (cold) fragments, Full (purple) lines: final fragments filtered for angular acceptance and magnetic rigidity. The vertical dashed (green) lines indicate the initiation of neutron pickup. On the left of the vertical black lines the data are obtained with incomplete magnetic rigidity coverage.

5.2 Momentum Distributions

In our subsequent analysis, we present the measured differential cross-sections versus the linear momentum per nucleon (p/A) of the fragments. The momentum per nucleon serves as an indicator of the velocity of the ejectiles, facilitating direct comparisons with the beam velocity. Similar to kinetic energy, p/A provides valuable insight into energy dissipation and the underlying reaction mechanisms. In the plots, the x-axis represents the momentum per nucleon (p/A), while the y-axis represents the differential cross-section with respect to solid angle and p/A, $(d^2\sigma)/(d\Omega\, d(p/A))$, expressed in units of mb/(msr(MeV/c)). These are measured cross-sections, and the data, along with calculations, are presented for the angular range $\Delta\theta$ = 2.2° – 5.8° (measured at approximately 4°). We refer to these distributions as "momentum distributions" throughout the discussion.

Each plot illustrates the momentum distribution for a specific projectile-like fragment. Experimental data are displayed as black points, while theoretical calculations are shown in various colors and shapes. Notably, the experimental data exhibit pronounced "dips," which are artifacts introduced by software gates applied during data analysis to exclude elastically scattered beam components. The parameter Q_{gg}, displayed at the top of each plot, represents the ground-state-to-ground-state Q-value, which is calculated using the masses of the products in their ground states, as previously discussed. Additionally, the total excitation energy (in MeV), determined from binary kinematics, using the corresponding p/A values, is indicated above or below certain peaks.

In the figures presented, a vertical green dashed line marks the projectile velocity at 166 MeV/c. The momentum distributions can be qualitatively divided into two regions. On the right side of most distributions, there is a noticeable peak or "band" near the beam velocity, corresponding to the quasi-elastic region. On the left side, an extended region indicates higher excitation energies of the di-nuclear system, representing more dissipative events.

The channels of the reaction that are of interest for the current work are the neutron pickup channels, from +1 to +4 neutrons, the proton removal channels, from -1 to -4 protons, the neutron removal channels from -1 to -4 neutrons, the single and double charge exchange channels and the peak isotope channels for Z= 20 to Z = 13.

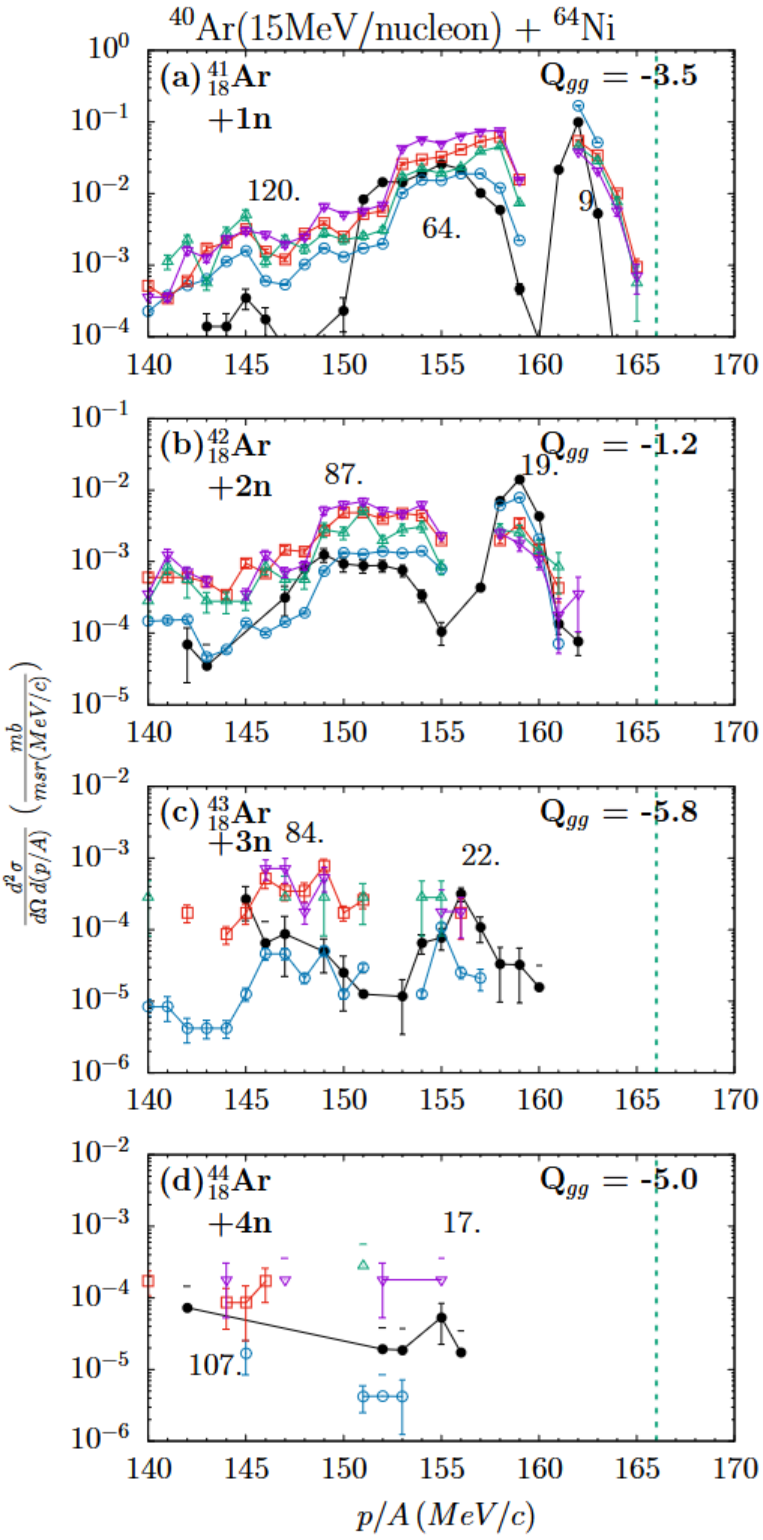

Figure 30: Momentum per nucleon distributions of projectile-like fragments for neutron pick-up channels. Black points: experimental data. Blue circles: DIT calculation. Red squares: CoMD calculation, with K = 254 MeV. The vertical dashed (green) lines indicate the velocity of the beam. Green triangles: CoMD calculations, with K = 200 MeV. Purple inverse triangles: CoMD calculation, with K = 308 MeV.

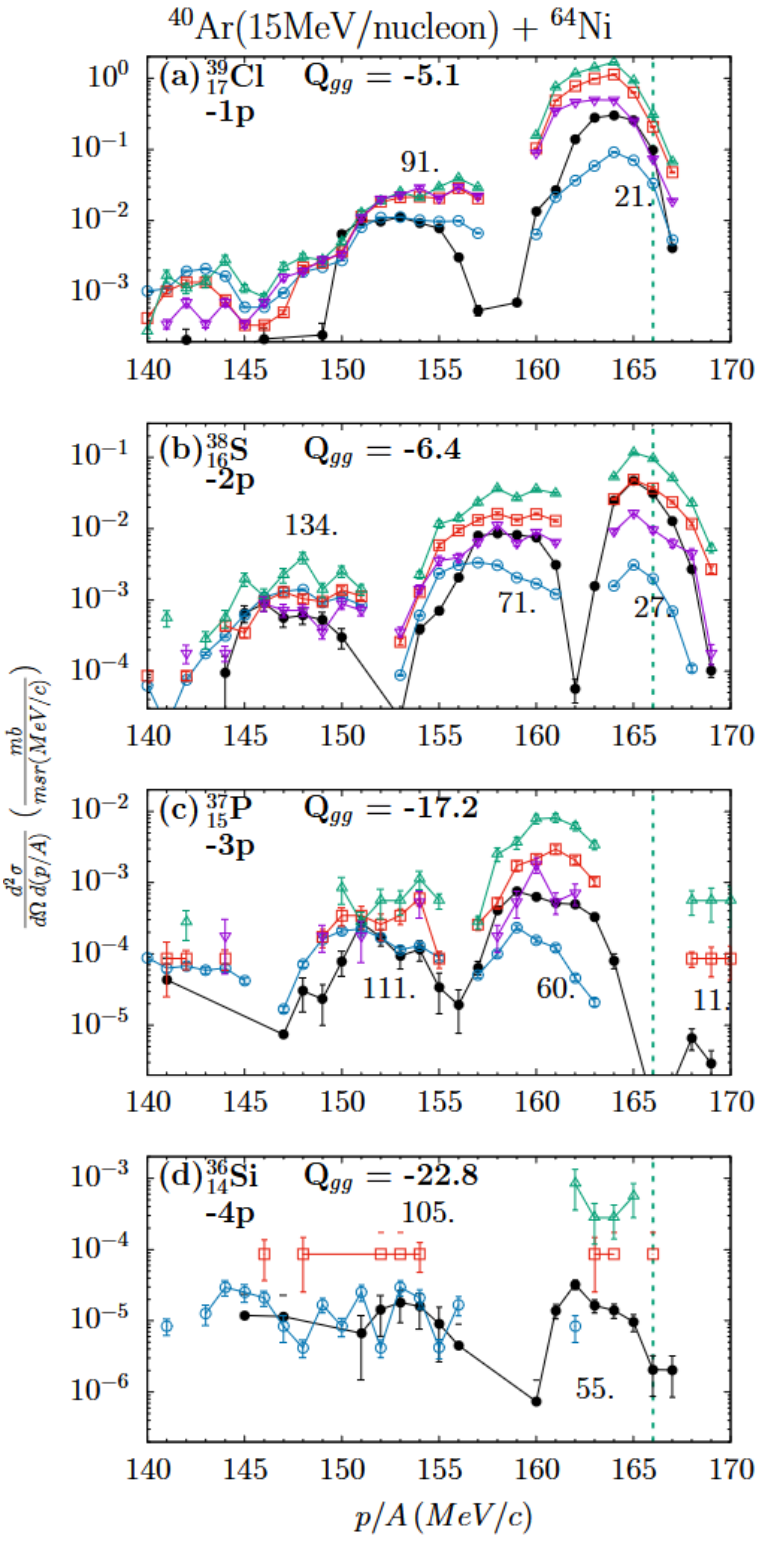

Figure 31: Momentum per nucleon distributions of projectile-like fragments for proton removal channels. Black points: experimental data. Blue circles: DIT calculation. Red squares: CoMD calculation, with K = 254 MeV. The vertical dashed (green) lines indicate the velocity of the beam. Green triangles: CoMD calculations, with K = 200 MeV. Purple inverse triangles: CoMD calculation, with K = 308 MeV.

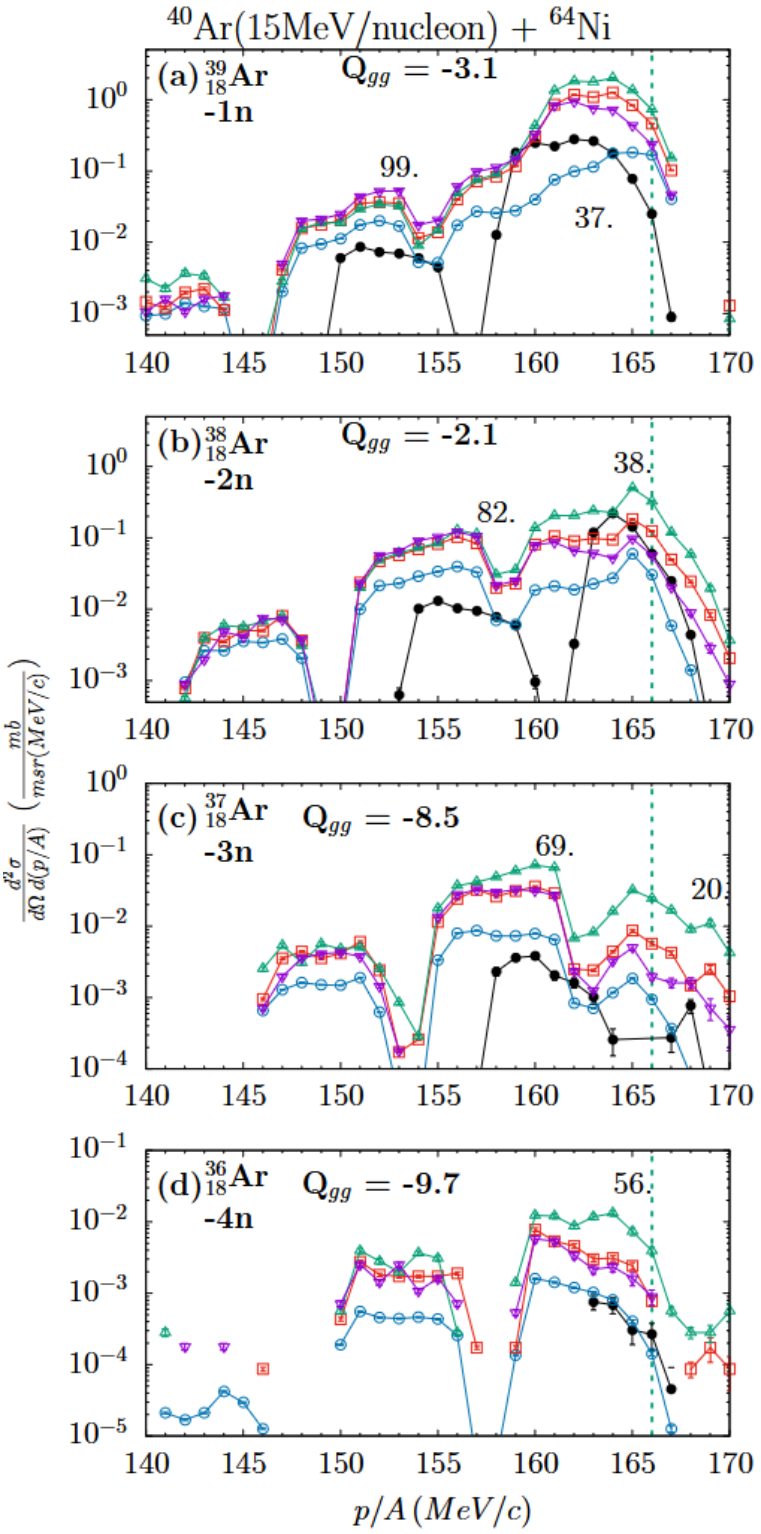

Figure 32: Momentum per nucleon distributions of projectile-like fragments for neutron removal channels. Black points: experimental data. Blue circles: DIT calculation. Red squares: CoMD calculation, with K = 254 MeV. The vertical dashed (green) lines indicate the velocity of the beam. Green triangles: CoMD calculations, with K = 200 MeV. Purple inverse triangles: CoMD calculation, with K = 308 MeV.

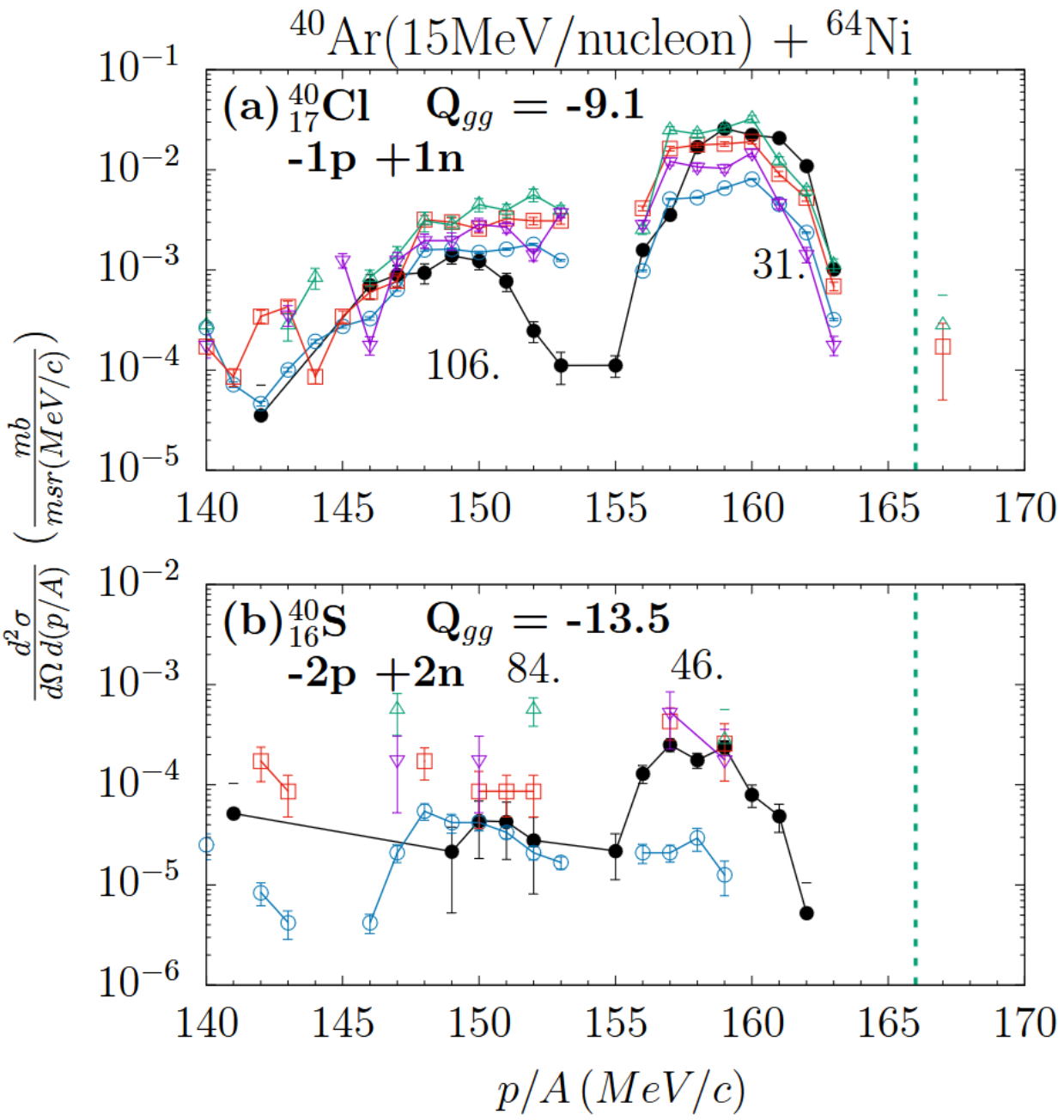

Figure 33: Momentum per nucleon distributions of projectile-like fragments for charge exchange channels. Black points: experimental data. Blue circles: DIT calculation. Red squares: CoMD calculation, with K = 254 MeV. The vertical dashed (green) lines indicate the velocity of the beam. Green triangles: CoMD calculations, with K = 200 MeV. Purple inverse triangles: CoMD calculation, with K = 308 MeV.

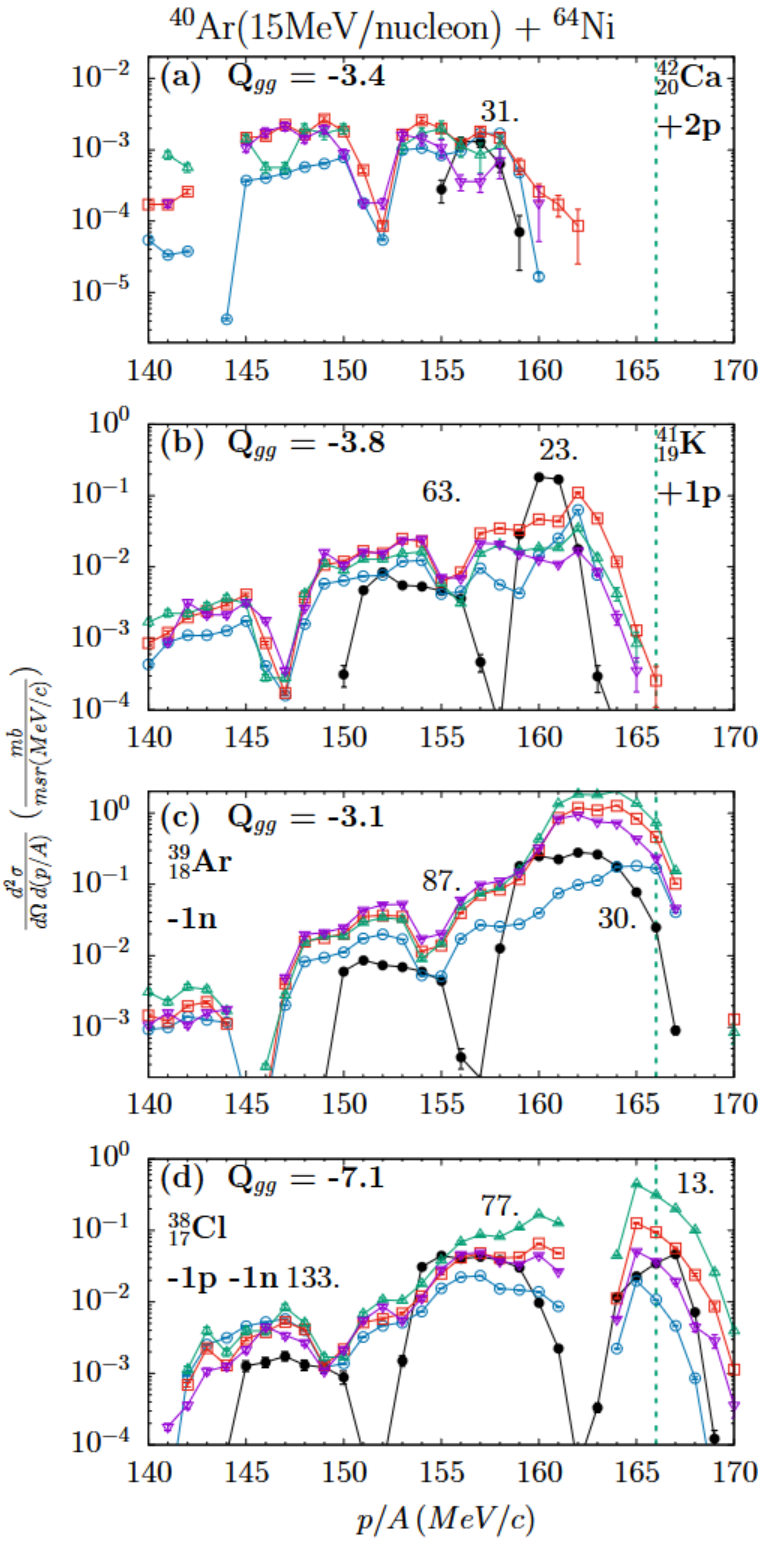

Figure 34: Momentum per nucleon distributions of projectile-like fragments for peak isotope channels (20 – 17). Black points: experimental data. Blue circles: DIT calculation. Red squares: CoMD calculation, with K = 254 MeV. The vertical dashed (green) lines indicate the velocity of the beam. Green triangles: CoMD calculations, with K = 200 MeV. Purple inverse triangles: CoMD calculation, with K = 308 MeV.

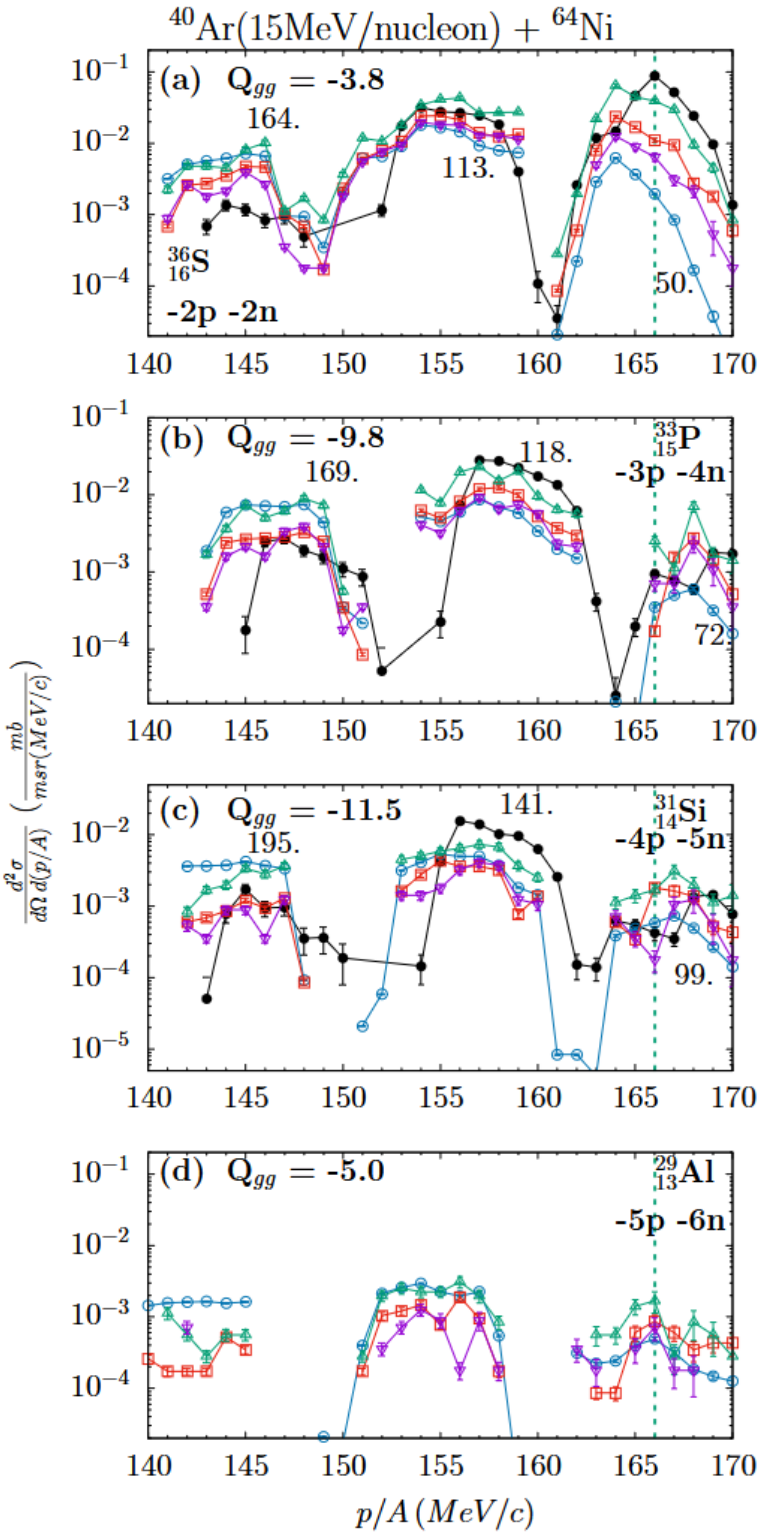

Figure 35: Momentum per nucleon distributions of projectile-like fragments for peak isotope channels (16 – 13). Black points: experimental data. Blue circles: DIT calculation. Red squares: CoMD calculation, with K = 254 MeV. The vertical dashed (green) lines indicate the velocity of the beam. Green triangles: CoMD calculations, with K = 200 MeV. Purple inverse triangles: CoMD calculation, with K = 308 MeV.

In Figures 30 – 35 we can observe for all the channels of interest the experimental data, the DIT and standard CoMD calculations and their comparison with CoMD calculations with softer (K = 200) and harder (K =308) nuclear matter compressibility. The experimental data are represented by black dots, the DIT calculation by blue circles, the CoMD calculation by red squares, the softer compressibility by green triangles and the harder compressibility by purple inverted triangles.

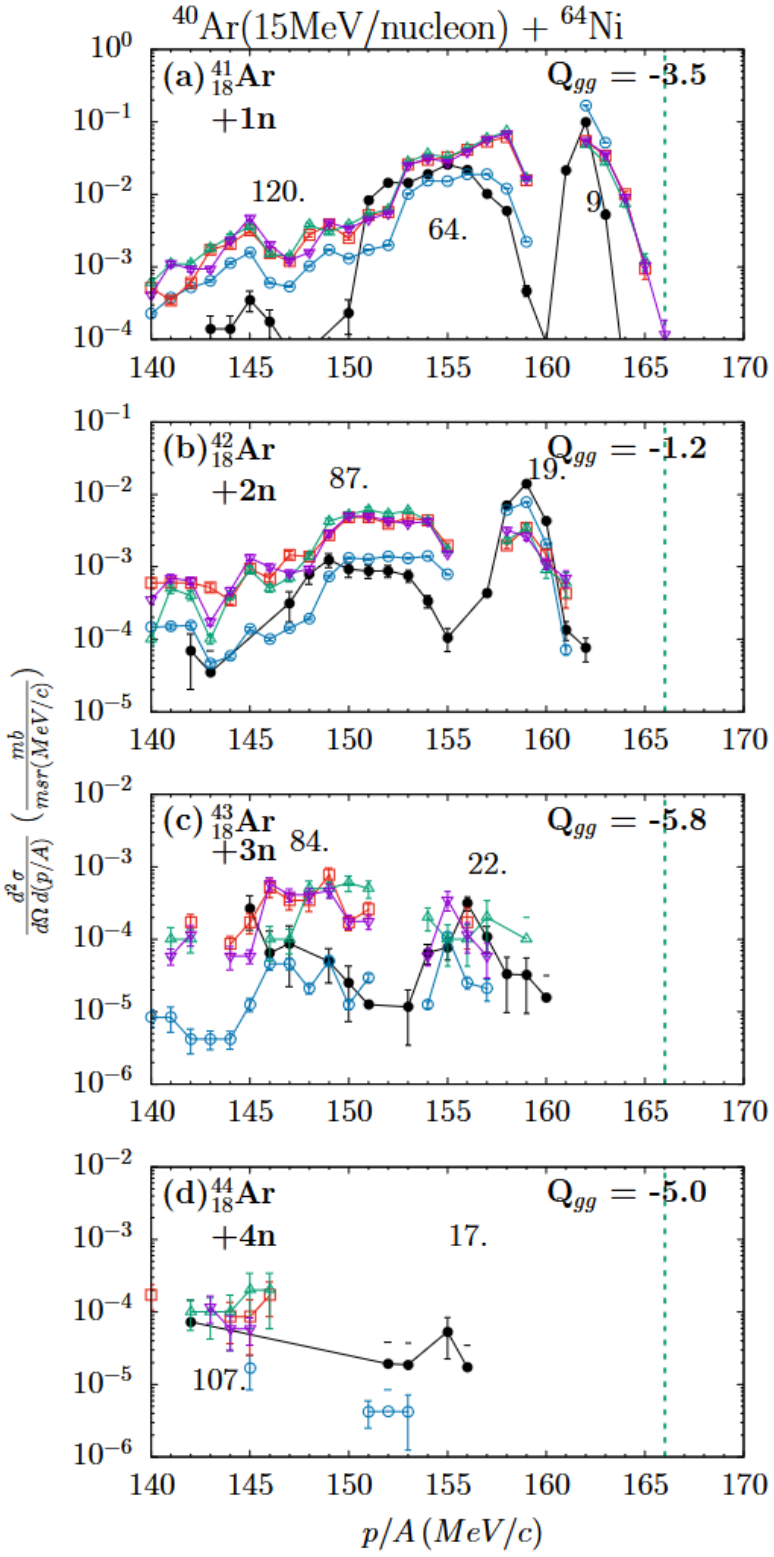

Figure 36: Momentum per nucleon distributions of projectile-like fragments for neutron pick-up channels. Black points: experimental data. Blue circles: DIT calculation. Red squares: CoMD calculation. The vertical dashed (green) lines indicate the velocity of the beam. Green triangles: CoMD calculations, with pair = 4. Purple inverse triangles: CoMD calculation, isig = 20.

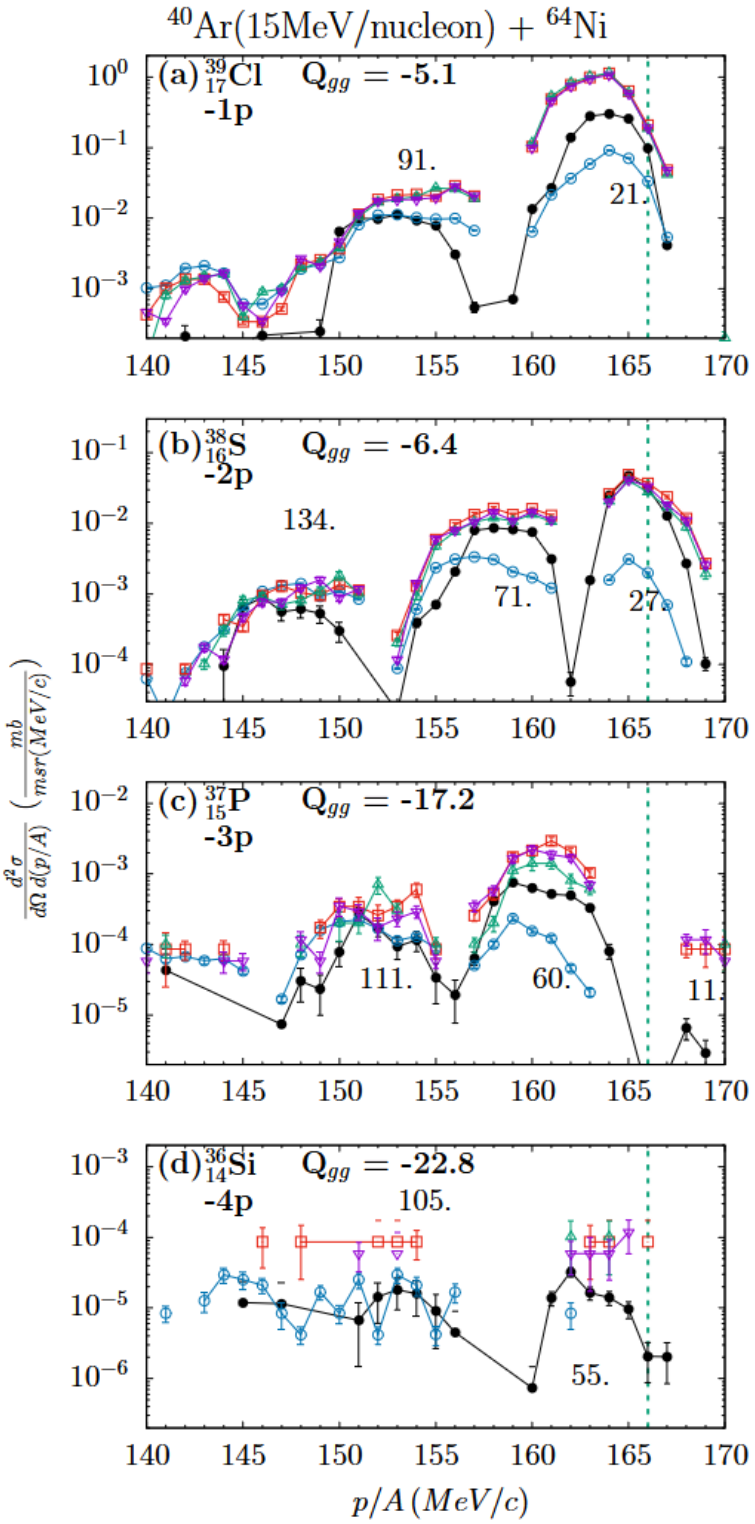

Figure 37: Momentum per nucleon distributions of projectile-like fragments for proton removal channels. Black points: experimental data. Blue circles: DIT calculation. Red squares: CoMD calculation. The vertical dashed (green) lines indicate the velocity of the beam. Green triangles: CoMD calculations, with pair = 4. Purple inverse triangles: CoMD calculation, isig = 20.

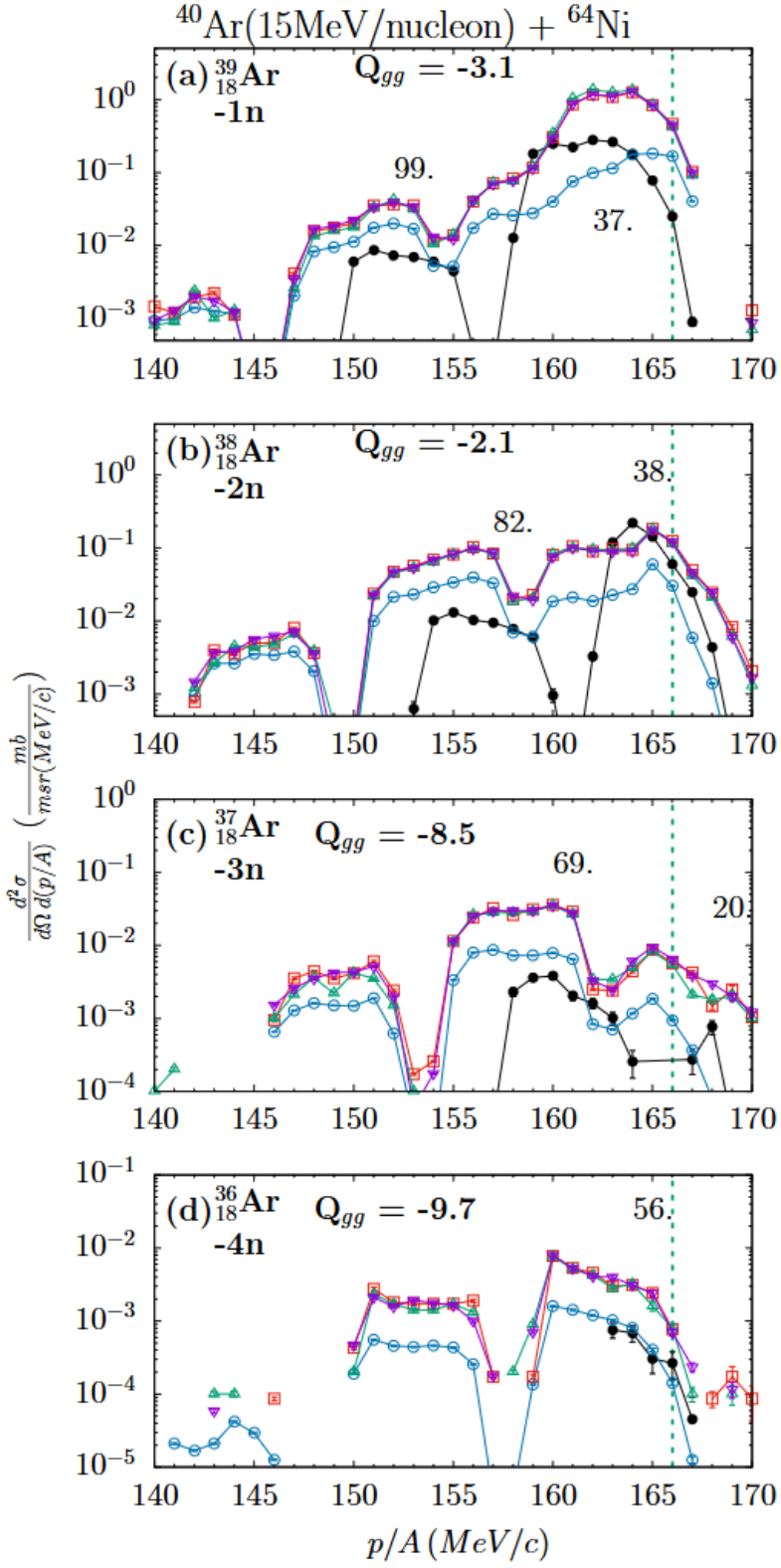

Figure 38: Momentum per nucleon distributions of projectile-like fragments for neutron removal channels. Black points: experimental data. Blue circles: DIT calculation. Red squares: CoMD calculation. The vertical dashed (green) lines indicate the velocity of the beam. Green triangles: CoMD calculations, with pair = 4. Purple inverse triangles: CoMD calculation, isig = 20.

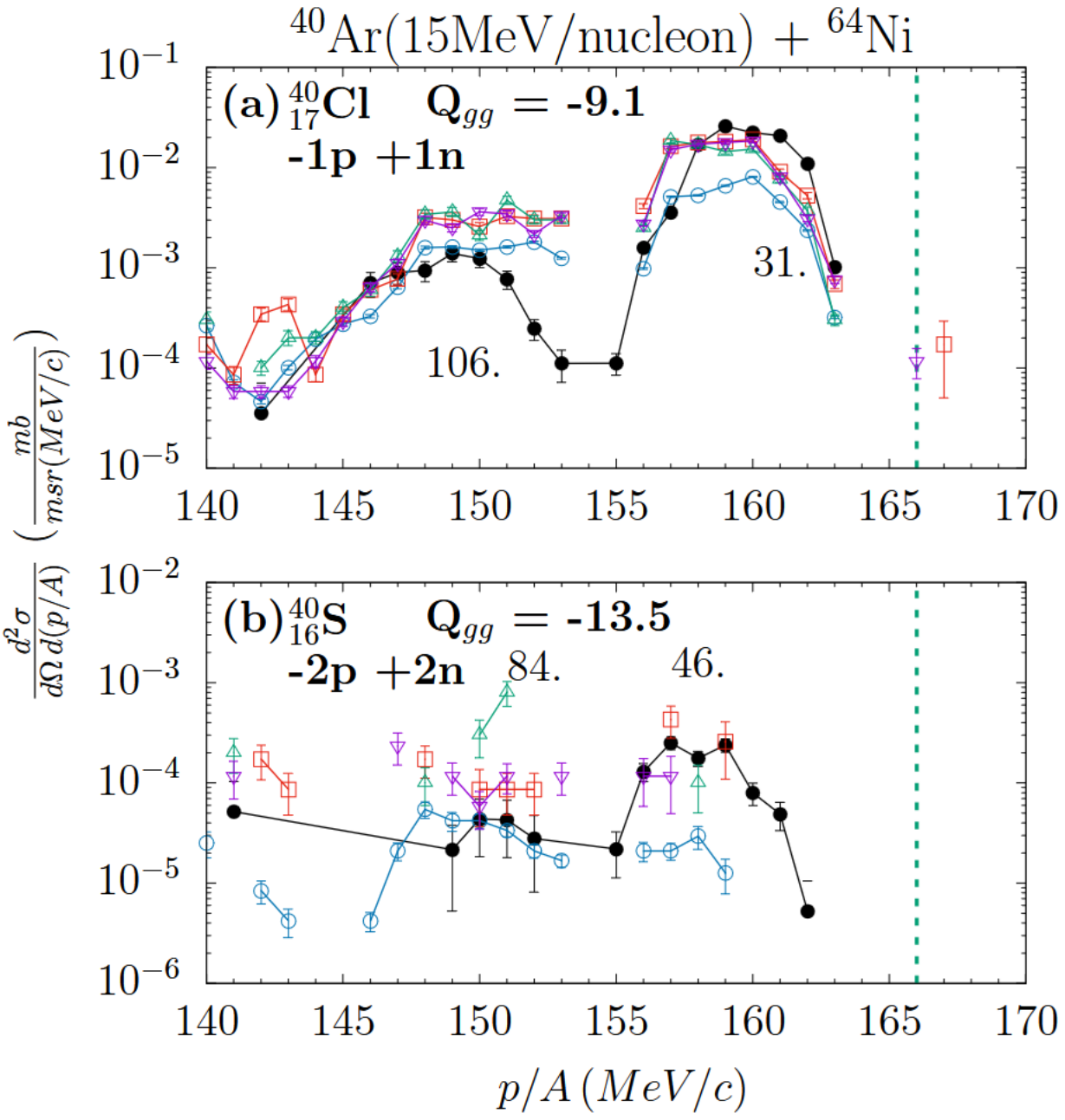

Figure 39: Momentum per nucleon distributions of projectile-like fragments for charge exchange channels. Black points: experimental data. Blue circles: DIT calculation. Red squares: CoMD calculation. The vertical dashed (green) lines indicate the velocity of the beam. Green triangles: CoMD calculations, with pair = 4. Purple inverse triangles: CoMD calculation, isig = 20.

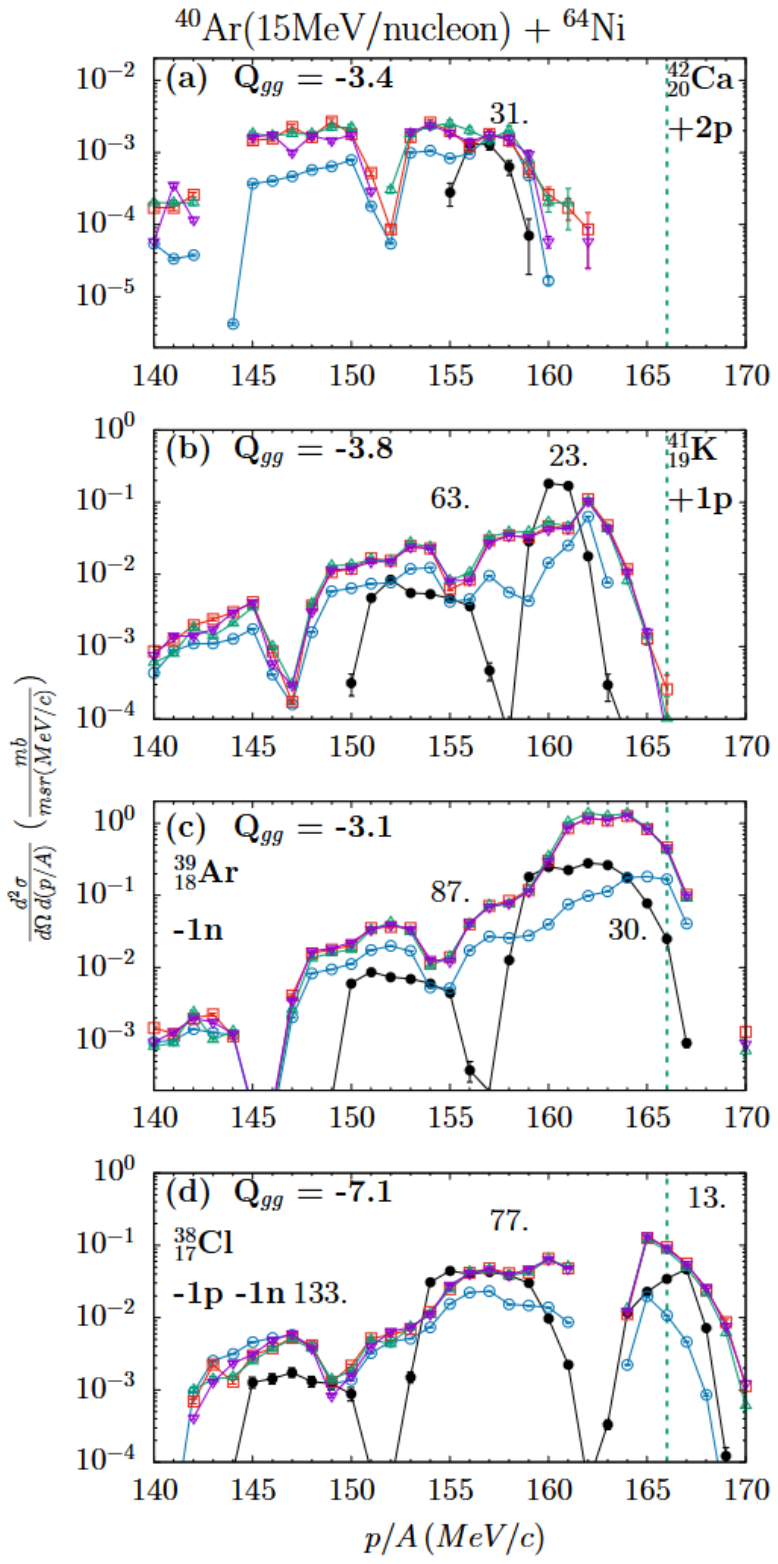

Figure 40: Momentum per nucleon distributions of projectile-like fragments for peak isotope channels (20 – 17). Black points: experimental data. Blue circles: DIT calculation. Red squares: CoMD calculation. The vertical dashed (green) lines indicate the velocity of the beam. Green triangles: CoMD calculations, with pair = 4. Purple inverse triangles: CoMD calculation, isig = 20.

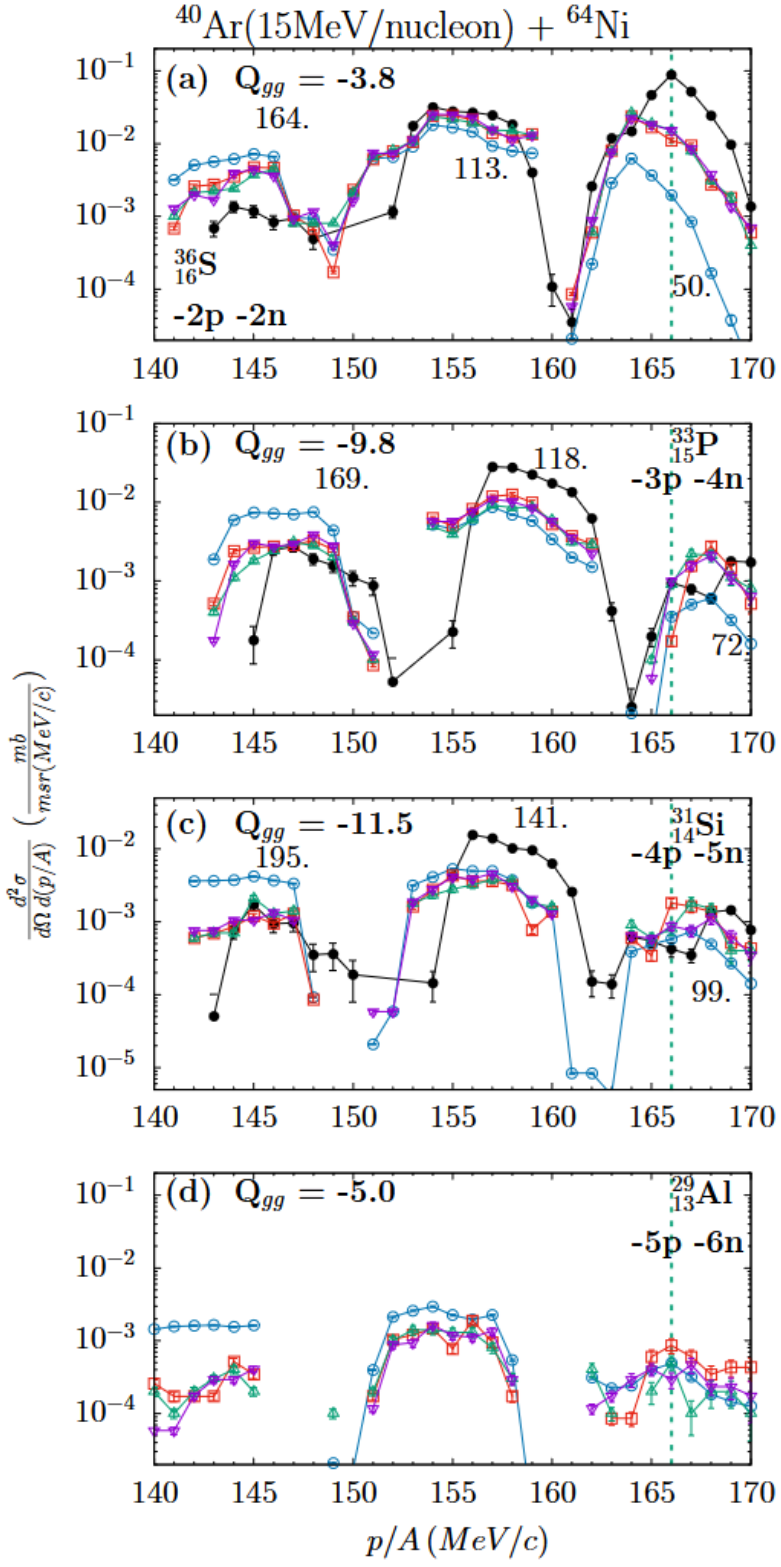

Figure 41: Momentum per nucleon distributions of projectile-like fragments for peak isotope channels (16 – 13). Black points: experimental data. Blue circles: DIT calculation. Red squares: CoMD calculation. The vertical dashed (green) lines indicate the velocity of the beam. Green triangles: CoMD calculations, with pair = 4. Purple inverse triangles: CoMD calculation, isig = 20.

In Figures 36 – 41 we can observe for all the channels of interest the experimental data, the DIT and standard CoMD calculations and their comparison with CoMD calculations with different parameters, pair = 4 and ISIG = 20. The experimental data are represented by black dots, the DIT calculation by blue circles, the CoMD calculation by red squares, the CoMD with pair = 4 calculations by green triangles and the CoMD with isig = 20 calculation by purple inverted triangles.

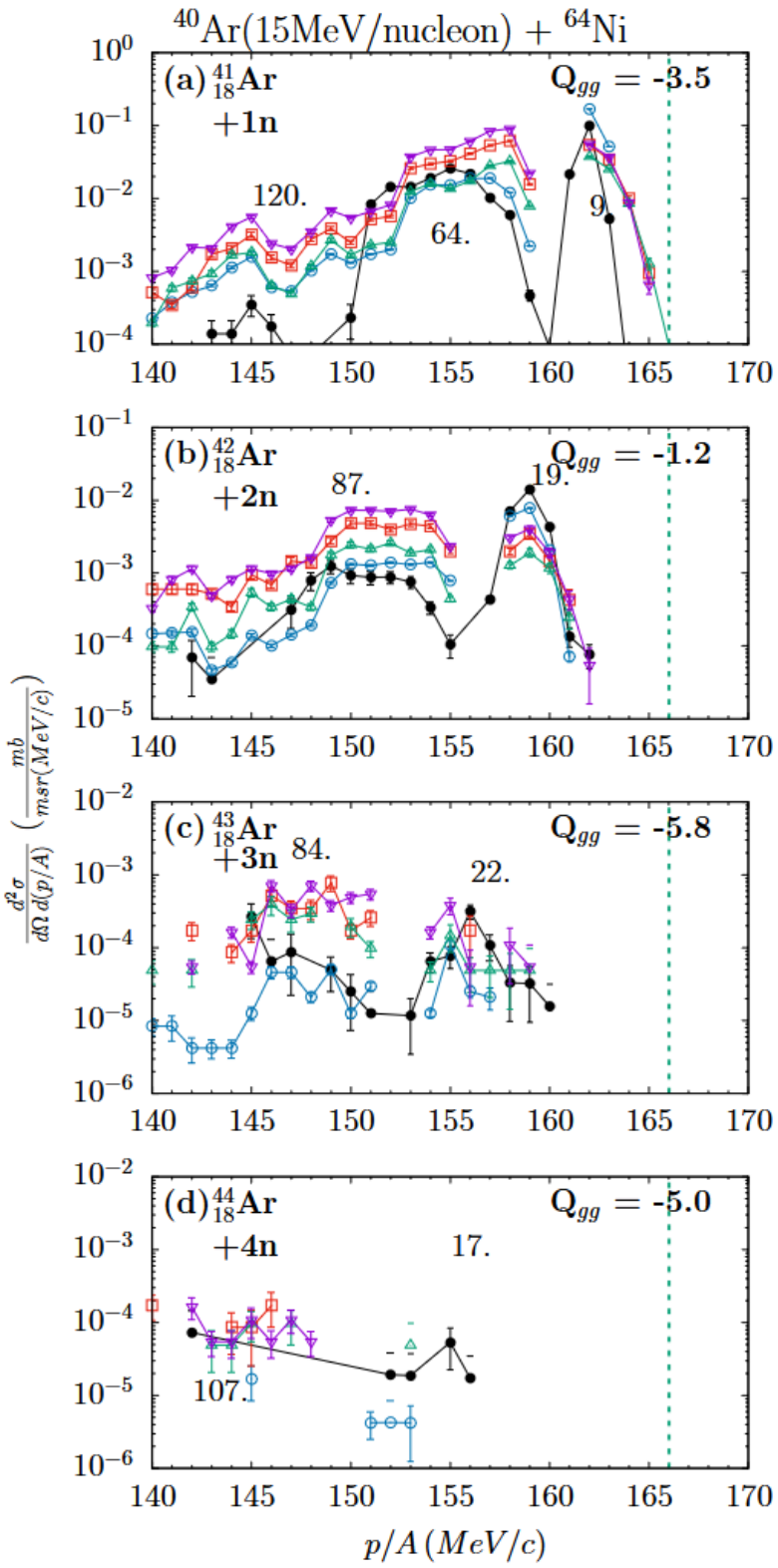

Figure 42: Momentum per nucleon distributions of projectile-like fragments for neutron pick-up channels. Black points: experimental data. Blue circles: DIT calculation. Red squares: CoMD calculation. The vertical dashed (green) lines indicate the velocity of the beam. Green triangles: CoMD calculations, with isyn = 1. Purple inverse triangles: CoMD calculation, isyn = 3.

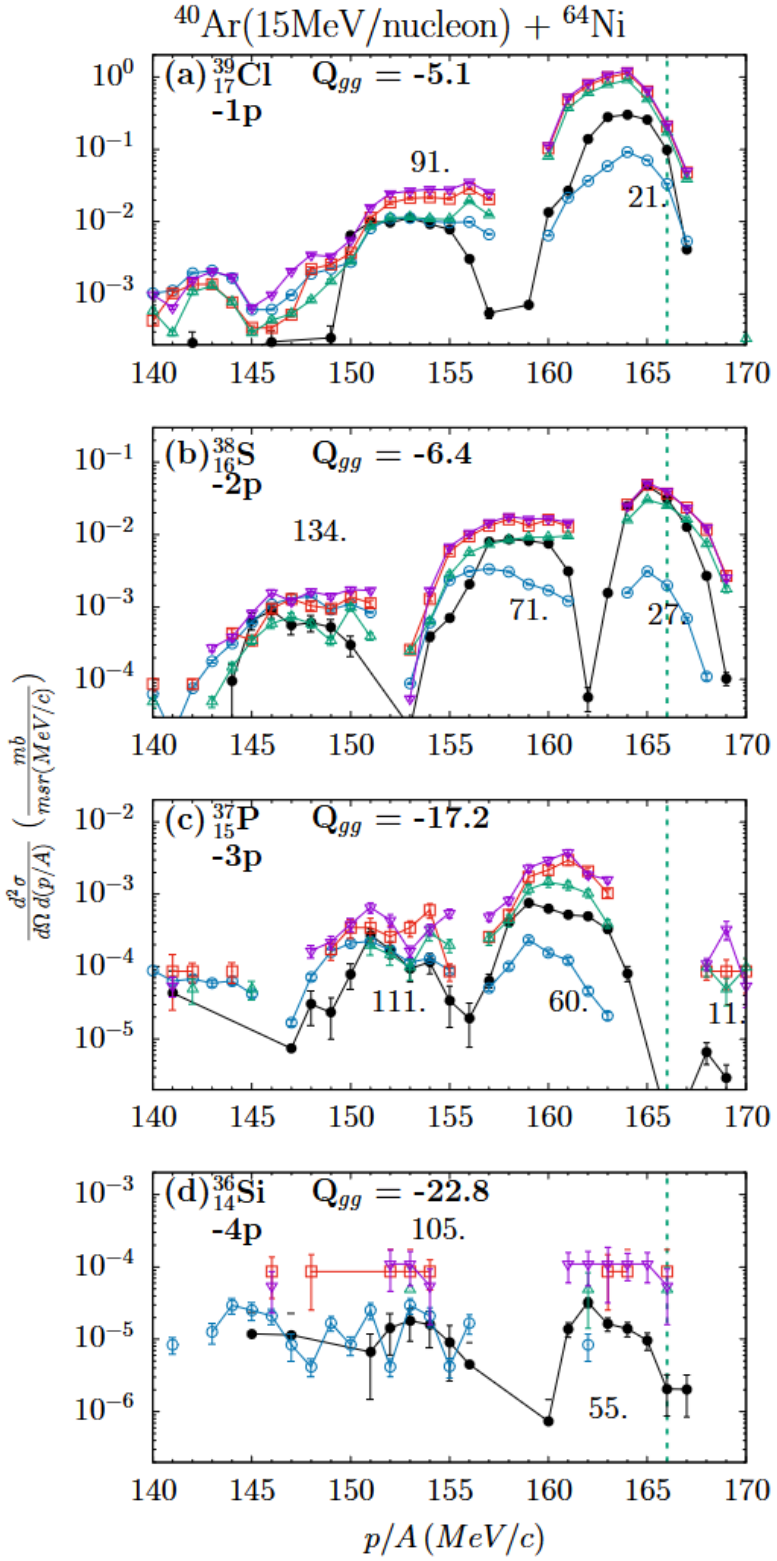

Figure 43: Momentum per nucleon distributions of projectile-like fragments for proton removal channels. Black points: experimental data. Blue circles: DIT calculation. Red squares: CoMD calculation. The vertical dashed (green) lines indicate the velocity of the beam. Green triangles: CoMD calculations, with isyn = 1. Purple inverse triangles: CoMD calculation, isyn = 3.

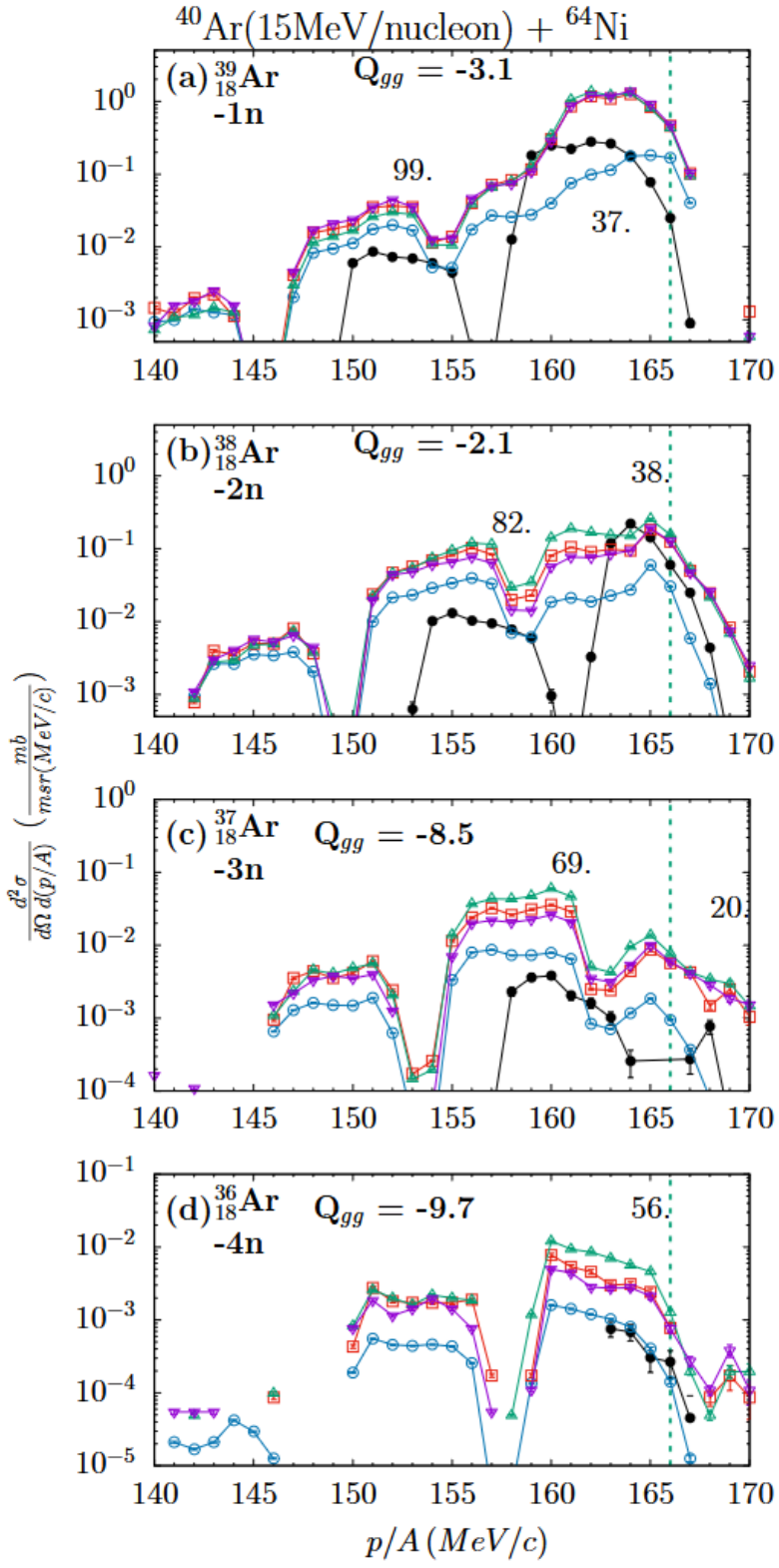

Figure 44: Momentum per nucleon distributions of projectile-like fragments for neutron removal channels. Black points: experimental data. Blue circles: DIT calculation. Red squares: CoMD calculation. The vertical dashed (green) lines indicate the velocity of the beam. Green triangles: CoMD calculations, with isyn = 1. Purple inverse triangles: CoMD calculation, isyn = 3.

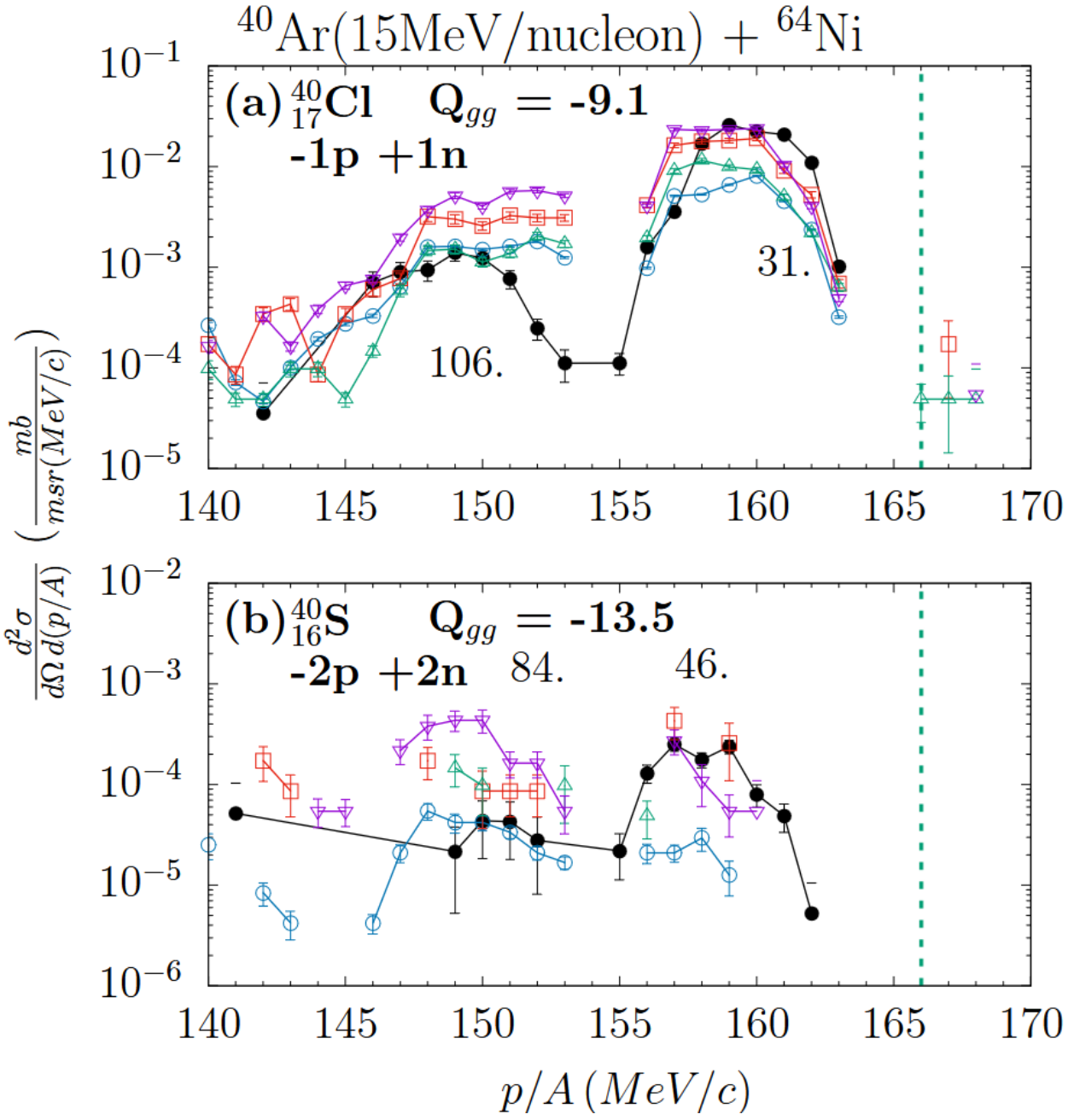

Figure 45: Momentum per nucleon distributions of projectile-like fragments for charge exchange channels. Black points: experimental data. Blue circles: DIT calculation. Red squares: CoMD calculation. The vertical dashed (green) lines indicate the velocity of the beam. Green triangles: CoMD calculations, with isyn = 1. Purple inverse triangles: CoMD calculation, isyn = 3.

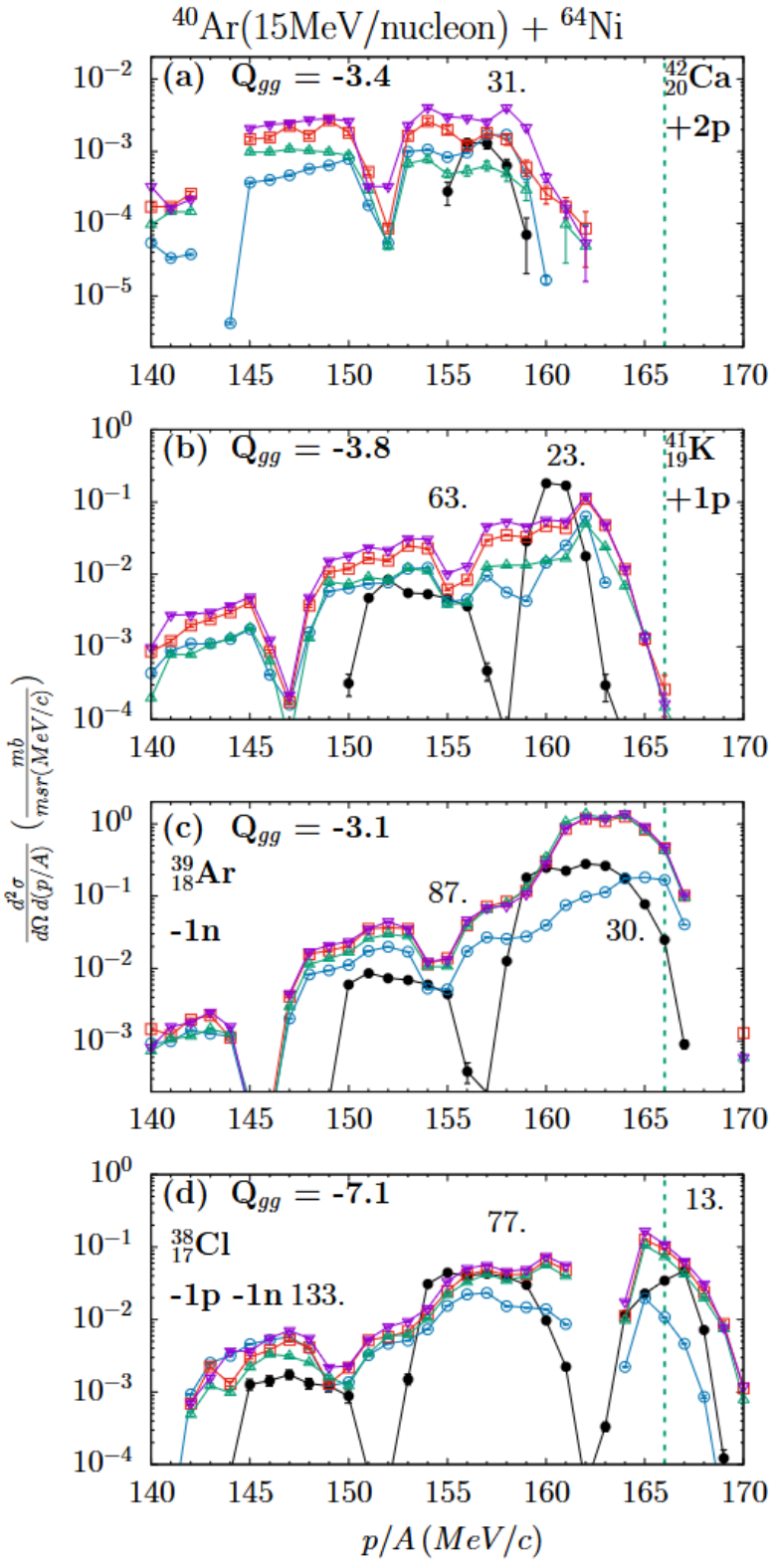

Figure 46: Momentum per nucleon distributions of projectile-like fragments for peak isotope channels (20 – 17). Black points: experimental data. Blue circles: DIT calculation. Red squares: CoMD calculation. The vertical dashed (green) lines indicate the velocity of the beam. Green triangles: CoMD calculations, with isyn = 1. Purple inverse triangles: CoMD calculation, isyn = 3.

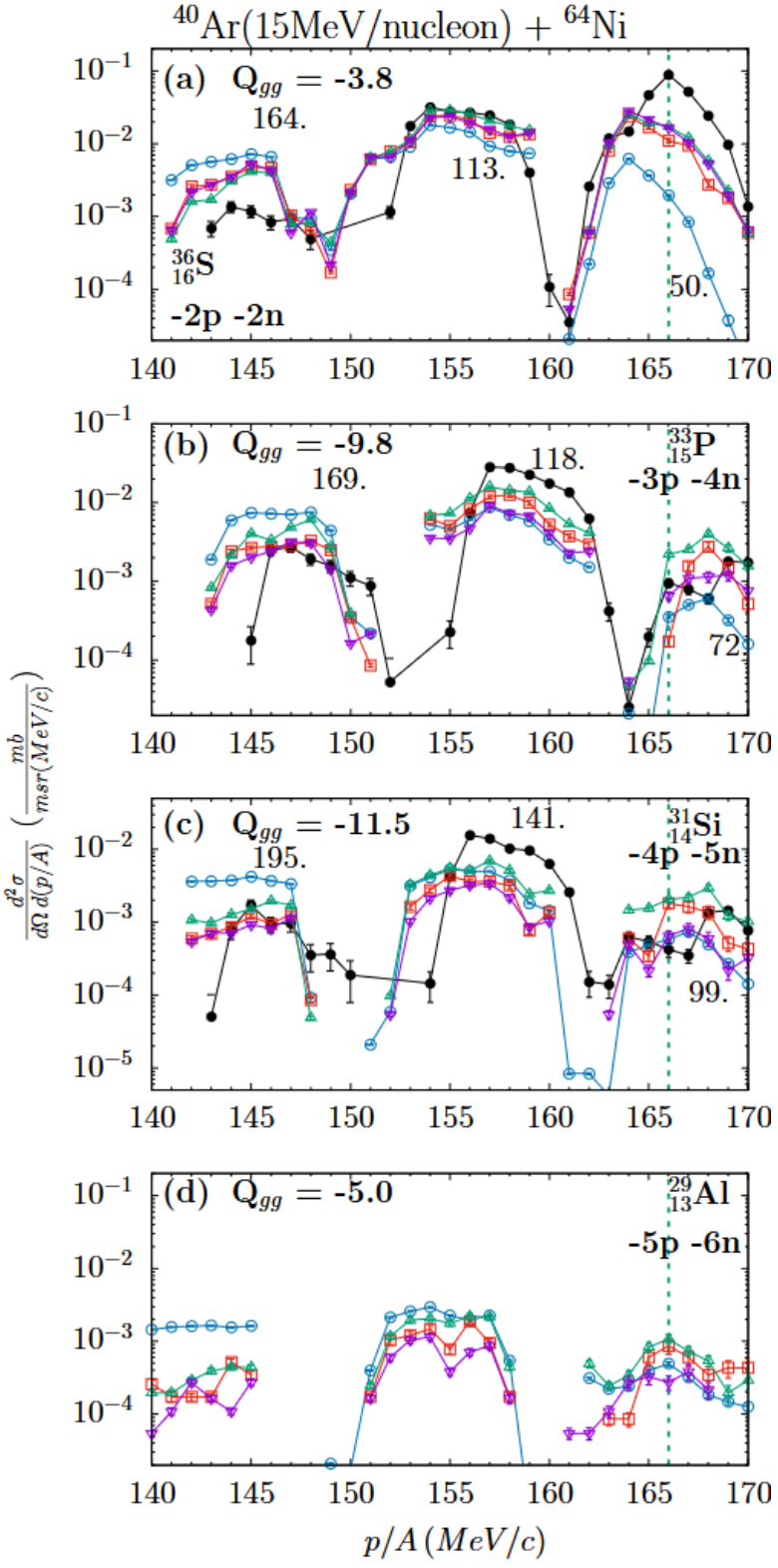

Figure 47: Momentum per nucleon distributions of projectile-like fragments for peak isotope channels (16 – 13). Black points: experimental data. Blue circles: DIT calculation. Red squares: CoMD calculation. The vertical dashed (green) lines indicate the velocity of the beam. Green triangles: CoMD calculations, with isyn = 1. Purple inverse triangles: CoMD calculation, isyn = 3.

In Figures 42 – 47 we can observe for all the channels of interest the experimental data, the DIT and standard CoMD calculations and their comparison with CoMD calculations with different parameters, isyn = 1 and isyn = 3. The experimental data are represented by black dots, the DIT calculation by blue circles, the CoMD calculation by red squares, the CoMD with isyn = 1 calculations by green triangles and the CoMD with isyn = 3 calculation by purple inverted triangles.

This subsection compares the momentum distributions of the experimental data (represented by black points) with the DIT model calculations for the de-excited, final fragments (depicted as blue solid lines) for each channel studied. Across all channels, the DIT calculations exhibit a general tendency to underestimate the experimental data, particularly in the quasi-elastic region of the distribution. This region, corresponding to lower excitation energies of the projectile-target system, is the primary focus of our study. This discrepancy arises because the DIT model, being phenomenological in nature, provides a more accurate description of the deep inelastic part of the distributions rather than the quasi-elastic part.

We also compare the momentum distributions of the experimental data with CoMD model calculations for the de-excited, final fragments across the same channels. The primary objective of this comparison is to evaluate the CoMD model.

In most cases, the standard CoMD calculations provide a reasonable description of the experimental data; however, they tend to underestimate the distributions overall. Notably, discrepancies are evident in the right-hand region of the momentum distributions, particularly in the quasi-elastic part, where the experimental data and calculations diverge. These discrepancies highlight areas where the CoMD model can be further refined to better align with experimental observations.

5.3 Angular Distributions

In the following part of this project we present angular distributions for all the channels of interest, the neutron pickup channels, from +1 to +4 neutrons, the proton removal channels, from -1 to -4 protons, the neutron removal channels from -1 to -4 neutrons, the single and double charge exchange channels and the peak isotope channels for Z= 20 to Z = 13. In these figures the x-axis represent the angle of the quasi projectile moving away from the target and in the y-axis the differential cross section with respect to solid angle, dΩ in units, mb/msr. The MARS experimental apparatus measures in only one angle, 4°±1.8°, so we have only one experimental point at each channel, represented by the black point. In each channel we also present the Rutherford scattering shown by black circles. The blue circles represent the DIT calculations, the red squares the standard CoMD calculations.

In Figures 48 – 53 the green triangles represent the CoMD calculations with K = 200 MeV and the inverted purple triangles the CoMD calculations with K = 308 MeV.

In Figures 54 – 59 the green triangles represent the CoMD calculations with isyn = 1 and the inverted purple triangles represent the CoMD calculations with isyn = 3.

In most cases, the DIT calculations seen to be slightly more efficient in describing the experimental data and in some channels the CoMD calculations with K = 200 MeV perform adequately. It is also worthy to mention that CoMD calculations with isyn = 1 perform well in some channels.

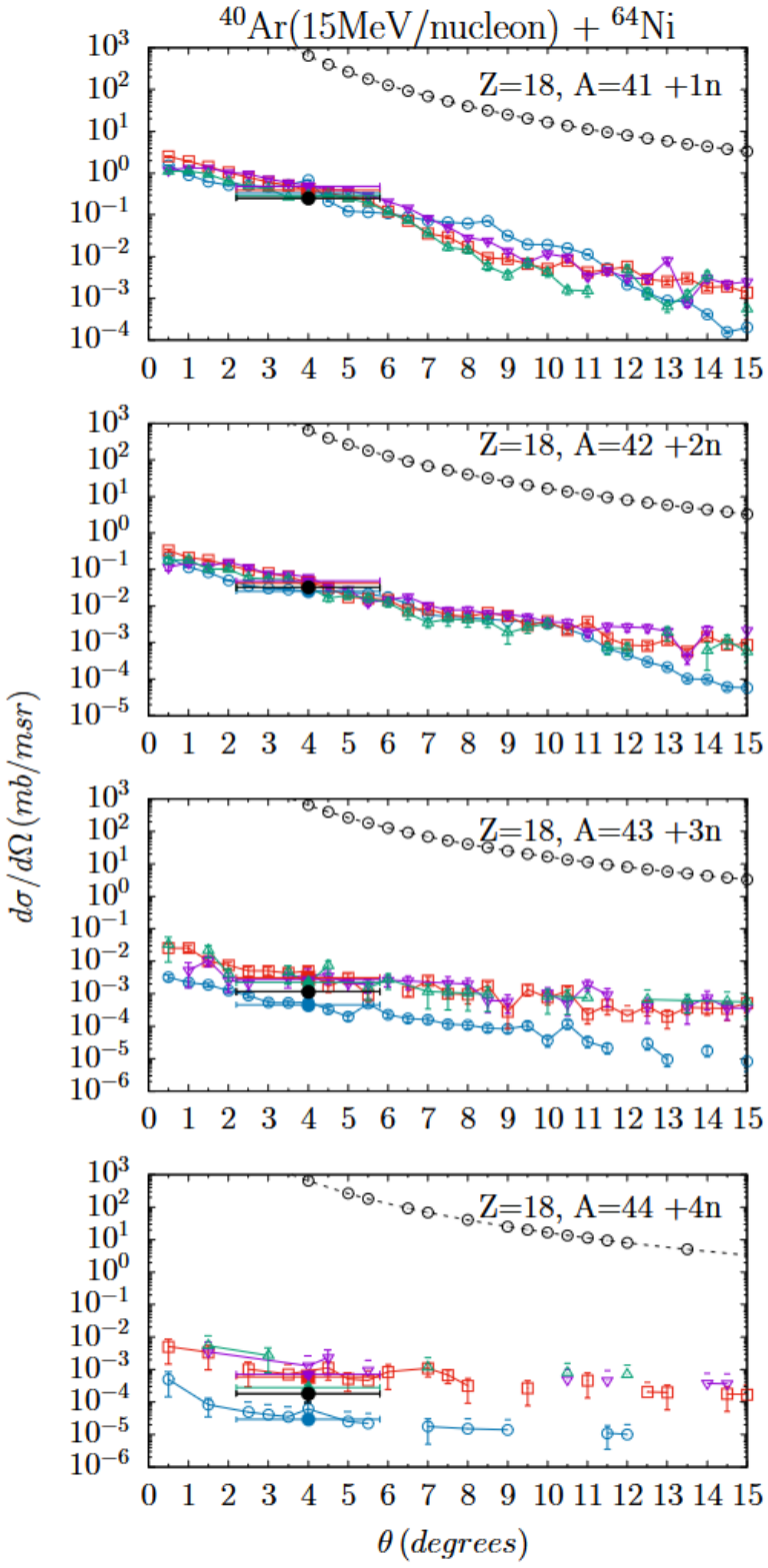

Figure 48: Angular distributions of projectile-like fragments for neutron pick-up channels. Black circles: Rutherford scattering. Black points: Experimental data. Blue circles: DIT calculation. Red squares: CoMD calculation, with K = 254 MeV. Green triangles: CoMD calculations, with K = 200 MeV. Purple inverse triangles: CoMD calculation, with K = 308 MeV.

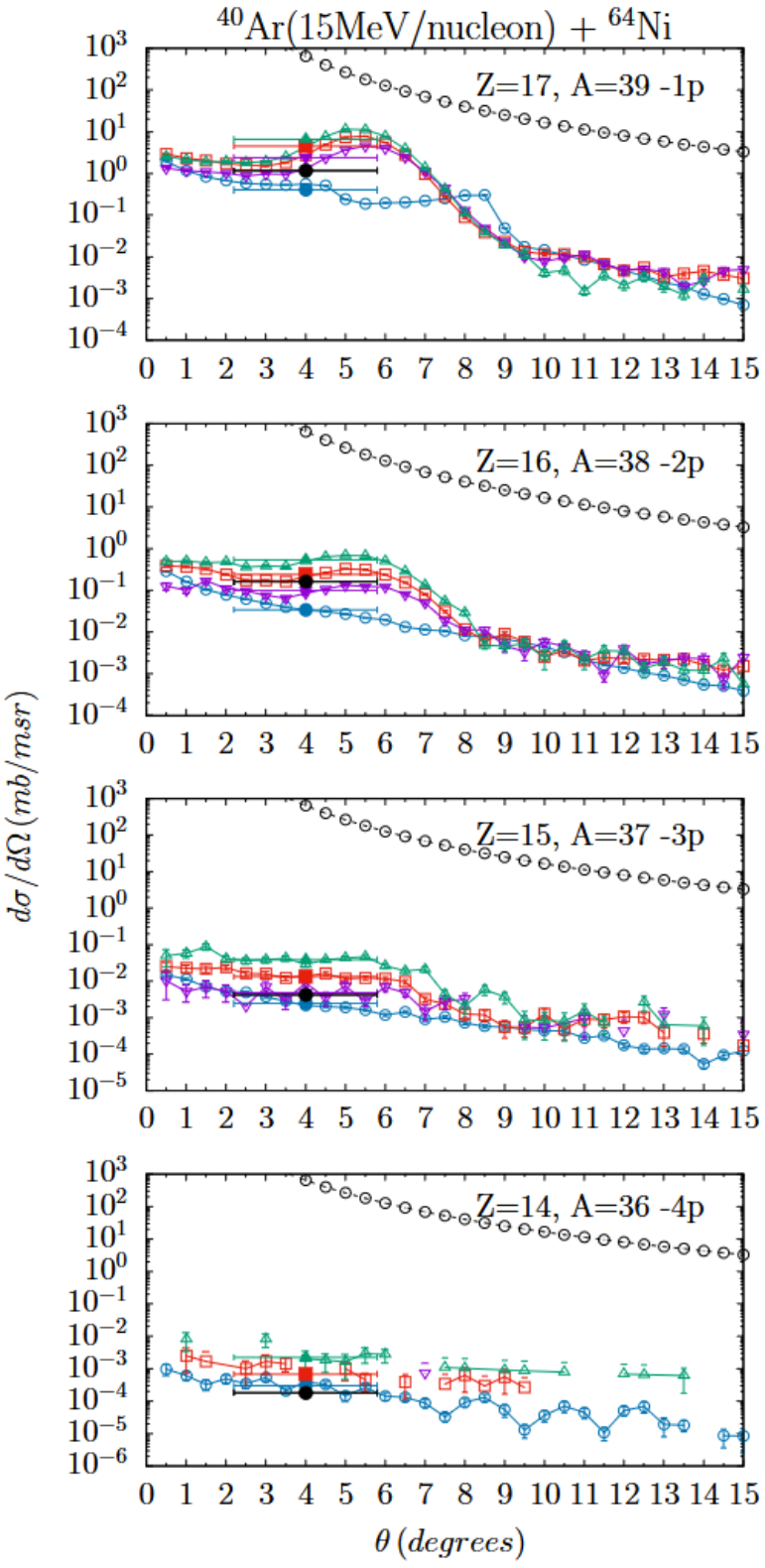

Figure 49: Angular distributions of projectile-like fragments for proton removal channels. Black circles: Rutherford scattering. Black points: Experimental data. Blue circles: DIT calculation. Red squares: CoMD calculation, with K = 254 MeV. Green triangles: CoMD calculations, with K = 200 MeV. Purple inverse triangles: CoMD calculation, with K = 308 MeV.

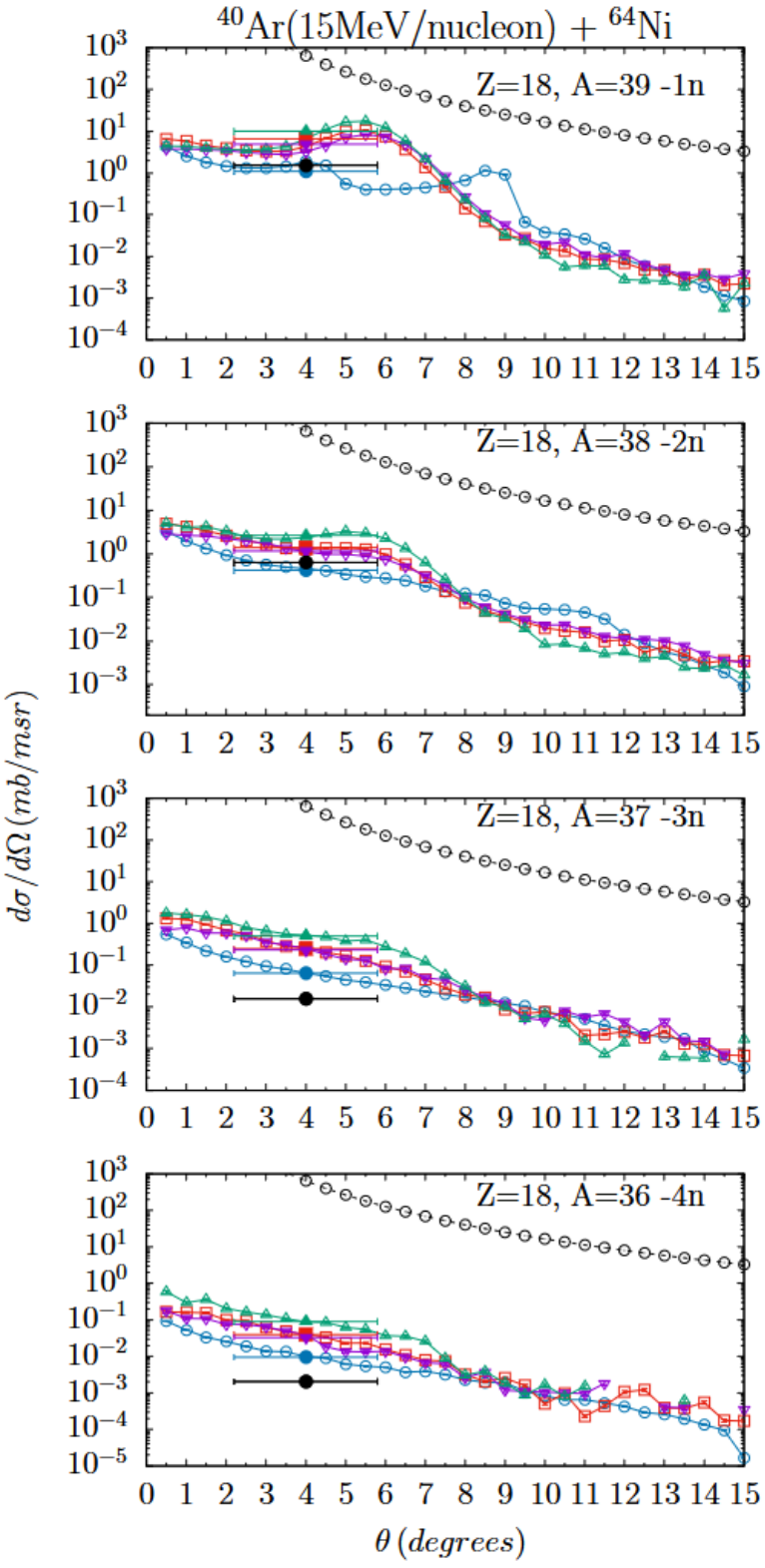

Figure 50: Angular distributions of projectile-like fragments for neutron removal channels. Black circles: Rutherford scattering. Black points: Experimental data. Blue circles: DIT calculation. Red squares: CoMD calculation, with K = 254 MeV. Green triangles: CoMD calculations, with K = 200 MeV. Purple inverse triangles: CoMD calculation, with K = 308 MeV.

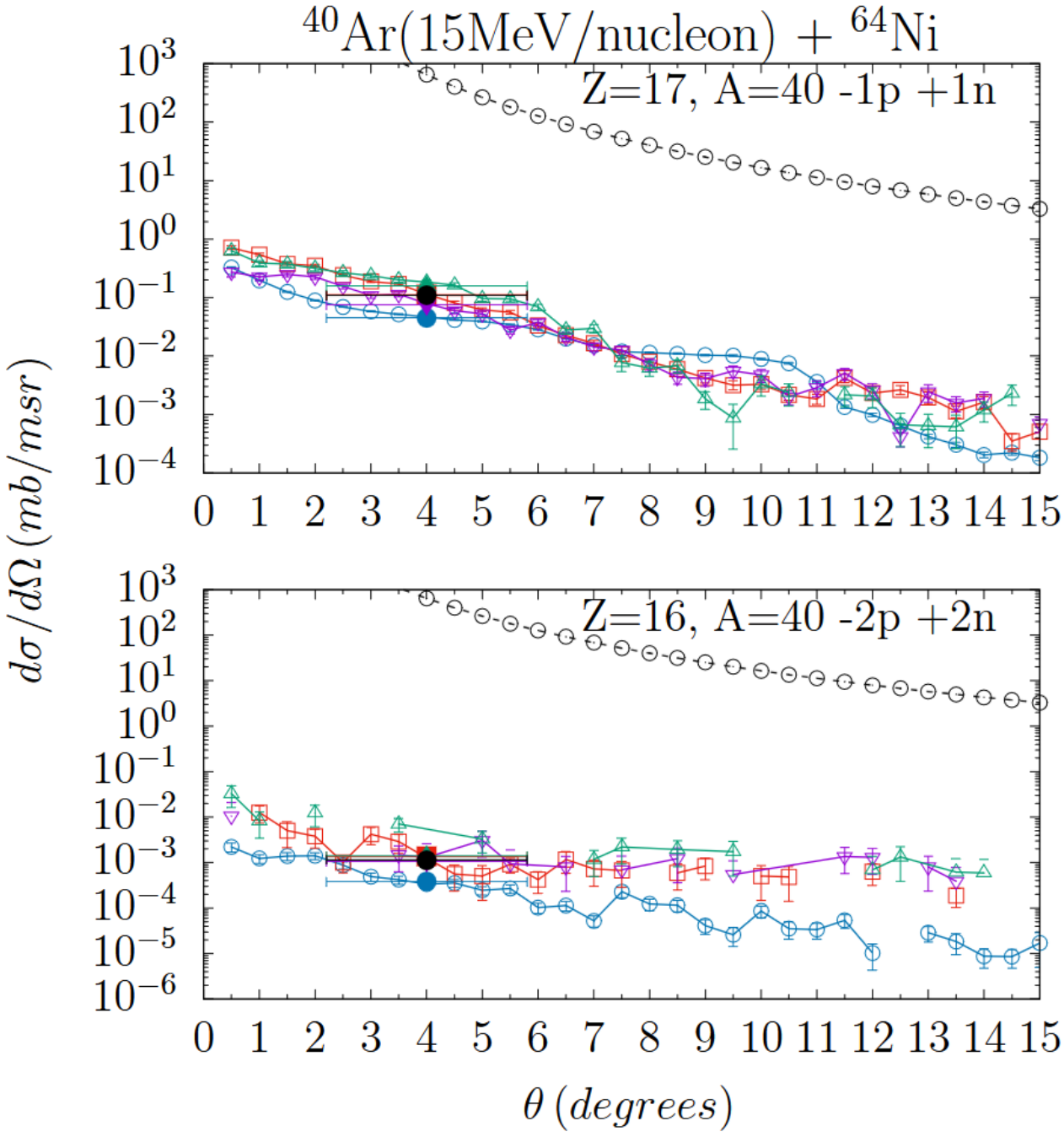

Figure 51: Angular distributions of projectile-like fragments for charge exchange channels. Black circles: Rutherford scattering. Black points: Experimental data. Blue circles: DIT calculation. Red squares: CoMD calculation, with K = 254 MeV. Green triangles: CoMD calculations, with K = 200 MeV. Purple inverse triangles: CoMD calculation, with K = 308 MeV.

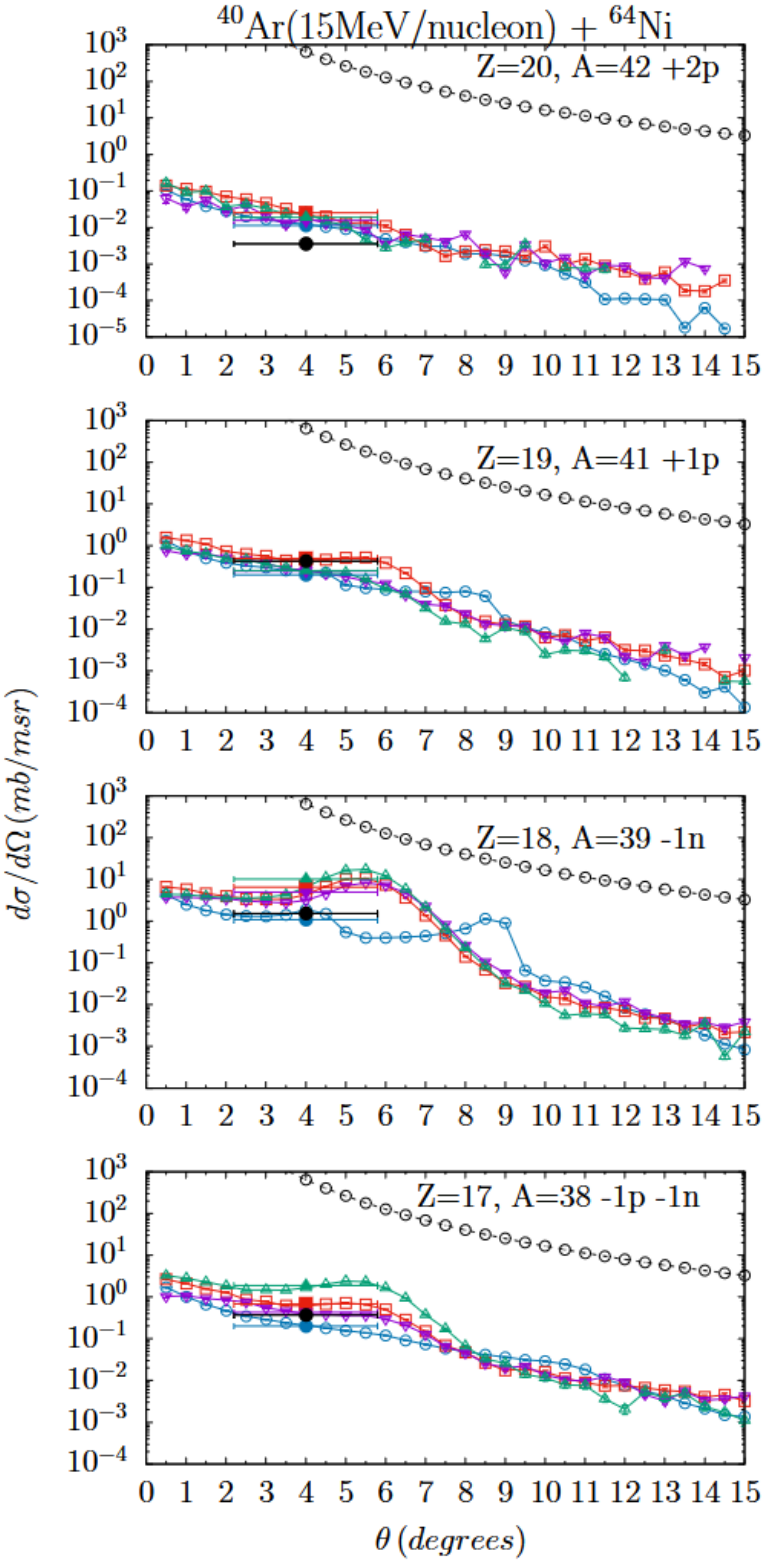

Figure 52: Angular distributions of projectile-like fragments for peak isotope channels (20 – 17). Black circles: Rutherford scattering. Black points: Experimental data. Blue circles: DIT calculation. Red squares: CoMD calculation, with K = 254 MeV. Green triangles: CoMD calculations, with K = 200 MeV. Purple inverse triangles: CoMD calculation, with K = 308 MeV.

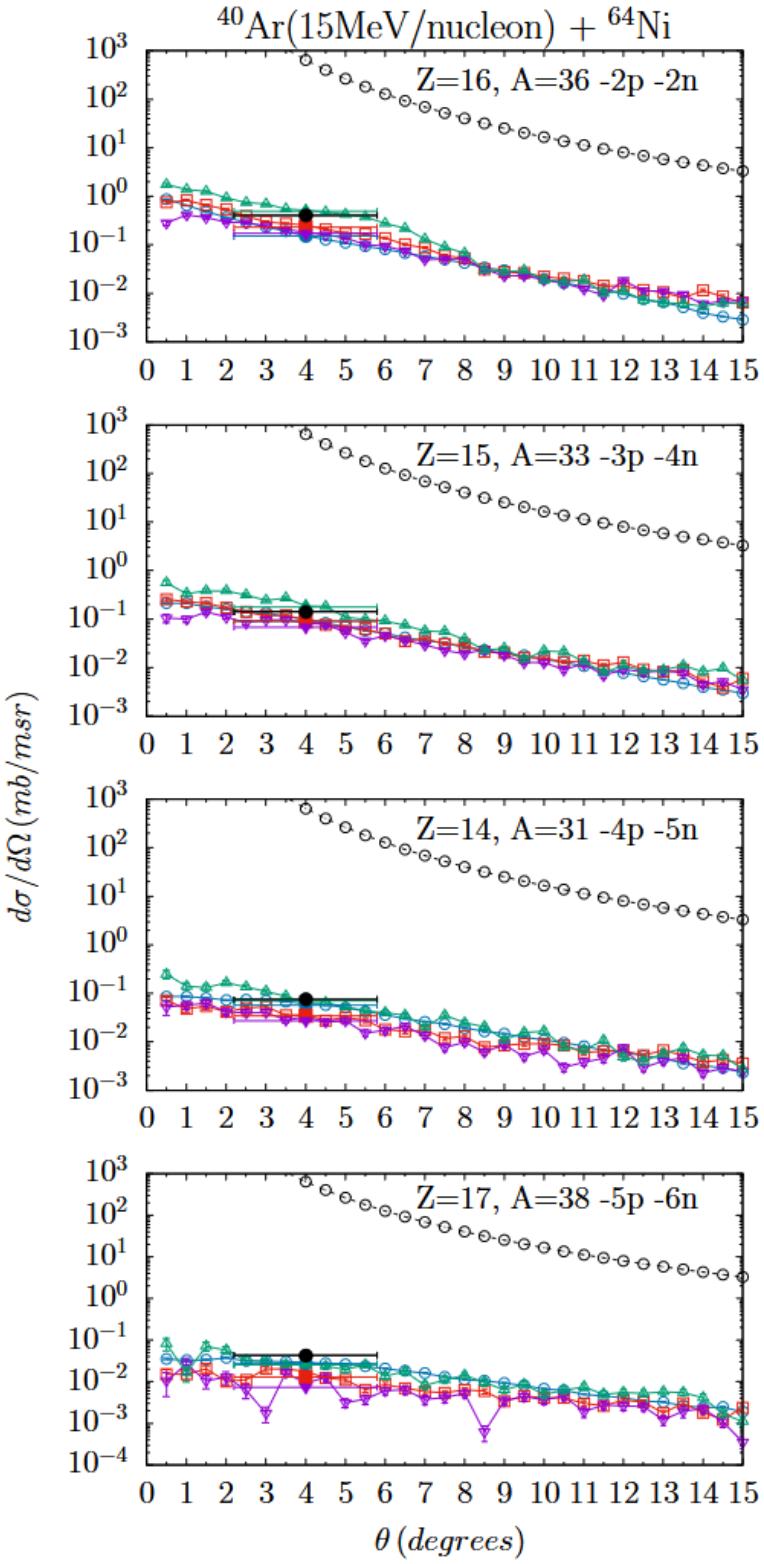

Figure 53: Angular distributions of projectile-like fragments for peak isotope channels (16 – 13). Black circles: Rutherford scattering. Black points: Experimental data. Blue circles: DIT calculation. Red squares: CoMD calculation, with K = 254 MeV. Green triangles: CoMD calculations, with K = 200 MeV. Purple inverse triangles: CoMD calculation, with K = 308 MeV.

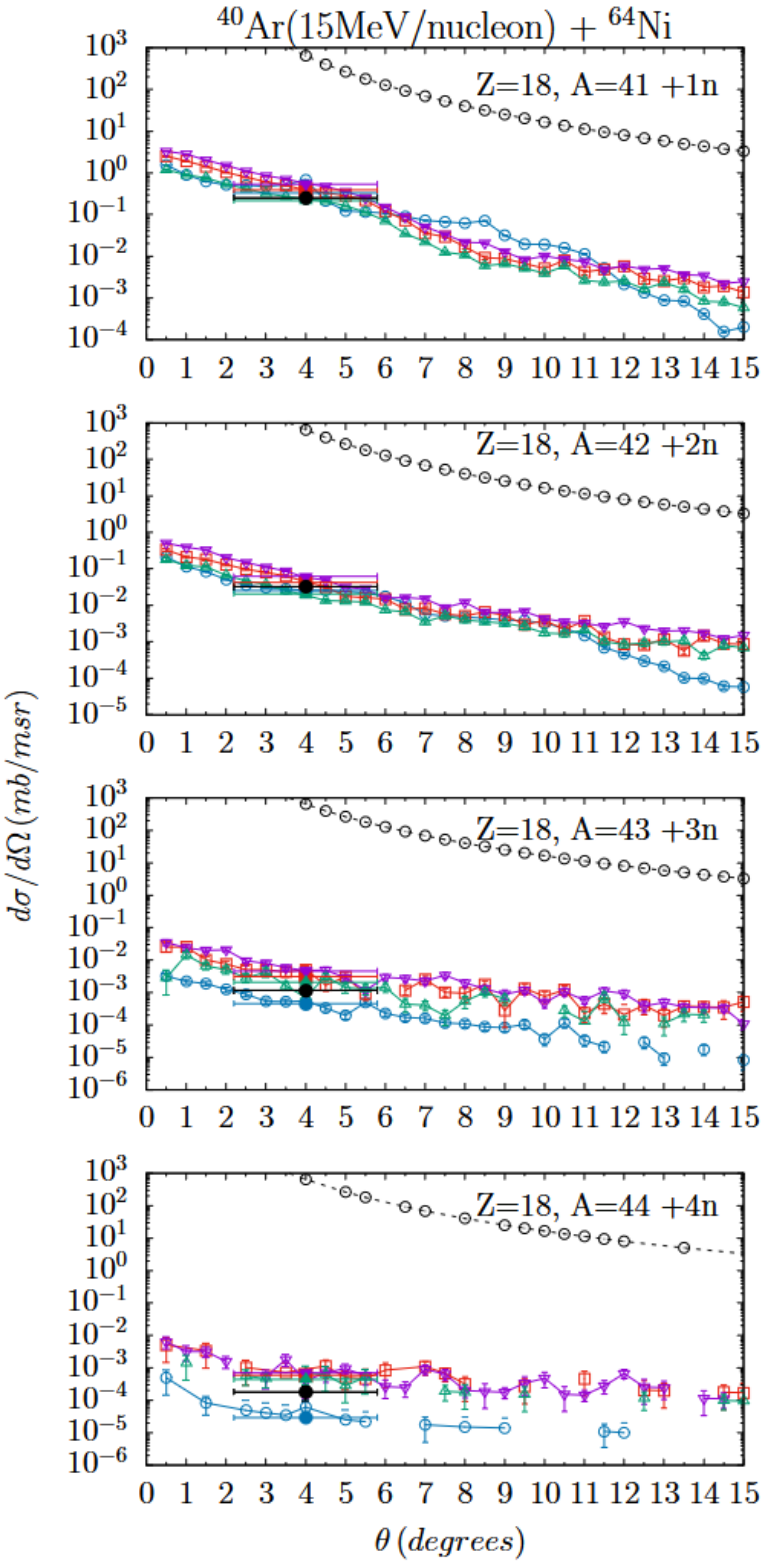

Figure 54: Angular distributions of projectile-like fragments for neutron pick-up channels. Black circles: Rutherford scattering. Black points: Experimental data. Blue circles: DIT calculation. Red squares: CoMD calculation, with isyn = 2. Green triangles: CoMD calculations, with isyn = 1. Purple inverse triangles: CoMD calculation, with isyn = 3.

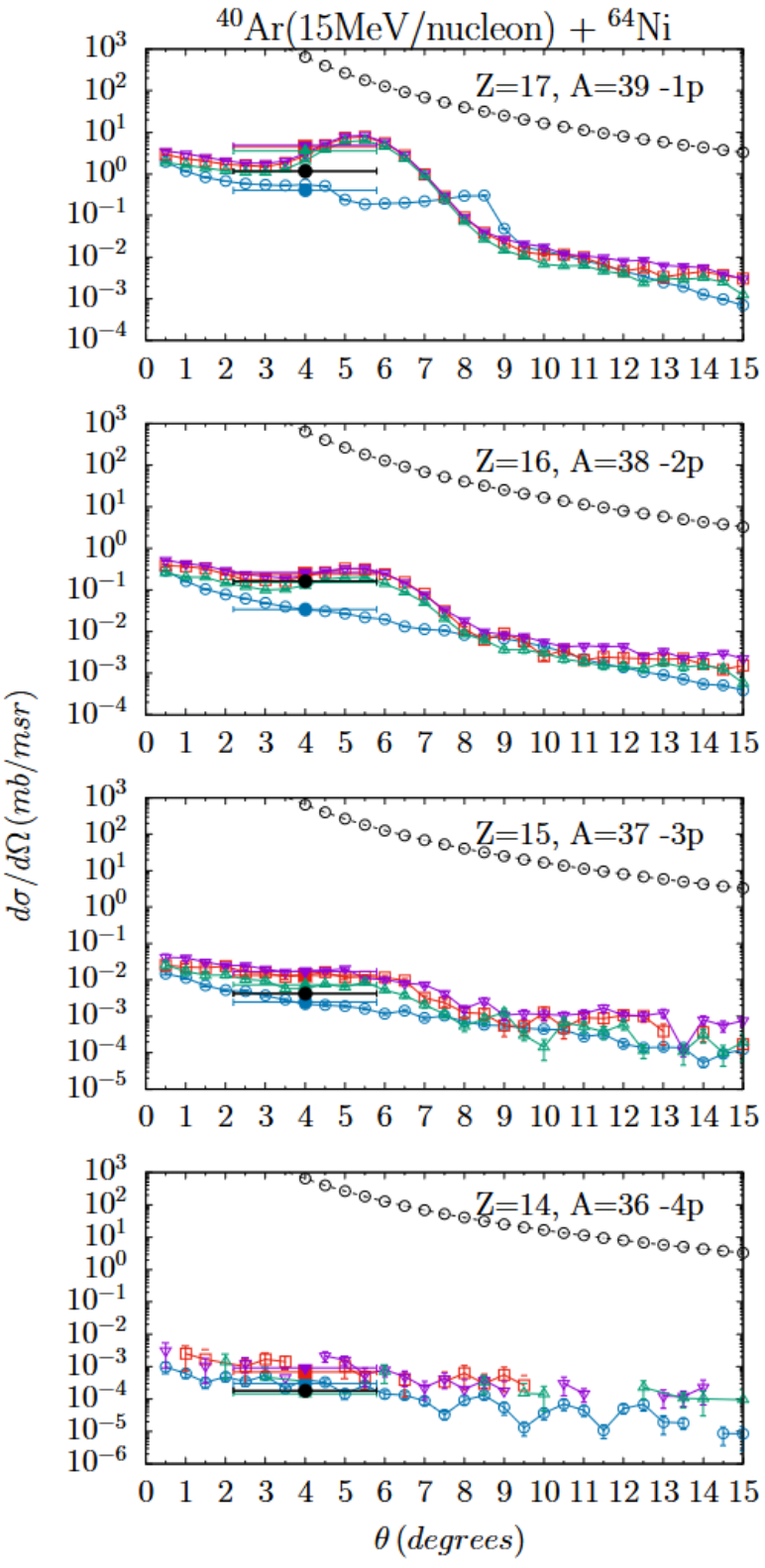

Figure 55: Angular distributions of projectile-like fragments for proton removal channels. Black circles: Rutherford scattering. Black points: Experimental data. Blue circles: DIT calculation. Red squares: CoMD calculation, with isyn = 2. Green triangles: CoMD calculations, with isyn = 1. Purple inverse triangles: CoMD calculation, with isyn = 3.

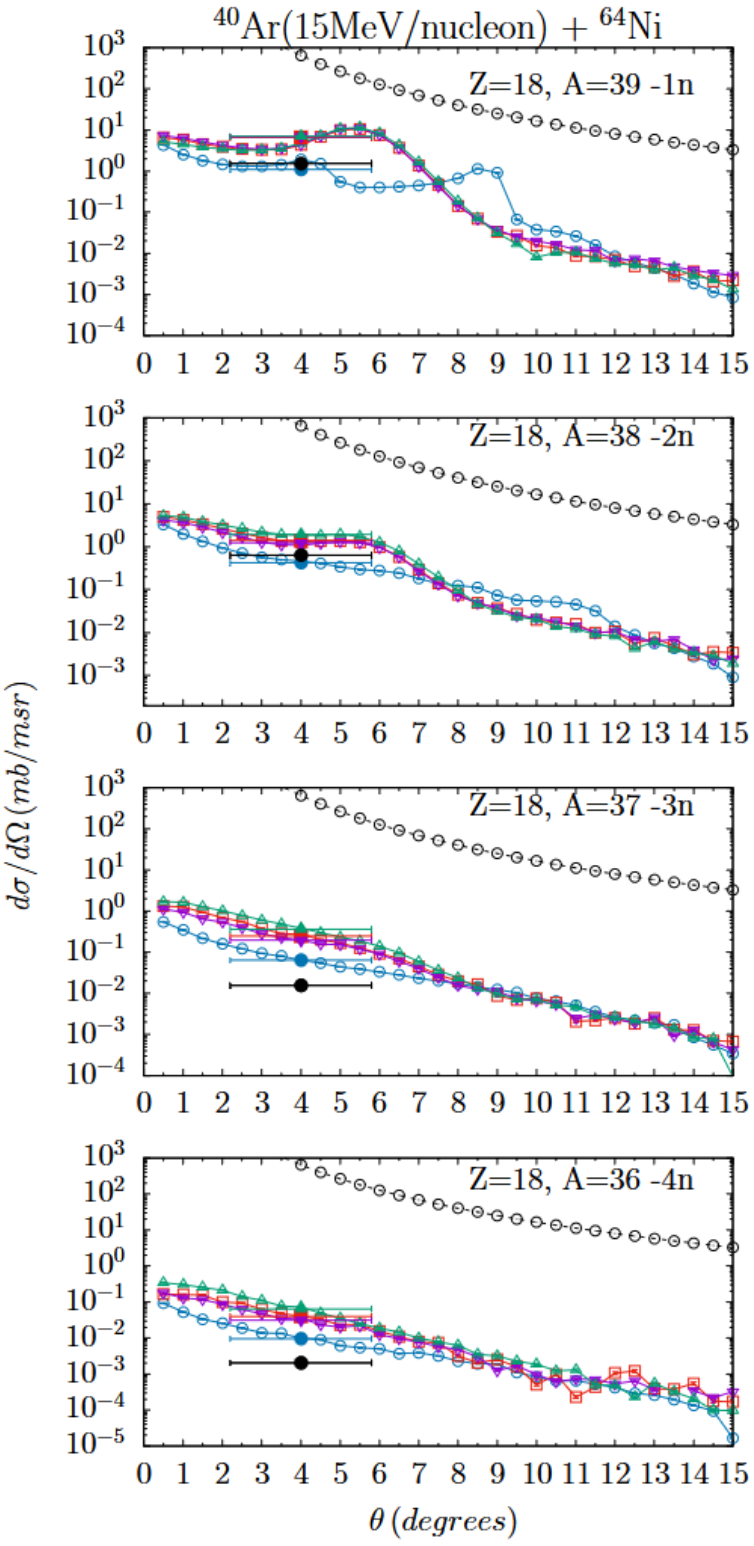

Figure 56: Angular distributions of projectile-like fragments for neutron removal channels. Black circles: Rutherford scattering. Black points: Experimental data. Blue circles: DIT calculation. Red squares: CoMD calculation, with isyn = 2. Green triangles: CoMD calculations, with isyn = 1. Purple inverse triangles: CoMD calculation, with isyn = 3.

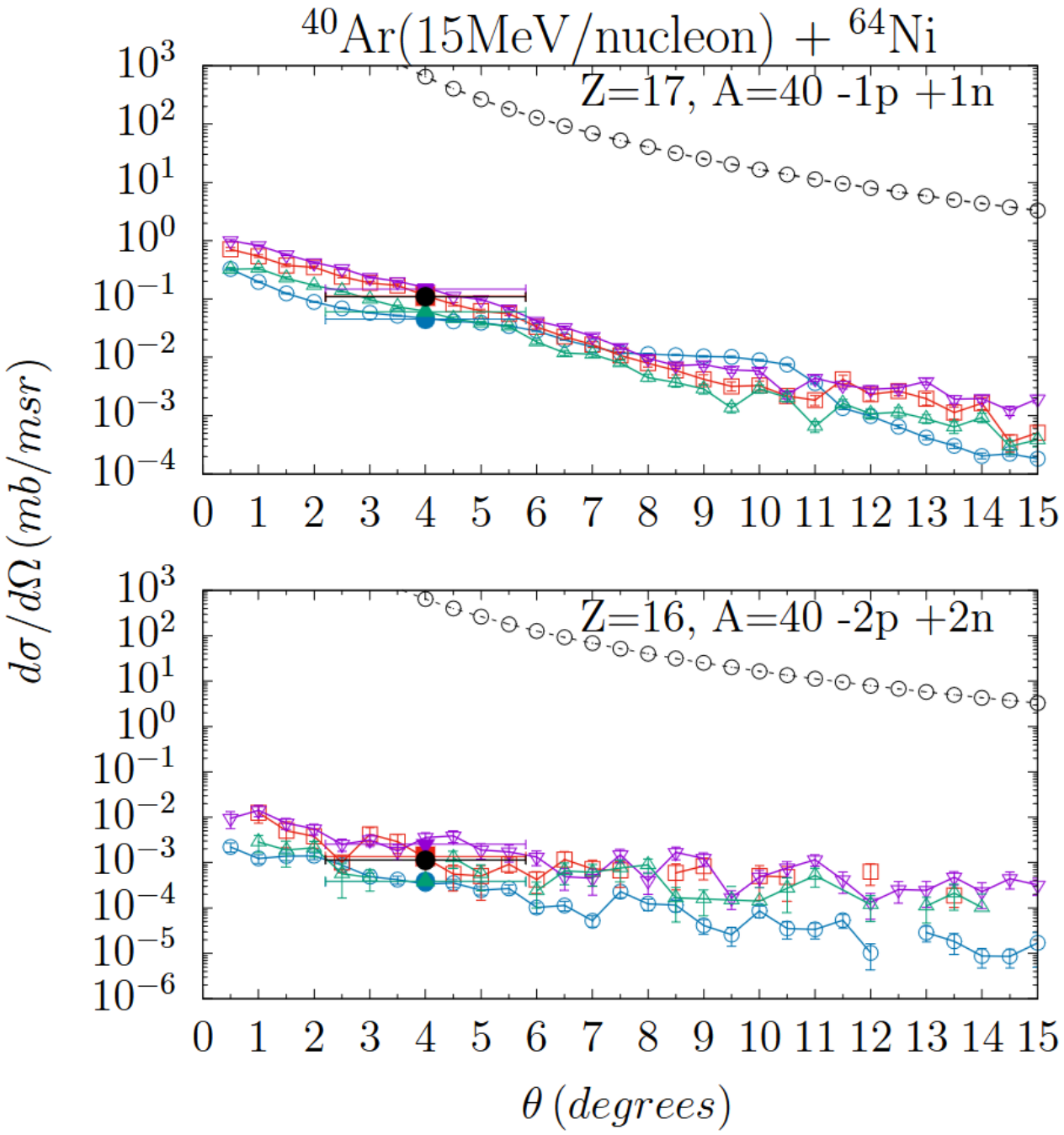

Figure 57: Angular distributions of projectile-like fragments for charge exchange channels. Black circles: Rutherford scattering. Black points: Experimental data. Blue circles: DIT calculation. Red squares: CoMD calculation, with isyn = 2. Green triangles: CoMD calculations, with isyn = 1. Purple inverse triangles: CoMD calculation, with isyn = 3.

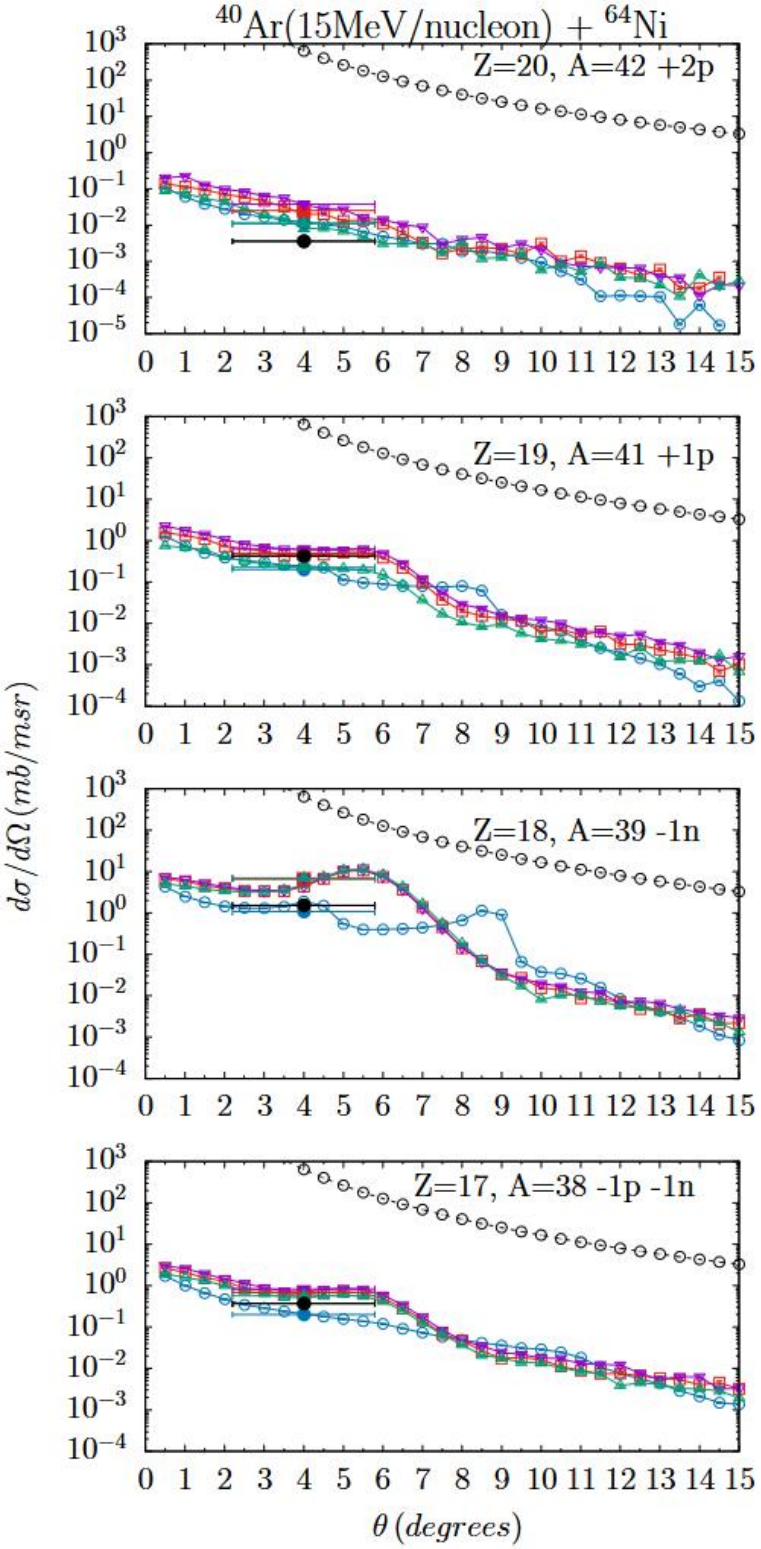

Figure 58: Angular distributions of projectile-like fragments for peak isotope channels (20 – 17). Black circles: Rutherford scattering. Black points: Experimental data. Blue circles: DIT calculation. Red squares: CoMD calculation, with isyn = 2. Green triangles: CoMD calculations, with isyn = 1. Purple inverse triangles: CoMD calculation, with isyn = 3.

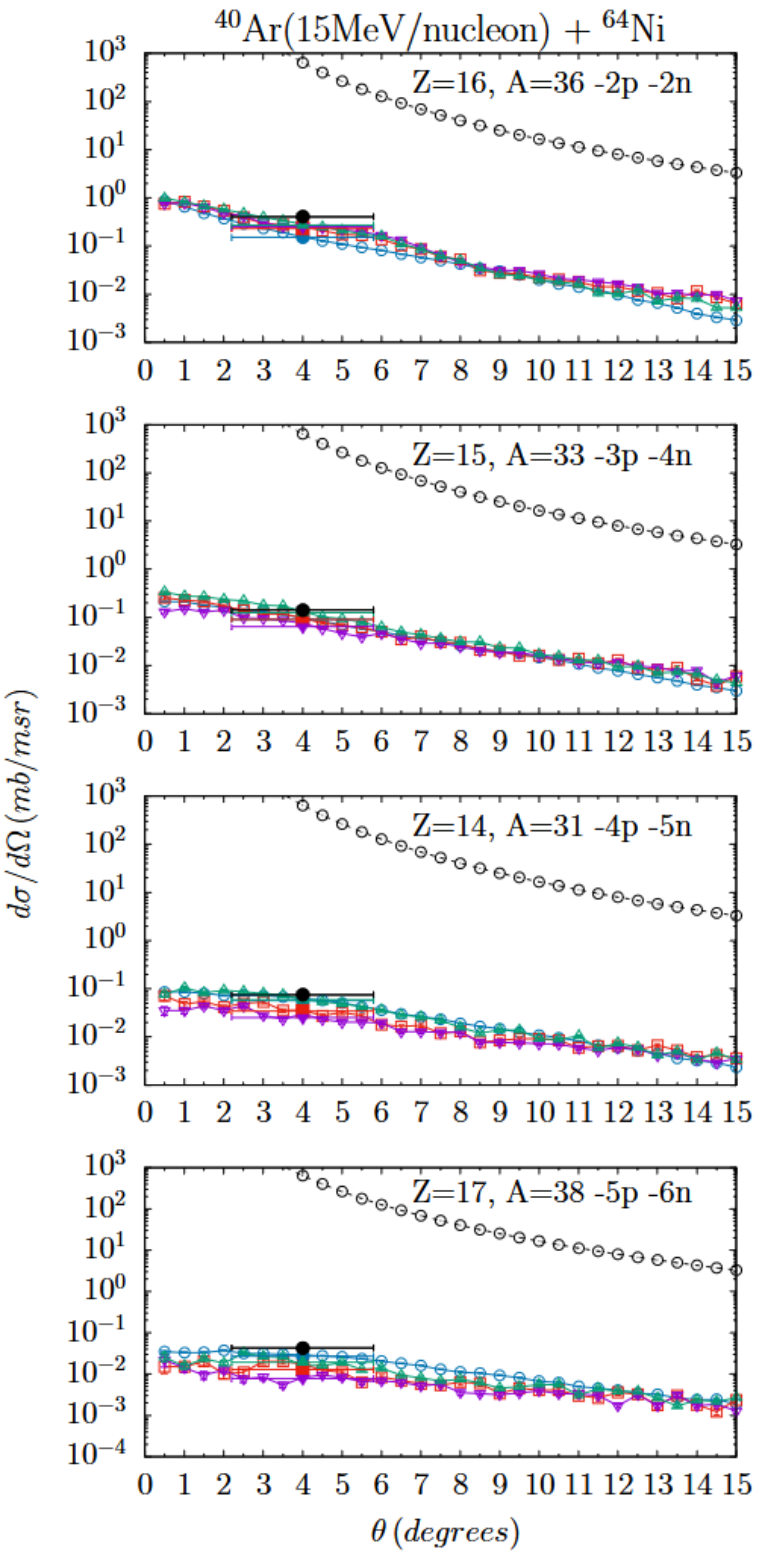

Figure 59: Angular distributions of projectile-like fragments for peak isotope channels (16 – 13). Black circles: Rutherford scattering. Black points: Experimental data. Blue circles: DIT calculation. Red squares: CoMD calculation, with isyn = 2. Green triangles: CoMD calculations, with isyn = 1. Purple inverse triangles: CoMD calculation, with isyn = 3.

5.4 Total Excitation Energy Distributions

Furthering our analysis on the channels of interest we explore the behavior of total excitation energy distributions. In these figures the x-axis represent the total excitation energy of the quasi-projectile and quasi-target system and in the y-axis the differential cross section with respect to solid angle, dΩ and energy, dE in units, mb/msr·MeV. The reconstructed data of the total excitation energy for neutron evaporation are represented by black points and for no evaporation by black crosses. The blue circles represent the DIT calculations, the red squares the standard CoMD calculations

In Figures 60 – 65 the green triangles represent the CoMD calculations with K = 200 MeV and the inverted purple triangles the CoMD calculations with K = 308 MeV.

In Figures 66 – 71 the green triangles represent the CoMD calculations with isyn = 1 and the inverted purple triangles represent the CoMD calculations with isyn = 3.

The comparison of the models with the experimental data shows that further research and improvement of the models is needed in order to describe the data more sufficiently. From the models used the DIT has performed better than the CoMD of any compressibility. This might be due to some difficulty of the CoMD model to account for excitation energies. Another reason for that could be the much bigger dataset of the DIT calculations, and the increase of the CoMD statistics might provide some improvement. Some convergence with the CoMD calculation with isyn = 1, stiff asymmetry potential, seem promising, but further research should be conducted as the results are preliminary.

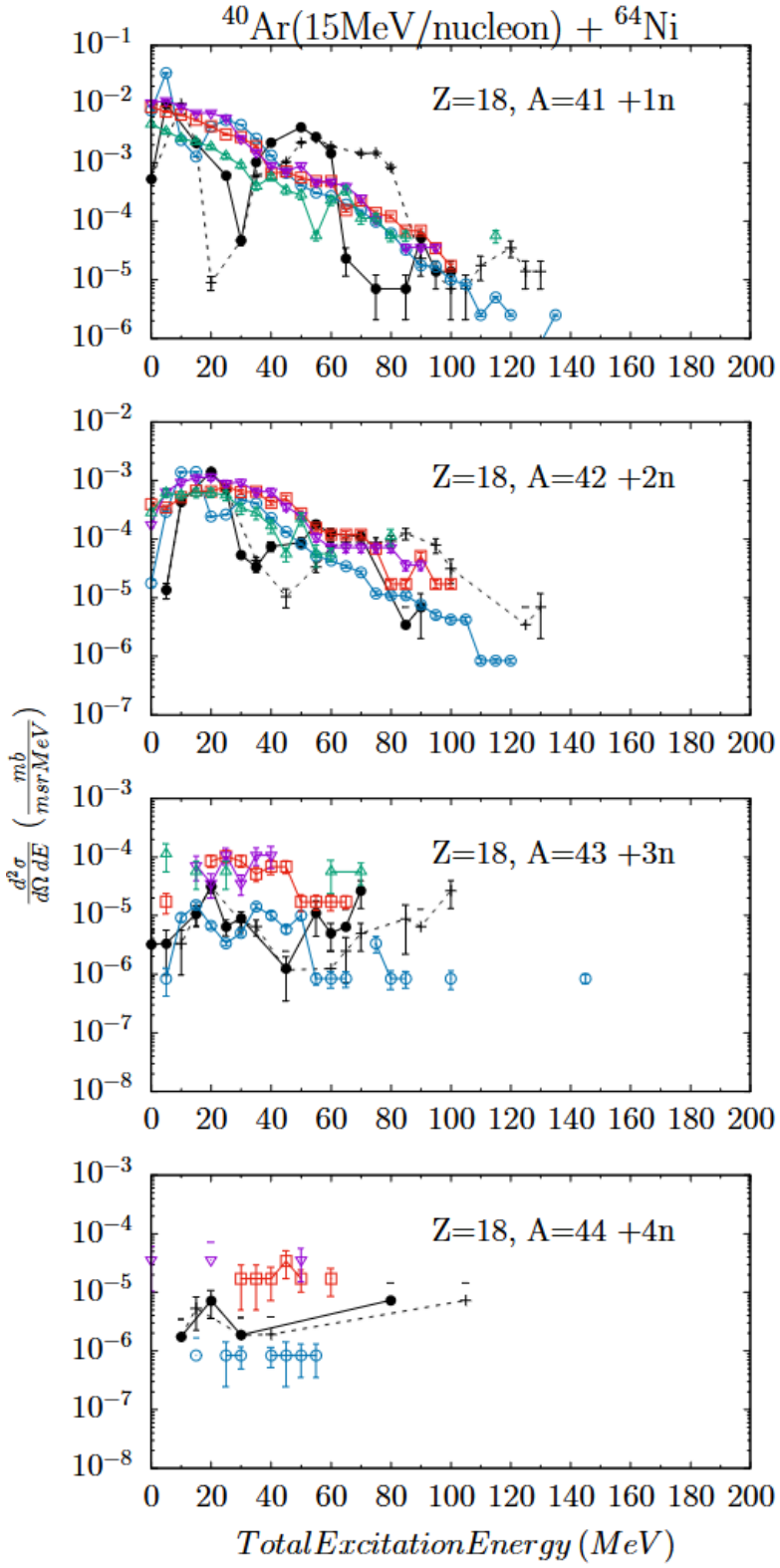

Figure 60: Total excitation energy distributions of projectile-like fragments for neutron pick-up channels. Black points: Neutron evaporation points. Black crosses: No evaporation. Blue circles: DIT calculation. Red squares: CoMD calculation, with K = 254 MeV. Green triangles: CoMD calculations, with K = 200 MeV. Purple inverse triangles: CoMD calculation, with K = 308 MeV.

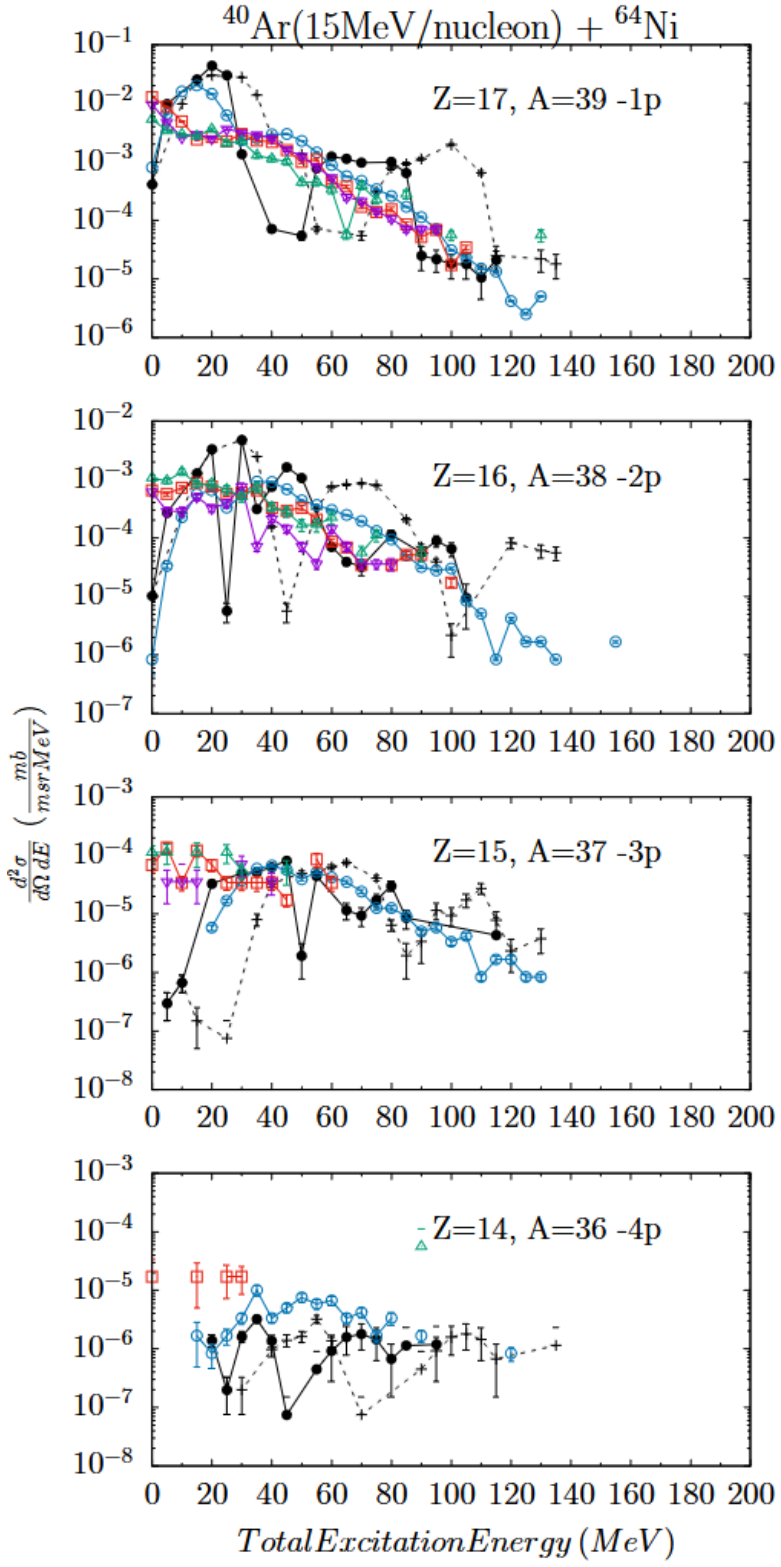

Figure 61: Total excitation energy distributions of projectile-like fragments for proton removal channels. Black points: Neutron evaporation points. Black crosses: No evaporation. Blue circles: DIT calculation. Red squares: CoMD calculation, with K = 254 MeV. Green triangles: CoMD calculations, with K = 200 MeV. Purple inverse triangles: CoMD calculation, with K = 308 MeV.

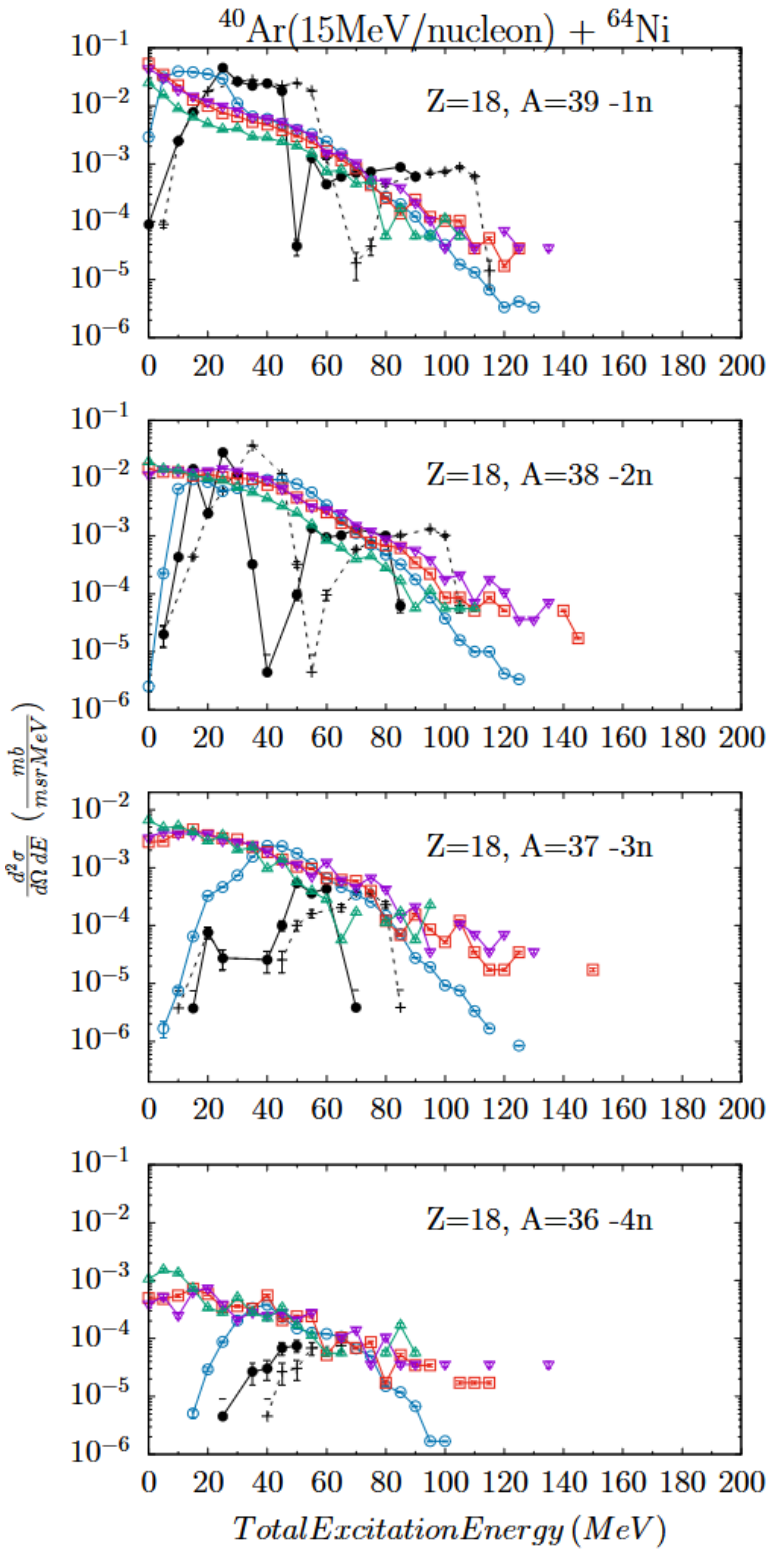

Figure 62: Total excitation energy distributions of projectile-like fragments for neutron removal channels. Black points: Neutron evaporation points. Black crosses: No evaporation. Blue circles: DIT calculation. Red squares: CoMD calculation, with K = 254 MeV. Green triangles: CoMD calculations, with K = 200 MeV. Purple inverse triangles: CoMD calculation, with K = 308 MeV.

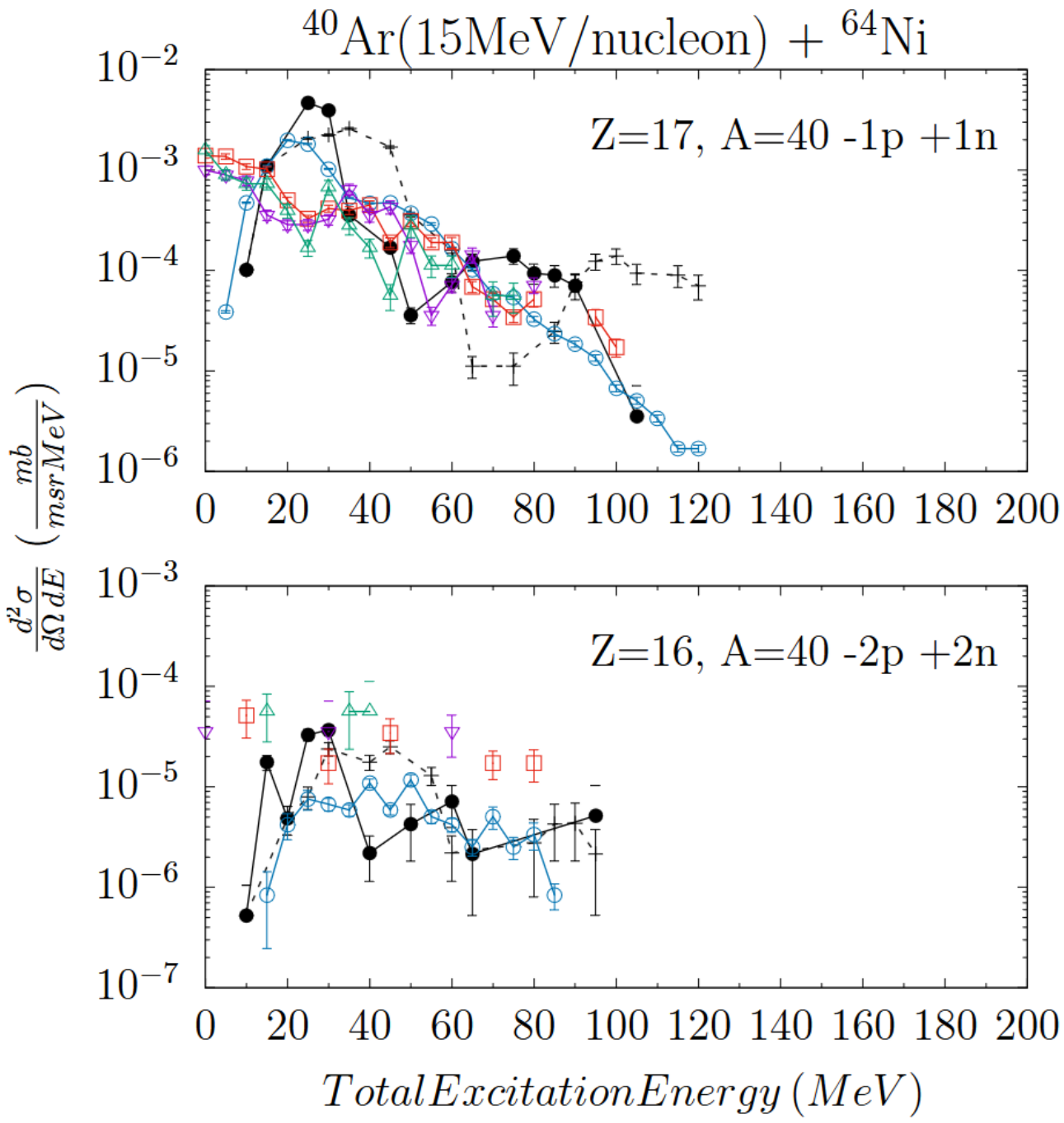

Figure 63: Total excitation energy distributions of projectile-like fragments for charge exchange channels. Black points: Neutron evaporation points. Black crosses: No evaporation. Blue circles: DIT calculation. Red squares: CoMD calculation, with K = 254 MeV. Green triangles: CoMD calculations, with K = 200 MeV. Purple inverse triangles: CoMD calculation, with K = 308 MeV.

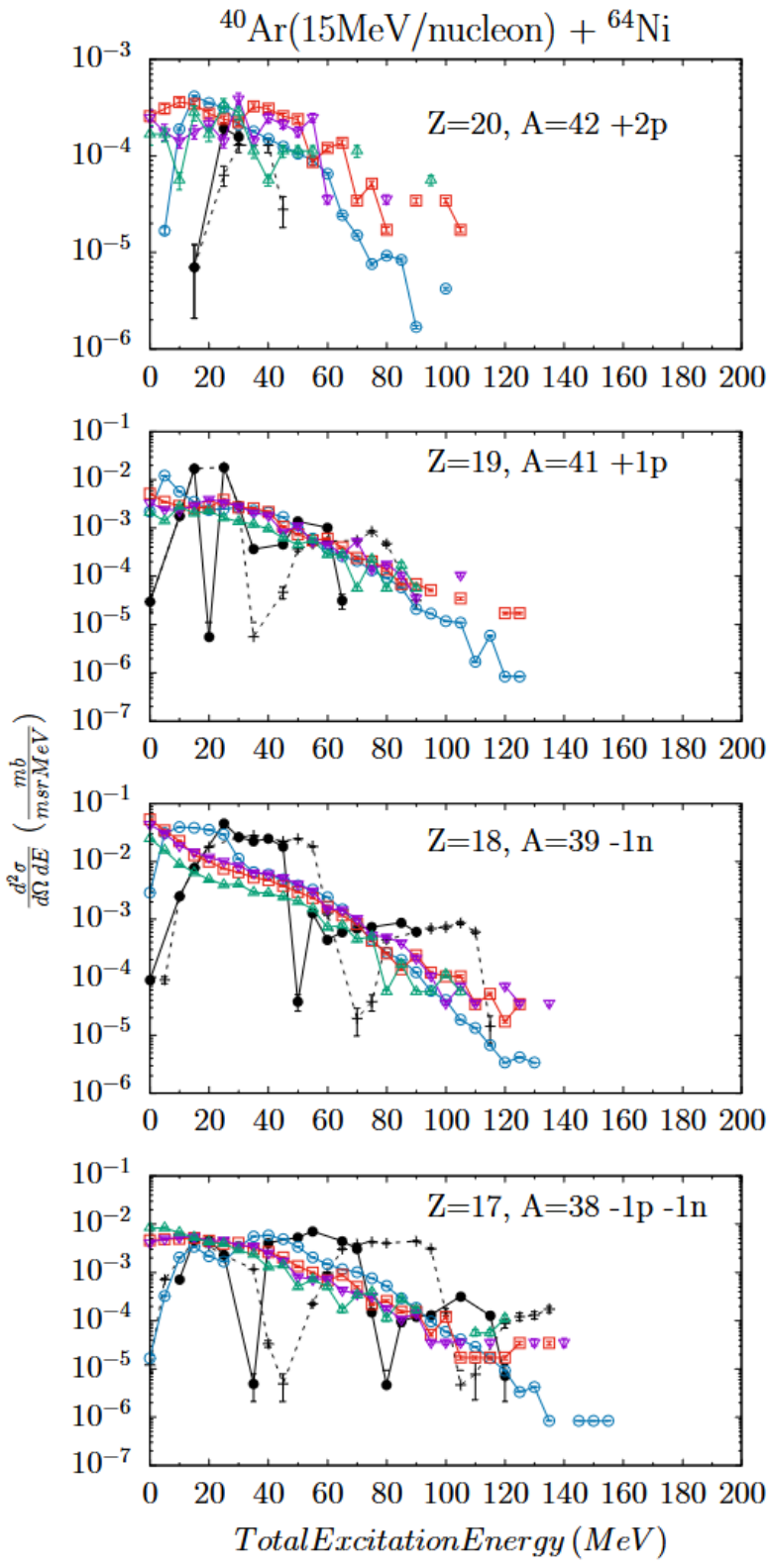

Figure 64: Total excitation energy distributions of projectile-like fragments for peak isotope channels (20 – 17). Black points: Neutron evaporation points. Black crosses: No evaporation. Blue circles: DIT calculation. Red squares: CoMD calculation, with K = 254 MeV. Green triangles: CoMD calculations, with K = 200 MeV. Purple inverse triangles: CoMD calculation, with K = 308 MeV.

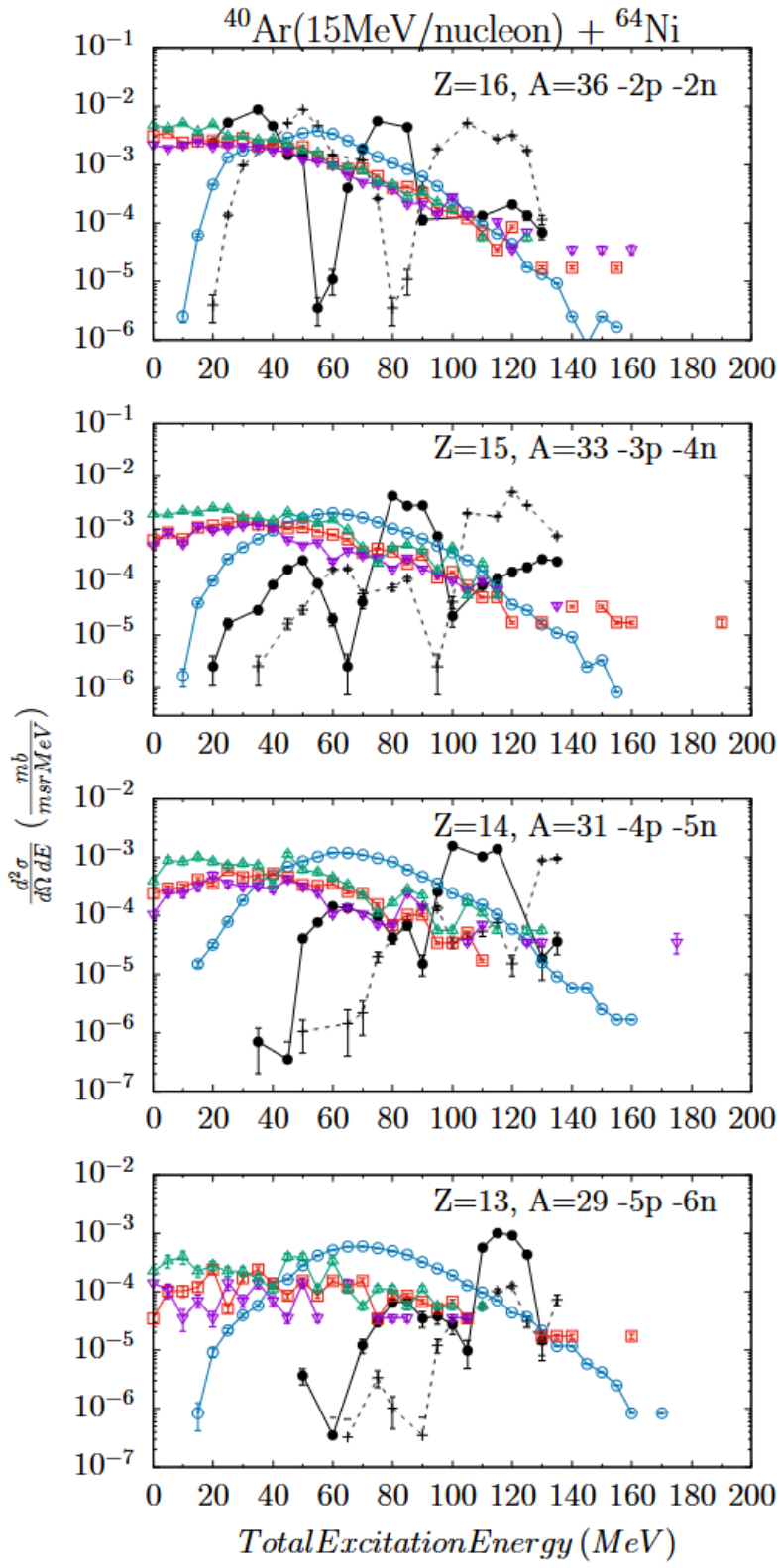

Figure 65: Total excitation energy distributions of projectile-like fragments for peak isotope channels (16 – 13). Black points: Neutron evaporation points. Black crosses: No evaporation. Blue circles: DIT calculation. Red squares: CoMD calculation, with K = 254 MeV. Green triangles: CoMD calculations, with K = 200 MeV. Purple inverse triangles: CoMD calculation, with K = 308 MeV.

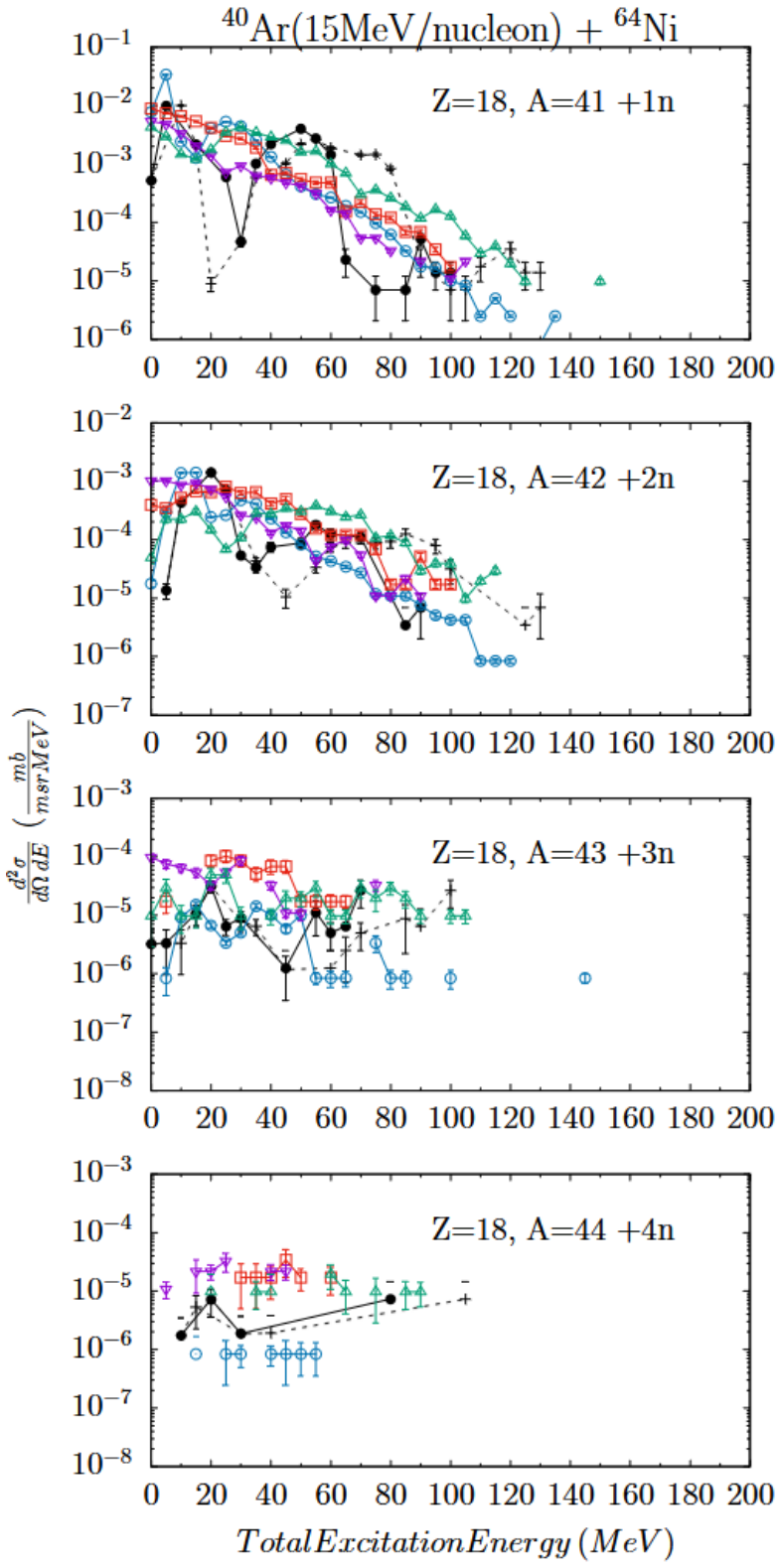

Figure 66: Total excitation energy distributions of projectile-like fragments for neutron pick-up channels. Black points: Neutron evaporation points. Black crosses: No evaporation. Blue circles: DIT calculation. Red squares: CoMD calculation, with isyn = 2. Green triangles: CoMD calculations, with isyn = 1. Purple inverse triangles: CoMD calculation, with isyn = 3.

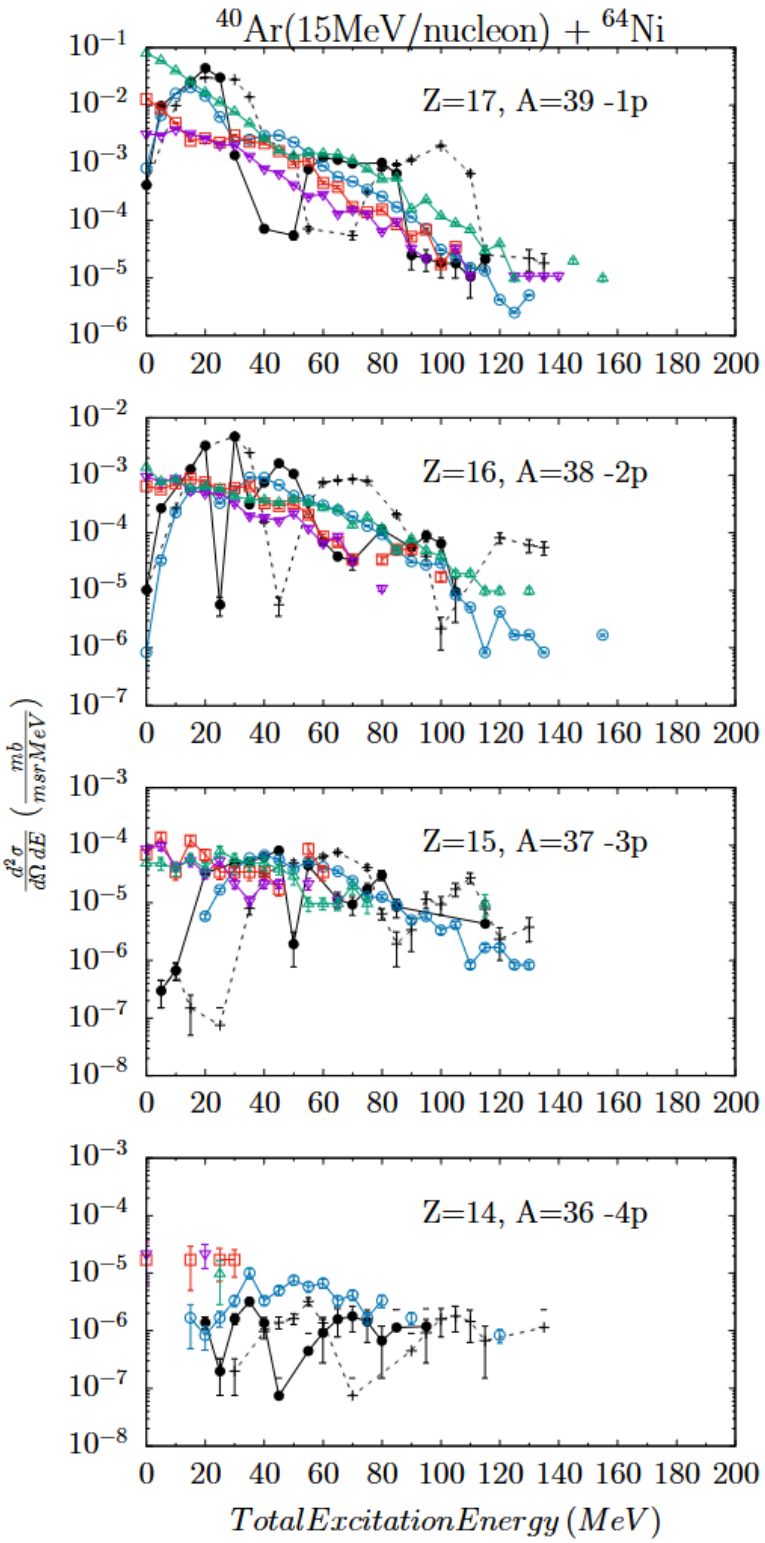

Figure 67: Total excitation energy distributions of projectile-like fragments for proton removal channels. Black points: Neutron evaporation points. Black crosses: No evaporation. Blue circles: DIT calculation. Red squares: CoMD calculation, with isyn = 2. Green triangles: CoMD calculations, with isyn = 1. Purple inverse triangles: CoMD calculation, with isyn = 3.

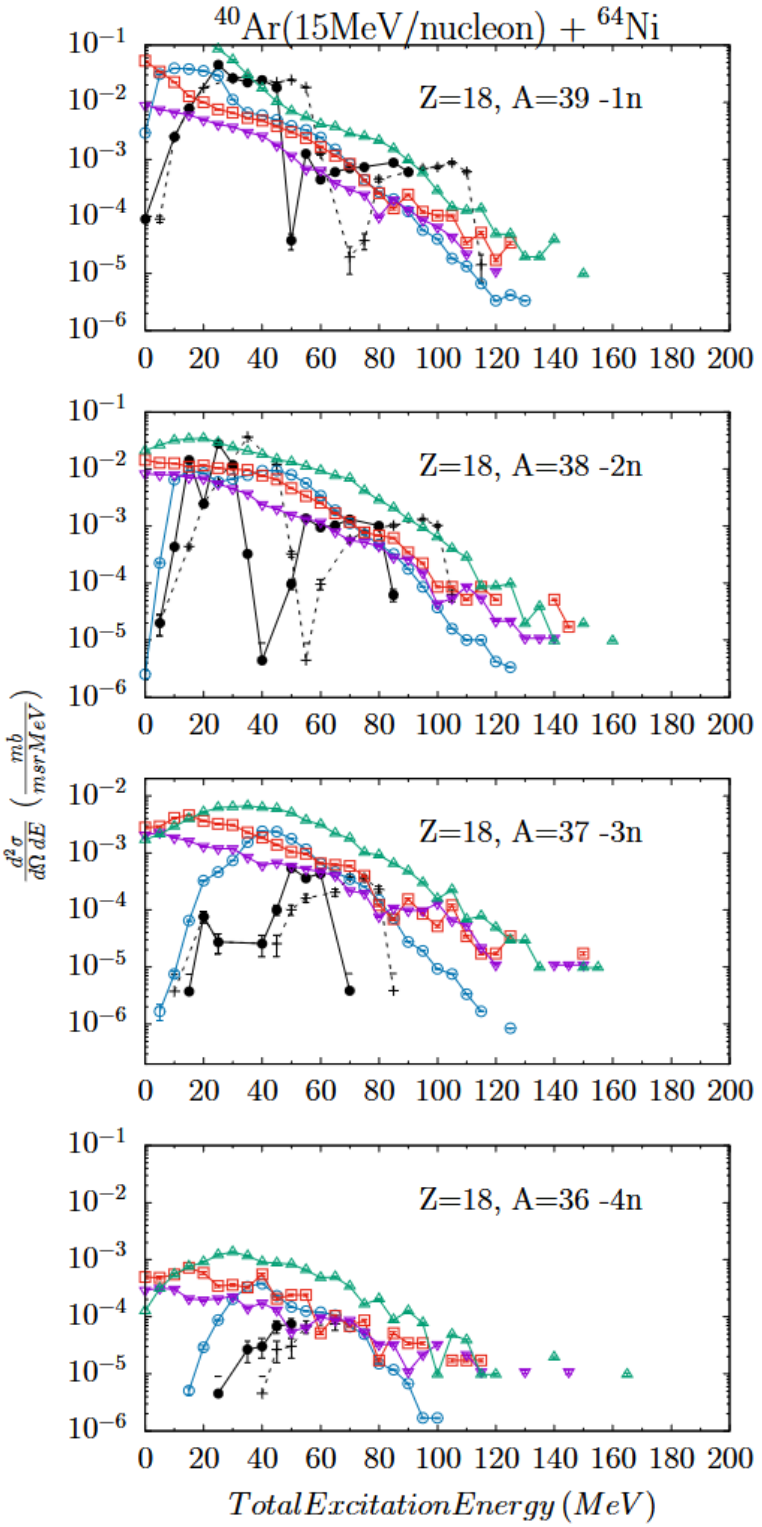

Figure 68: Total excitation energy distributions of projectile-like fragments for neutron removal channels. Black points: Neutron evaporation points. Black crosses: No evaporation. Blue circles: DIT calculation. Red squares: CoMD calculation, with isyn = 2. Green triangles: CoMD calculations, with isyn = 1. Purple inverse triangles: CoMD calculation, with isyn = 3.

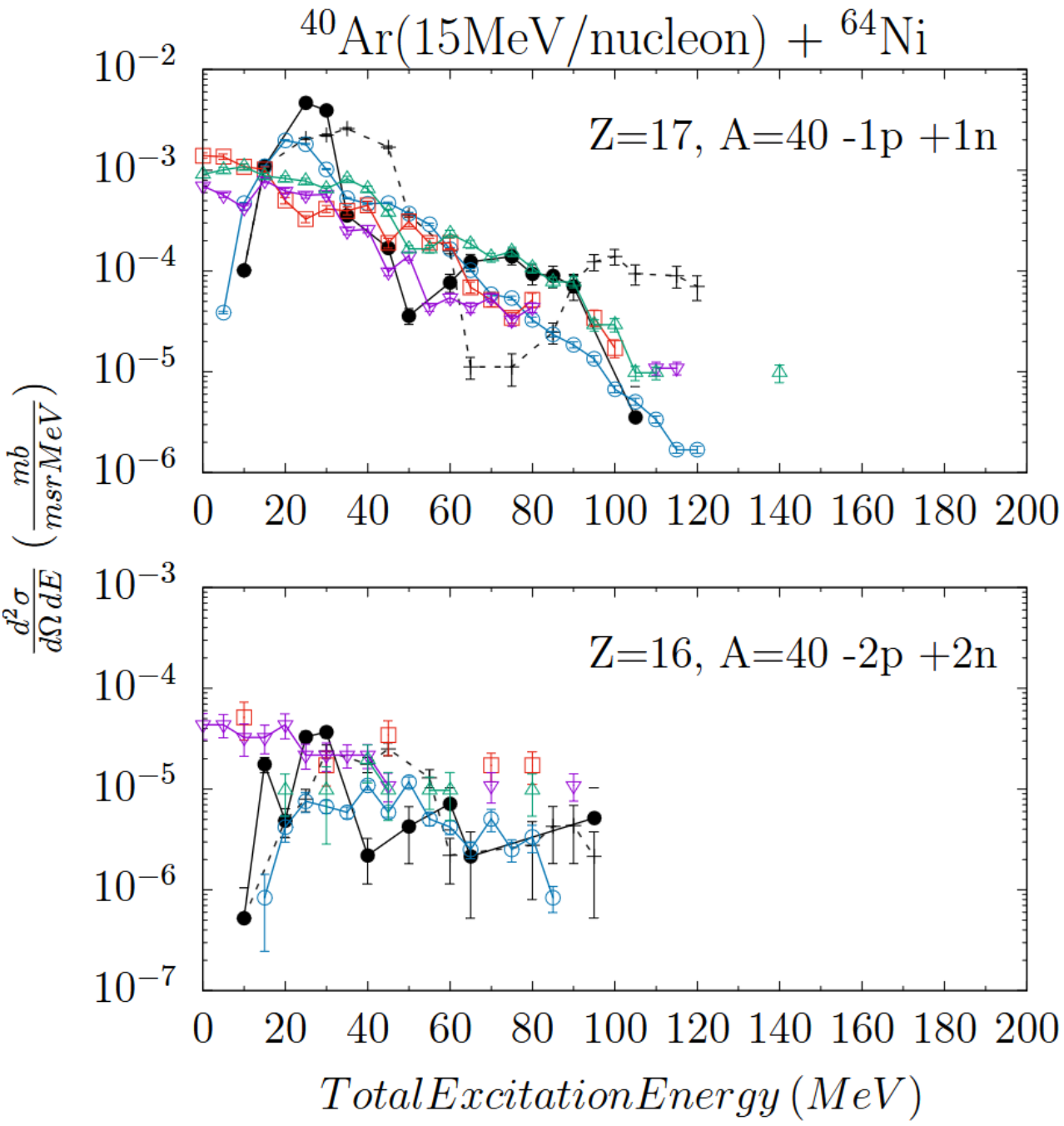

Figure 69: Total excitation energy distributions of projectile-like fragments for charge exchange channels. Black points: Neutron evaporation points. Black crosses: No evaporation. Blue circles: DIT calculation. Red squares: CoMD calculation, with isyn = 2. Green triangles: CoMD calculations, with isyn = 1. Purple inverse triangles: CoMD calculation, with isyn = 3.

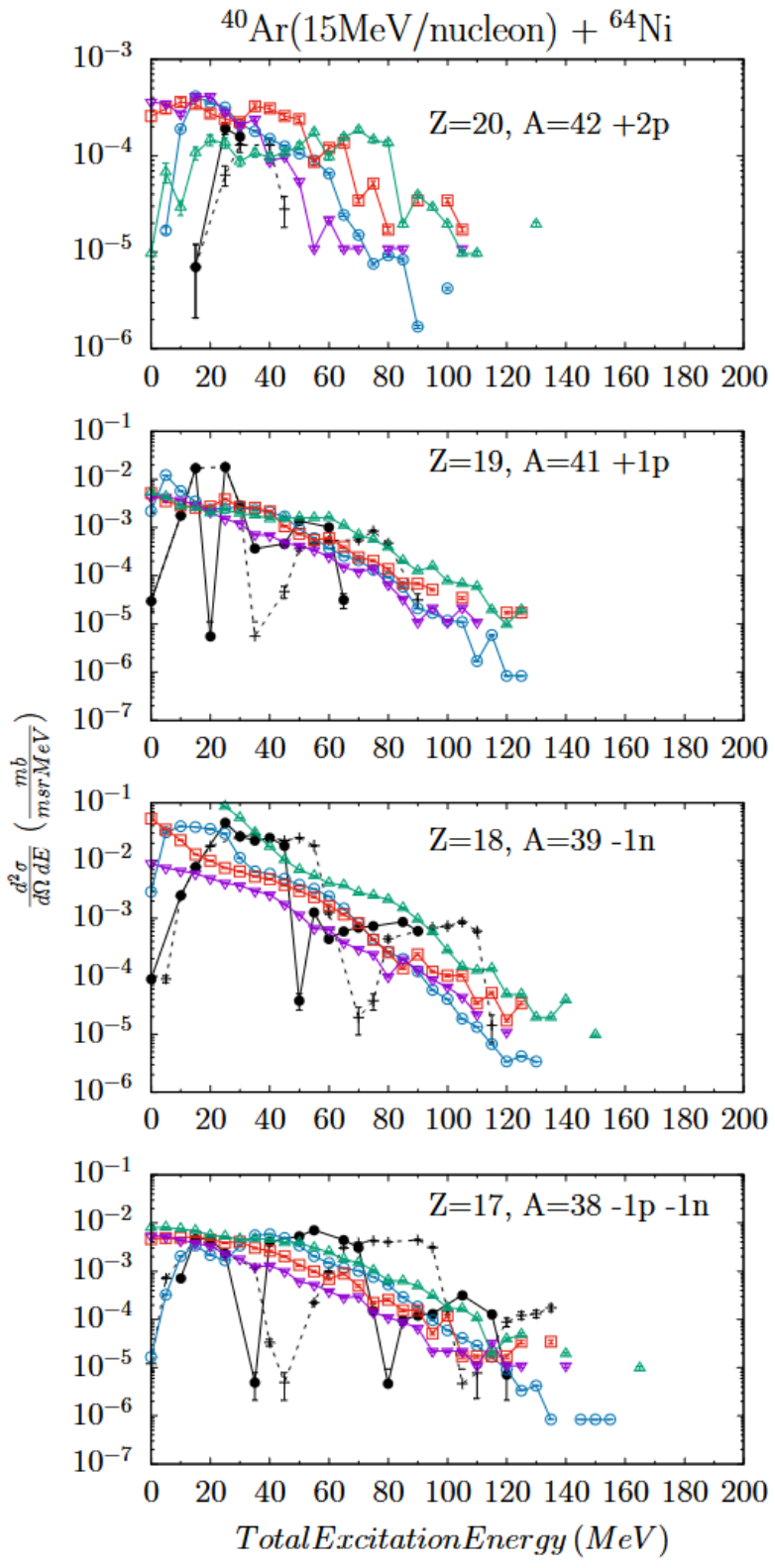

Figure 70: Total excitation energy distributions of projectile-like fragments for peak isotope channels (20 – 17). Black points: Neutron evaporation points. Black crosses: No evaporation. Blue circles: DIT calculation. Red squares: CoMD calculation, with isyn = 2. Green triangles: CoMD calculations, with isyn = 1. Purple inverse triangles: CoMD calculation, with isyn = 3.

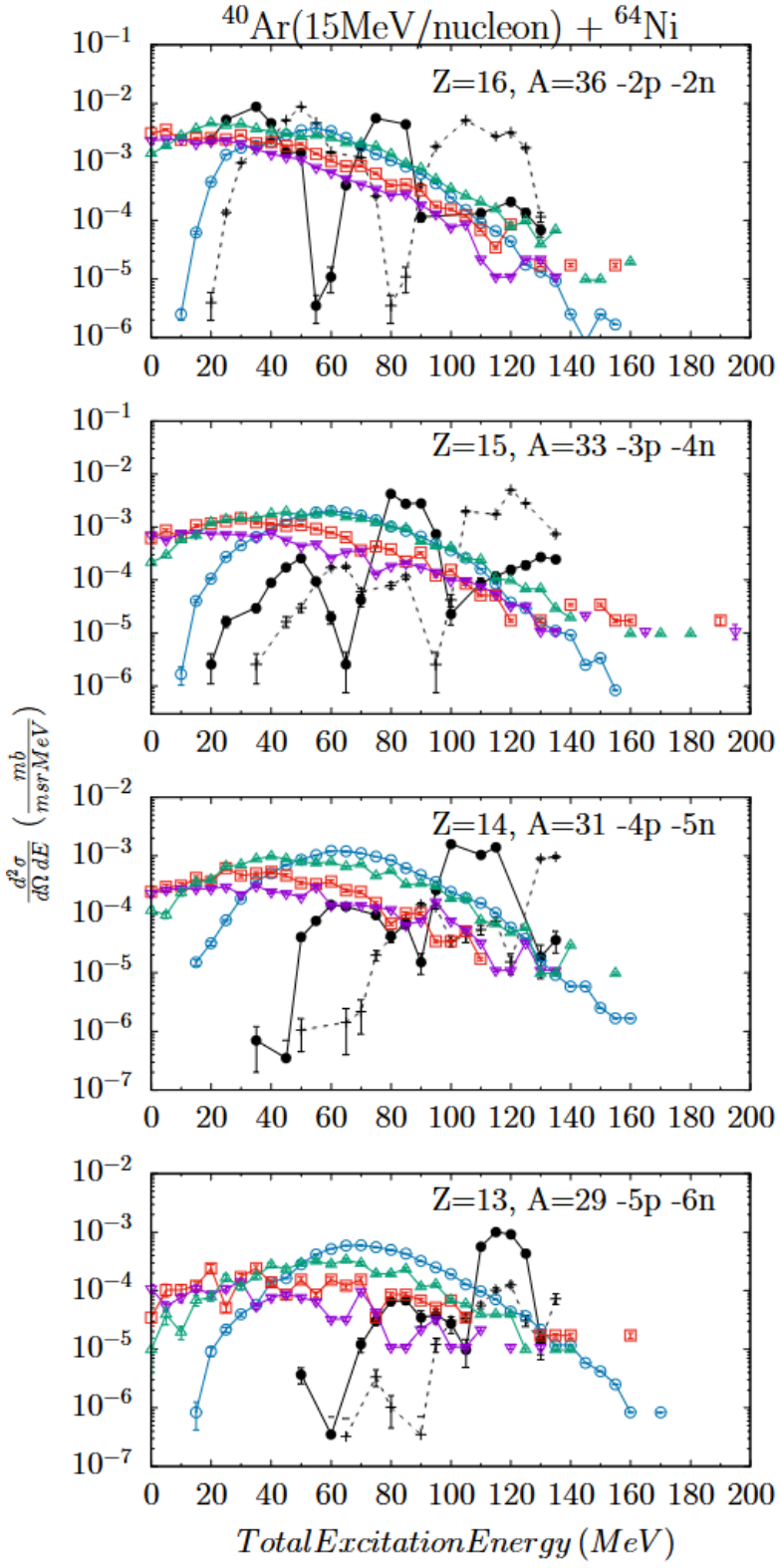

Figure 71: Total excitation energy distributions of projectile-like fragments for peak isotope channels (16 – 13). Black points: Neutron evaporation points. Black crosses: No evaporation. Blue circles: DIT calculation. Red squares: CoMD calculation, with isyn = 2. Green triangles: CoMD calculations, with isyn = 1. Purple inverse triangles: CoMD calculation, with isyn = 3.

5.5 Other Distributions

In Figure 72 we can observe the isotopic yield, the isobaric yield and the distribution of velocity versus the mass number of the quasi-projectile. The black points and the solid lines represent the experimental data for the reaction of ^{40}Ar with the ^{64}Ni target, while the black circles and dashed lines represent the experimental data for the reaction with the ^{58}Ni target. Blue lines represent the DIT calculations and red lines the CoMD. In the first two panels there are two sets of calculations, the ones in higher cross sections for the total calculations and the ones closer to the experimental data that are filtered for angular acceptance and magnetic rigidity. We observe that the DIT calculations have a slight advantage in describing the data in the first two panels, while the CoMD calculations describe better the velocity distribution.

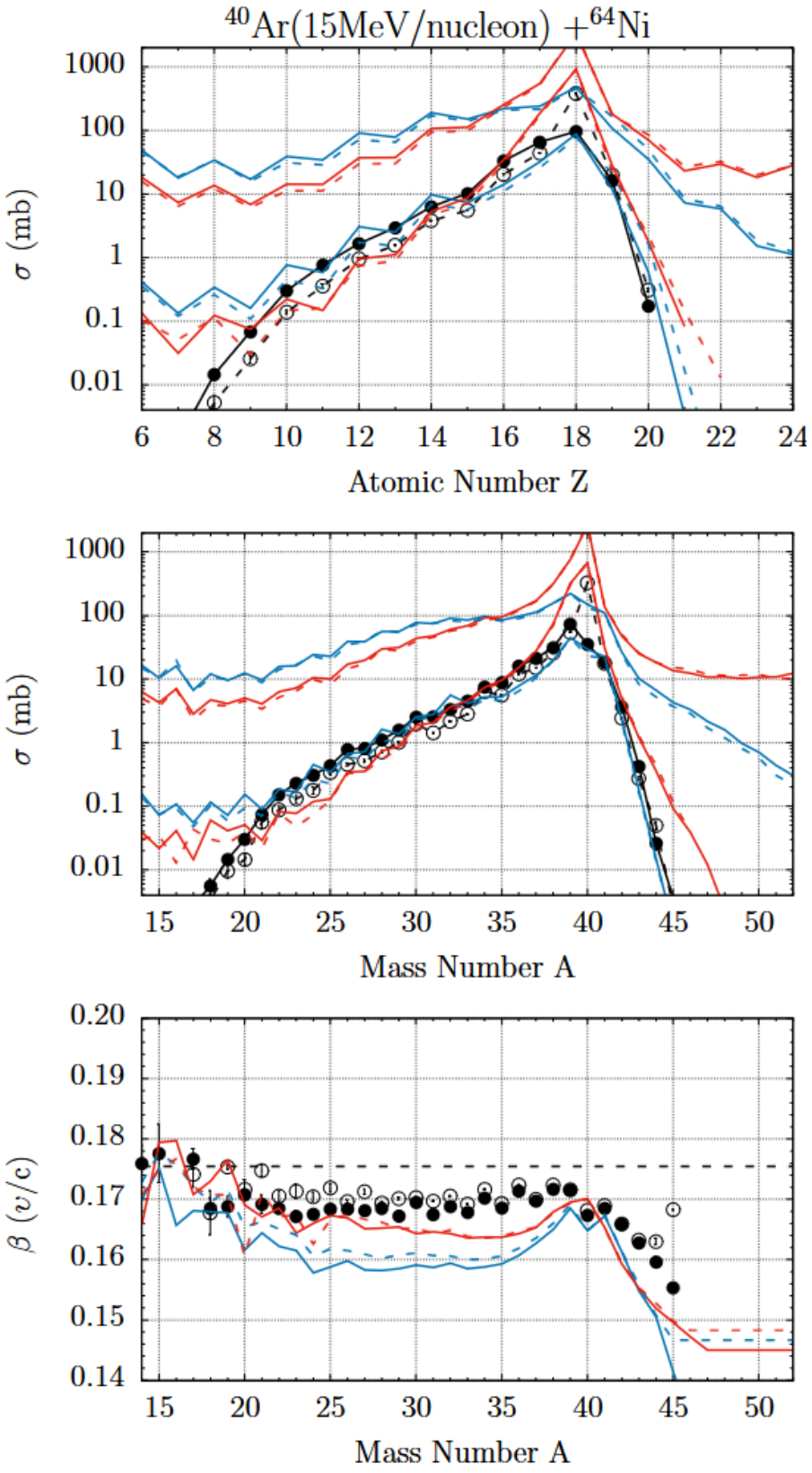

Figure 72: Isotopic yield, Isobaric yield, Velocity.

CHAPTER 6
SUMMARY AND CONCLUSIONS

This study focuses on investigating projectile-like fragments produced in the reaction of a ^{40}Ar projectile (15 MeV/nucleon) with a ^{64}Ni target in the Fermi energy regime. The experimental data analyzed in this work were originally collected by our group using the MARS spectrometer at the Cyclotron Institute of Texas A&M University, with multiple reaction channels examined.

For the dynamical stage of the ^{40}Ar (15 MeV/nucleon) + ^{64}Ni reaction, the DIT and CoMD models were employed, both followed by the GEMINI binary-decay model to simulate the de-excitation of the nuclei produced. These combined approaches were used to study the yields and momentum distributions of the projectile-like fragments.

The primary objective of this work was to modify the parameters of the CoMD model to evaluate their influence on the calculations and to enhance its ability to replicate the experimental momentum distributions. Specifically, we investigated the effects of nuclear matter compressibility, along with other parameters related to nucleon-nucleon collisions and density dependence, on the CoMD model's predictive capabilities.

Despite these efforts, further refinement of the CoMD model and a systematic examination of additional reactions within the Fermi energy range are necessary to achieve a more accurate description of the experimental data.

ACRONYMS

BE	Binding Energy
CoMD	Constrained Molecular Dynamics
DIT	Deep Inelastic Transfer
DCE	Double Charge Exchange
ISOL	Isotope Separation On-Line
PPAC	Parallel Plate Avalanche Counter
RIB	Radioactive Ion Beam
SCE	Single Charge Exchange
TOF	Time Of Flight

APPENDIX I
MASS DISTRIBUTIONS FOR ^{58}Ni TARGET

In the apendix, we present the observed mass distributions of selected projectile fragments with atomic numbers Z = 13 – 20, produced in the reaction of ^{40}Ar (15 MeV/nucleon) with ^{58}Ni. These experimental results are compared with theoretical calculations performed using the DIT and CoMD models. The diagrams display the mass number (A) on the x-axis and the total cross-section (σ, in millibarns) on the y-axis. The measured distributions within the solid angle window of $\Delta\Omega$ = 4 msr were integrated over the azimuthal angle, effectively scaling the data by a factor of 7. This allowed us to calculate the production cross-sections for each isotope in the polar angular range $\Delta\theta$ = 2.2° – 5.8°.

We can observe that the results do not diverge from the results from the reaction with the ^{64}Ni target. The datasets for following calculations are approximately 15 million for standard DIT, 1 million for standard CoMD, 0.75 million for CoMD with paulm = 80, 1 million for CoMD with isyn = 1 and 2.4 million for CoMD with isyn = 3.

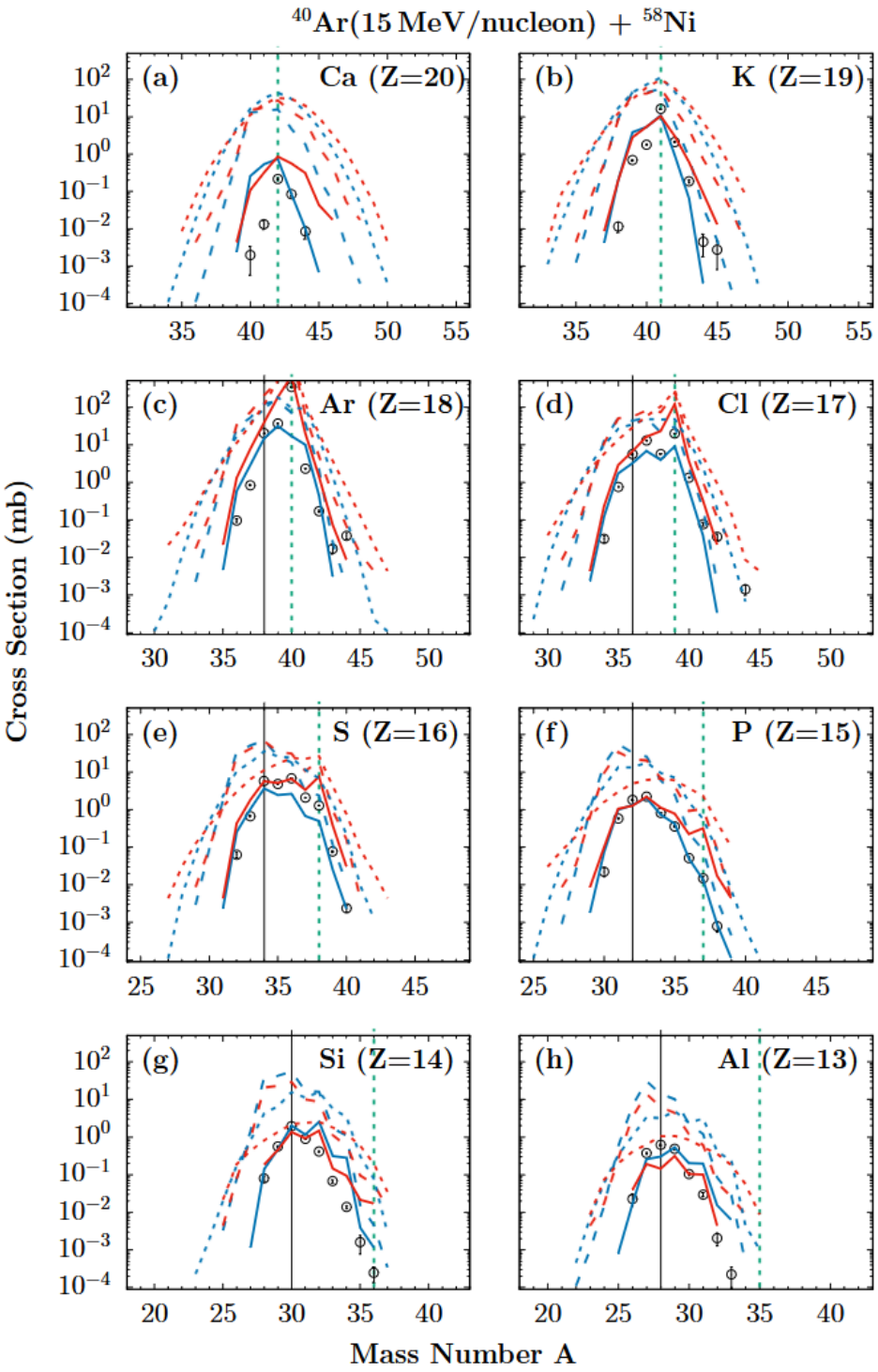

Figure 73: Production cross sections (mass distributions) of elements with Z = 13 - 20 from the reaction ^{40}Ar (15 MeV/nucleon) + ^{58}Ni. Black circles: experimental data. DIT calculations: Dotted (blue) lines: primary fragments, Dashed (blue) lines: final (cold) fragments, Full (blue) lines: final fragments filtered for angular acceptance and magnetic rigidity. CoMD calculations: Dotted (red) lines: primary fragments, Dashed (red) lines: final (cold) fragments, Full (red) lines: final fragments filtered for angular acceptance and magnetic rigidity. The vertical dashed (green) lines indicate the initiation of neutron pickup. On the left of the vertical black lines the data are obtained with incomplete magnetic rigidity coverage.

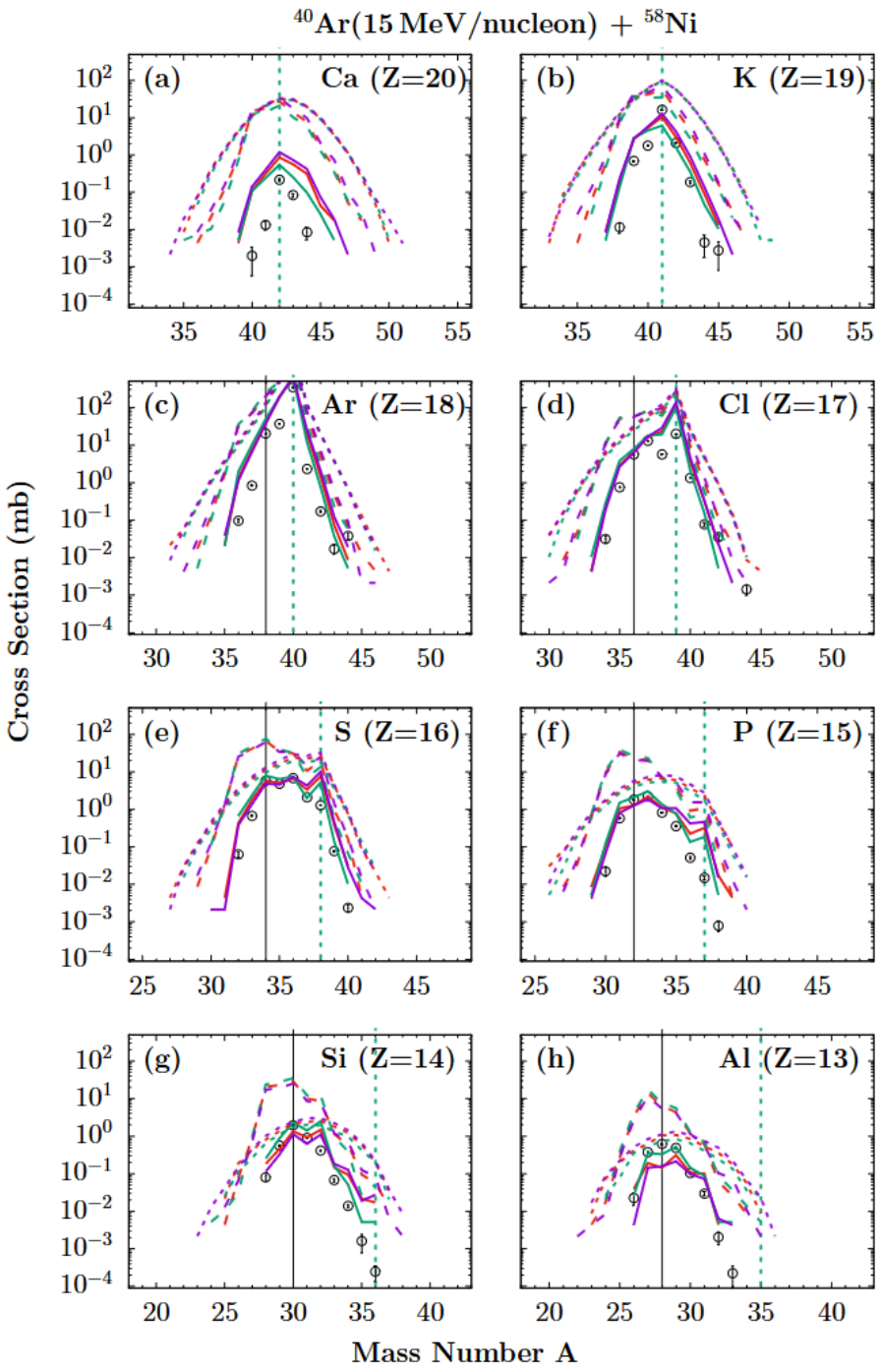

Figure 74: Production cross sections (mass distributions) of elements with Z = 13 - 20 from the reaction ^{40}Ar (15 MeV/nucleon) + ^{58}Ni. Black circles: experimental data. CoMD calculations: Dotted (red) lines: primary fragments, Dashed (red) lines: final (cold) fragments, Full (red) lines: final fragments filtered for angular acceptance and magnetic rigidity. CoMD calculations isyn = 1: Dotted (green) lines: primary fragments, Dashed (green) lines: final (cold) fragments, Full (green) lines: final fragments filtered for angular acceptance and magnetic rigidity. CoMD calculations isyn = 3: Dotted (purple) lines: primary fragments, Dashed (purple) lines: final (cold) fragments, Full (purple) lines: final fragments filtered for angular acceptance and magnetic rigidity. The vertical dashed (green) lines indicate the initiation of neutron pickup. On the left of the vertical black lines the data are obtained with incomplete magnetic rigidity coverage.

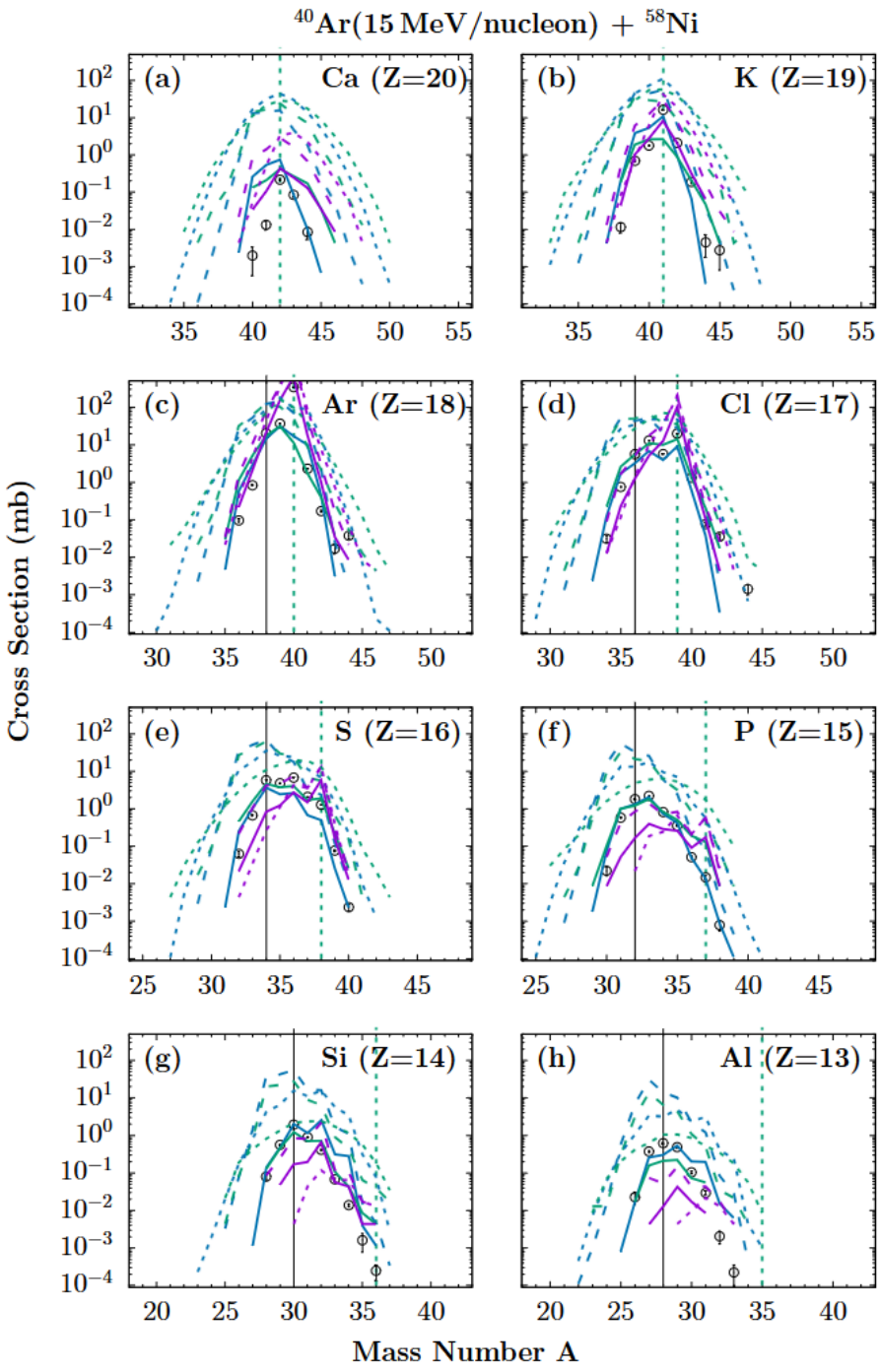

Figure 75: Production cross sections (mass distributions) of elements with Z = 13 - 20 from the reaction ^{40}Ar (15 MeV/nucleon) + ^{58}Ni. Black circles: experimental data. DIT calculations: Dotted (blue) lines: primary fragments, Dashed (blue) lines: final (cold) fragments, Full (blue) lines: final fragments filtered for angular acceptance and magnetic rigidity. CoMD calculations transfer: Dotted (green) lines: primary fragments, Dashed (green) lines: final (cold) fragments, Full (green) lines: final fragments filtered for angular acceptance and magnetic rigidity. CoMD calculations breakup: Dotted (purple) lines: primary fragments, Dashed (purple) lines: final (cold) fragments, Full (purple) lines: final fragments filtered for angular acceptance and magnetic rigidity. The vertical dashed (green) lines indicate the initiation of neutron pickup. On the left of the vertical black lines the data are obtained with incomplete magnetic rigidity coverage.

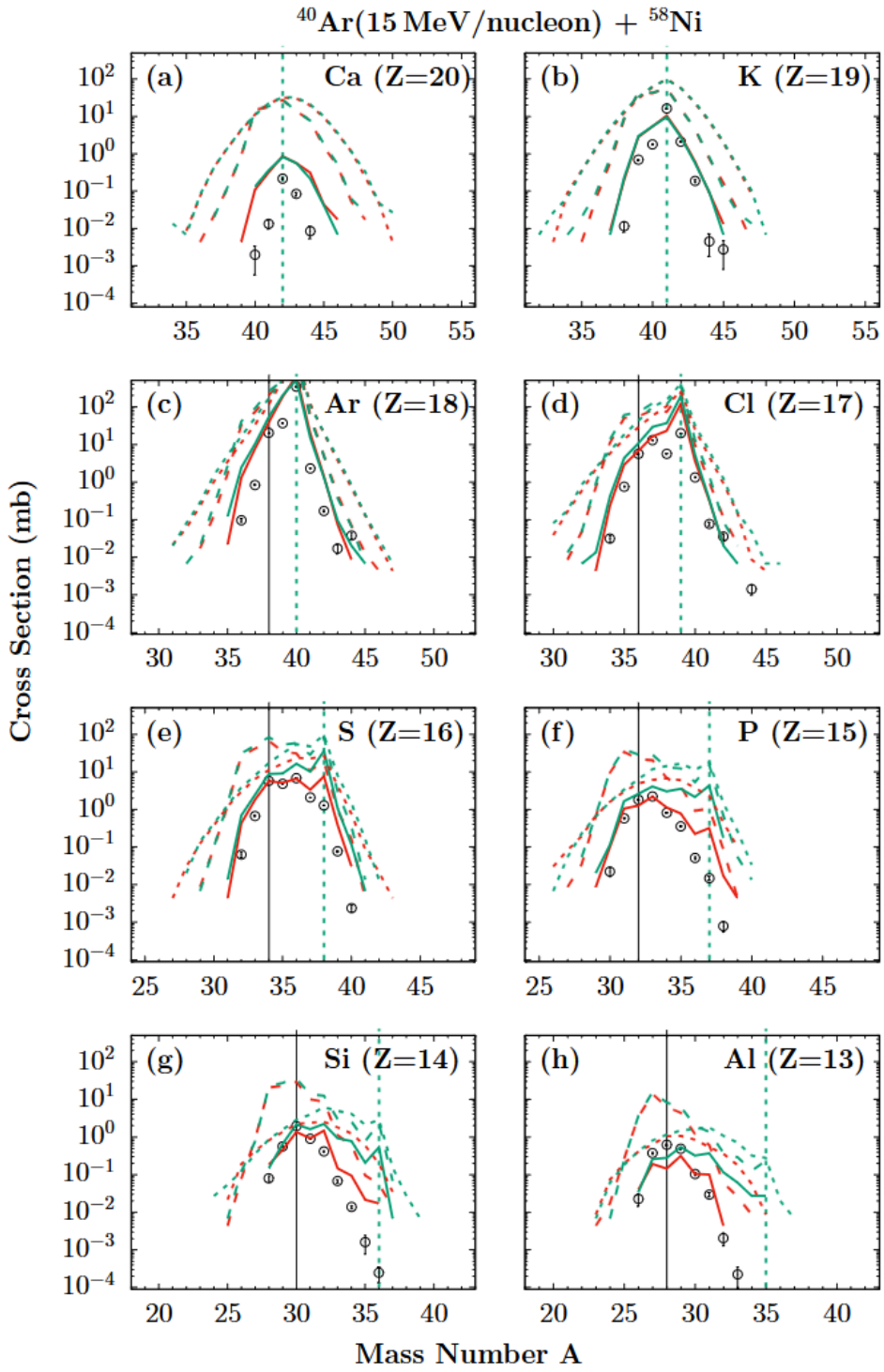

Figure 76: Production cross sections (mass distributions) of elements with Z = 13 - 20 from the reaction ^{40}Ar (15 MeV/nucleon) + ^{58}Ni. Black circles: experimental data. CoMD calculations: Dotted (red) lines: primary fragments, Dashed (red) lines: final (cold) fragments, Full (red) lines: final fragments filtered for angular acceptance and magnetic rigidity. CoMD calculations paulm = 80: Dotted (green) lines: primary fragments, Dashed (green) lines: final (cold) fragments, Full (green) lines: final fragments filtered for angular acceptance and magnetic rigidity. The vertical dashed (green) lines indicate the initiation of neutron pickup. On the left of the vertical black lines the data are obtained with incomplete magnetic rigidity coverage.

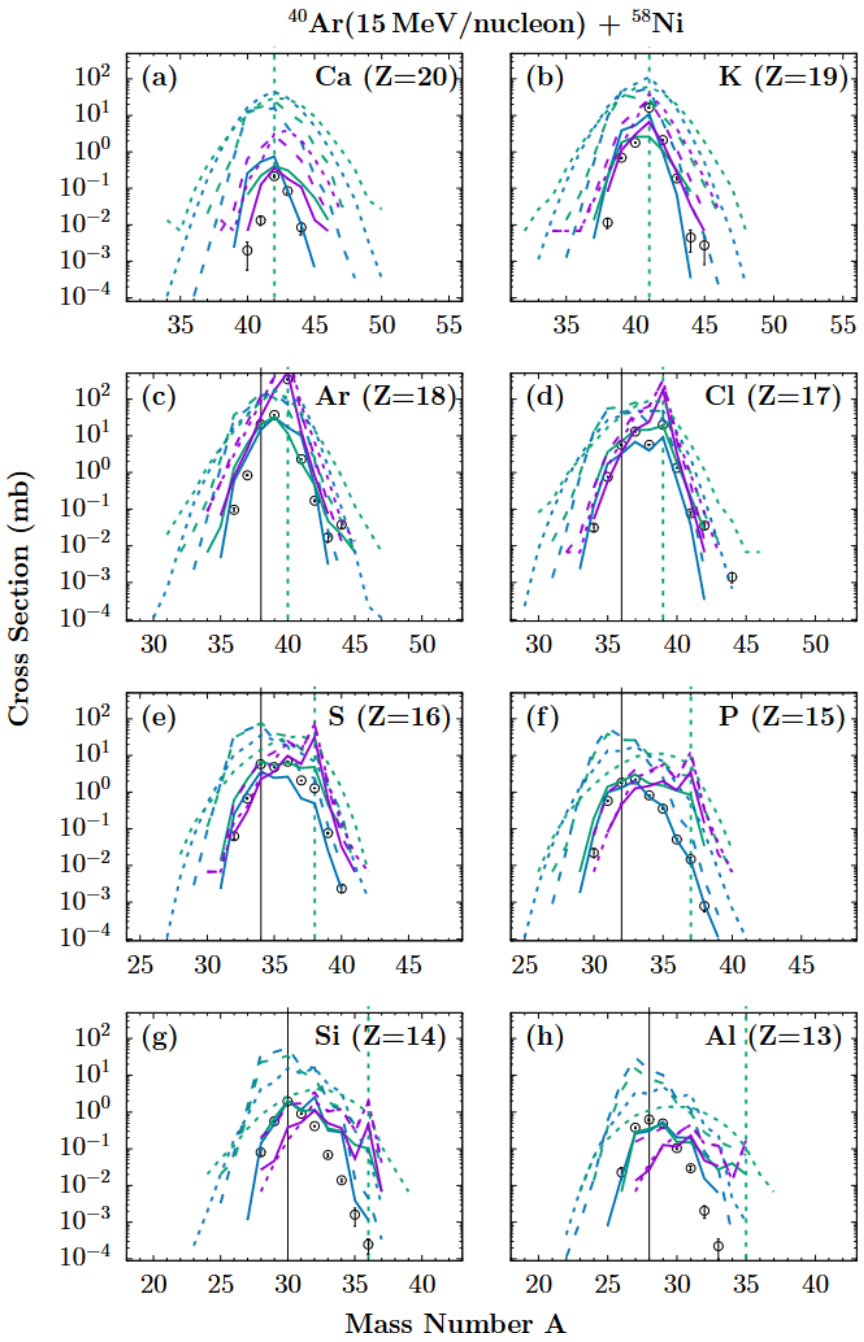

Figure 77: Production cross sections (mass distributions) of elements with Z = 13 - 20 from the reaction ^{40}Ar (15 MeV/nucleon) + ^{58}Ni. Black circles: experimental data. DIT calculations: Dotted (blue) lines: primary fragments, Dashed (blue) lines: final (cold) fragments, Full (blue) lines: final fragments filtered for angular acceptance and magnetic rigidity. CoMD calculations paulm = 80, transfer: Dotted (green) lines: primary fragments, Dashed (green) lines: final (cold) fragments, Full (green) lines: final fragments filtered for angular acceptance and magnetic rigidity. CoMD calculations paulm = 80, breakup: Dotted (purple) lines: primary fragments, Dashed (purple) lines: final (cold) fragments, Full (purple) lines: final fragments filtered for angular acceptance and magnetic rigidity. The vertical dashed (green) lines indicate the initiation of neutron pickup. On the left of the vertical black lines the data are obtained with incomplete magnetic rigidity coverage.

REFERENCES

1. Basdevant, J.-L.; Rich, J.; Spiro, M. *Fundamentals in Nuclear Physics: From Nuclear Structure to Cosmology*; Springer Science & Business Media, 2005.
2. Tang, T. L.; Kay, B. P.; Hoffman, C. R.; Schiffer, J. P.; Sharp, D. K.; Gaffney, L. P.; Freeman, S. J.; Mumpower, M. R.; Arokiaraj, A.; Baader, E. F.; Butler, P. A.; Catford, W. N.; de Angelis, G.; Flavigny, F.; Gott, M. D.; Gregor, E. T.; Konki, J.; Labiche, M.; Lazarus, I. H.; MacGregor, P. T.; Martel, I.; Page, R. D.; Podolyák, Zs.; Poleshchuk, O.; Raabe, R.; Recchia, F.; Smith, J. F.; Szwec, S. V.; Yang, J. First Exploration of Neutron Shell Structure below Lead and beyond N=126. *Phys. Rev. Lett.* **2020**, *124* (6), 062502. https://doi.org/10.1103/PhysRevLett.124.062502.
3. Langanke, K.; Wiescher, M. Nuclear Reactions and Stellar Processes. *Rep. Prog. Phys.* **2001**, *64* (12), 1657. https://doi.org/10.1088/0034-4885/64/12/202.
4. Janka, H.-Th.; Langanke, K.; Marek, A.; Martínez-Pinedo, G.; Müller, B. Theory of Core-Collapse Supernovae. *Phys. Rep.* **2007**, *442* (1), 38–74. https://doi.org/10.1016/j.physrep.2007.02.002.
5. Seeger, P.; Fowler, W.; Clayton, D. Nucleosynthesis of Heavy Elements by Neutron Capture. *Astrophys. J.* **1965**.
6. Arnould, M.; Goriely, S. Astronuclear Physics: A Tale of the Atomic Nuclei in the Skies. *Prog. Part. Nucl. Phys.* **2020**, *112*, 103766. https://doi.org/10.1016/j.ppnp.2020.103766.
7. Ericson, T. The Statistical Model and Nuclear Level Densities. *Adv. Phys.* **1960**. https://doi.org/10.1080/00018736000101239.
8. Danielewicz, P.; Lacey, R.; Lynch, W. G. Determination of the Equation of State of Dense Matter. *Science* **2002**, *298* (5598), 1592–1596. https://doi.org/10.1126/science.1078070.
9. Li, B.-A.; Chen, L.-W.; Ko, C. M. Recent Progress and New Challenges in Isospin Physics with Heavy-Ion Reactions. *Phys. Rep.* **2008**, *464* (4), 113–281. https://doi.org/10.1016/j.physrep.2008.04.005.
10. Shetty, D. V.; Yennello, S. J.; Souliotis, G. A. Density Dependence of the Symmetry Energy and the Nuclear Equation of State: A Dynamical and Statistical Model Perspective. *Phys. Rev. C* **2007**, *76* (2), 024606. https://doi.org/10.1103/PhysRevC.76.024606.
11. Blumenfeld, Y.; Nilsson, T.; Van Duppen, P. Facilities and Methods for Radioactive Ion Beam Production. *Phys. Scr.* **2013**, *2013* (T152), 014023. https://doi.org/10.1088/0031-8949/2013/T152/014023.
12. *Nuclear Binding Energy*. Physics LibreTexts. https://phys.libretexts.org/Bookshelves/University_Physics/University_Physics_(OpenStax)/University_Physics_III_-_Optics_and_Modern_Physics_(OpenStax)/10%3A__Nuclear_Physics/10.03%3A_Nuclear_Binding_Energy (accessed 2025-02-16).
13. Loveland, W. D.; Morrissey, D. J.; Seaborg, G. T. *Modern Nuclear Chemistry*; John Wiley & Sons, 2017.
14. Souliotis, G. A.; Fountas, P. N.; Veselsky, M.; Galanopoulos, S.; Kohley, Z.; McIntosh, A.; Yennello, S. J.; Bonasera, A. Isoscaling of Heavy Projectile Residues and N/Z Equilibration in Peripheral Heavy-Ion Collisions below the Fermi Energy. *Phys. Rev. C* **2014**, *90* (6), 064612. https://doi.org/10.1103/PhysRevC.90.064612.

15. Corradi, L.; Szilner, S.; Pollarolo, G.; Montanari, D.; Fioretto, E.; Stefanini, A. M.; Valiente-Dobón, J. J.; Farnea, E.; Michelagnoli, C.; Montagnoli, G.; Scarlassara, F.; Ur, C. A.; Mijatović, T.; Jelavić Malenica, D.; Soić, N.; Haas, F. Multinucleon Transfer Reactions: Present Status and Perspectives. *Nucl. Instrum. Methods Phys. Res. Sect. B Beam Interact. Mater. At.* **2013**, *317*, 743–751. https://doi.org/10.1016/j.nimb.2013.04.093.
16. Souliotis, G. A.; Veselsky, M.; Chubarian, G.; Trache, L.; Keksis, A.; Martin, E.; Shetty, D. V.; Yennello, S. J. Enhanced Production of Neutron-Rich Rare Isotopes in Peripheral Collisions at Fermi Energies. *Phys. Rev. Lett.* **2003**, *91* (2), 022701. https://doi.org/10.1103/PhysRevLett.91.022701.
17. Souliotis, G. A.; Veselsky, M.; Chubarian, G.; Trache, L.; Keksis, A.; Martin, E.; Ruangma, A.; Winchester, E.; Yennello, S. J. Enhanced Production of Neutron-Rich Rare Isotopes in the Reaction of 25 MeV/Nucleon ^{86}Kr on ^{64}Ni. *Phys. Lett. B* **2002**, *543* (3), 163–172. https://doi.org/10.1016/S0370-2693(02)02459-0.
18. Tribble, R. E.; Burch, R. H.; Gagliardi, C. A. MARS: A Momentum Achromat Recoil Spectrometer. *Nucl. Instrum. Methods Phys. Res. Sect. Accel. Spectrometers Detect. Assoc. Equip.* **1989**, *285* (3), 441–446. https://doi.org/10.1016/0168-9002(89)90215-5.
19. Souliotis, G. A.; Veselsky, M.; Galanopoulos, S.; Jandel, M.; Kohley, Z.; May, L. W.; Shetty, D. V.; Stein, B. C.; Yennello, S. J. Approaching Neutron-Rich Nuclei toward the r-Process Path in Peripheral Heavy-Ion Collisions at 15 MeV/Nucleon. *Phys. Rev. C* **2011**, *84* (6), 064607. https://doi.org/10.1103/PhysRevC.84.064607.
20. Papageorgiou, A.; Souliotis, G. A.; Tshoo, K.; Jeong, S. C.; Kang, B. H.; Kwon, Y. K.; Veselsky, M.; Yennello, S. J.; Bonasera, A. Neutron-Rich Rare Isotope Production with Stable and Radioactive Beams in the Mass Range A ∼ 40 – 60 at Beam Energy around 15 MeV/Nucleon. *J. Phys. G Nucl. Part. Phys.* **2018**, *45* (9), 095105. https://doi.org/10.1088/1361-6471/aad7df.
21. Souliotis, G. A.; Stein, B.; Veselsky, M.; Galanopoulos, S.; Keksis, A. L.; Kohley, Z.; Shetty, D. V.; Soisson, S. N.; Wuenschel, S.; Yennello, S. J. Neutron-Rich Rare Isotope Production in the Fermi Energy Domain and Application to the Texas A&M Radioactive Beam Upgrade. *Nucl. Instrum. Methods Phys. Res. Sect. B Beam Interact. Mater. At.* **2008**, *266* (19), 4692–4696. https://doi.org/10.1016/j.nimb.2008.05.118.
22. Πάκου, Α. Πειραματικές Μέθοδοι Στην Πυρηνική Φυσική. **1999**.
23. Swan, D.; Yurkon, J.; Morrissey, D. J. A Simple Two-Dimensional PPAC. *Nucl. Instrum. Methods Phys. Res. Sect. Accel. Spectrometers Detect. Assoc. Equip.* **1994**, *348* (2), 314–317. https://doi.org/10.1016/0168-9002(94)90753-6.
24. Souliotis, G. A.; Hanold, K.; Loveland, W.; Lhenry, I.; Morrissey, D. J.; Veeck, A. C.; Wozniak, G. J. Heavy Residue Formation in 20 MeV/Nucleon ^{197}Au – ^{12}C and ^{197}Au – ^{27}Al Collisions. *Phys. Rev. C* **1998**, *57* (6), 3129–3143. https://doi.org/10.1103/PhysRevC.57.3129.
25. Hubert, F.; Bimbot, R.; Gauvin, H. Range and Stopping-Power Tables for 2.5–500 MeV/Nucleon Heavy Ions in Solids. *At. Data Nucl. Data Tables* **1990**, *46* (1), 1–213. https://doi.org/10.1016/0092-640X(90)90001-Z.
26. Hubert, F.; Bimbot, R.; Gauvin, H. Semi-Empirical Formulae for Heavy Ion Stopping Powers in Solids in the Intermediate Energy Range. *Nucl. Instrum. Methods Phys.*

Res. Sect. B Beam Interact. Mater. At. **1989**, *36* (4), 357–363. https://doi.org/10.1016/0168-583X(89)90339-X.
27. Tassan-Got, L.; Stéphan, C. Deep Inelastic Transfers: A Way to Dissipate Energy and Angular Momentum for Reactions in the Fermi Energy Domain. *Nucl. Phys. A* **1991**, *524* (1), 121–140. https://doi.org/10.1016/0375-9474(91)90019-3.
28. Papa, M.; Maruyama, T.; Bonasera, A. Constrained Molecular Dynamics Approach to Fermionic Systems. *Phys. Rev. C* **2001**, *64* (2), 024612. https://doi.org/10.1103/PhysRevC.64.024612.
29. Charity, R. J.; McMahan, M. A.; Wozniak, G. J.; McDonald, R. J.; Moretto, L. G.; Sarantites, D. G.; Sobotka, L. G.; Guarino, G.; Pantaleo, A.; Fiore, L.; Gobbi, A.; Hildenbrand, K. D. Systematics of Complex Fragment Emission in Niobium-Induced Reactions. *Nucl. Phys. A* **1988**, *483* (2), 371–405. https://doi.org/10.1016/0375-9474(88)90542-8.
30. Fucito, F.; Parisi, G.; Marinari, E.; Rebbi, C. A Proposal for Monte Carlo Simulations of Fermionic Systems. *Nucl Phys B* **1980**, *180* (CERN-TH-2960), 369–377.
31. Veselsky, M.; Souliotis, G. A. Effect of Nuclear Periphery on Nucleon Transfer in Peripheral Collisions. *Nucl. Phys. A* **2006**, *765* (1), 252–261. https://doi.org/10.1016/j.nuclphysa.2005.11.001.
32. Randrup, J. Mass Transport in Nuclear Collisions. *Nucl. Phys. A* **1978**, *307* (2), 319–348. https://doi.org/10.1016/0375-9474(78)90621-8.
33. Palli, K.; Souliotis, G. A.; Depastas, T.; Dimitropoulos, I.; Fasoula, O.; Koulouris, S.; Veselsky, M.; Yennello, S. J.; Bonasera, A. Microscopic Dynamical Description of Multinucleon Transfer in ^{40}Ar Induced Peripheral Collisions at 15 MeV/Nucleon. *EPJ Web Conf.* **2021**, *252*, 07002. https://doi.org/10.1051/epjconf/202125207002.
34. Vonta, N.; Souliotis, G. A.; Veselsky, M.; Bonasera, A. Microscopic Dynamical Description of Proton-Induced Fission with the Constrained Molecular Dynamics Model. *Phys. Rev. C* **2015**, *92* (2), 024616. https://doi.org/10.1103/PhysRevC.92.024616.
35. Papa, M.; Giuliani, G.; Bonasera, A. Constrained Molecular Dynamics II: An *N*-Body Approach to Nuclear Systems. *J. Comput. Phys.* **2005**, *208* (2), 403–415. https://doi.org/10.1016/j.jcp.2005.02.032.
36. Papa, M. Many-Body Correlations in Semiclassical Molecular Dynamics and Skyrme Forces for Symmetric Nuclear Matter. *J. Phys. Conf. Ser.* **2013**, *420* (1), 012082. https://doi.org/10.1088/1742-6596/420/1/012082.
37. Bonasera, A.; Gulminelli, F.; Molitoris, J. The Boltzmann Equation at the Borderline. A Decade of Monte Carlo Simulations of a Quantum Kinetic Equation. *Phys. Rep.* **1994**, *243* (1), 1–124. https://doi.org/10.1016/0370-1573(94)90108-2.
38. Charity, R. J. Systematic Description of Evaporation Spectra for Light and Heavy Compound Nuclei. *Phys. Rev. C* **2010**, *82* (1), 014610. https://doi.org/10.1103/PhysRevC.82.014610.
39. Kwan, E. *Production of Nuclei near the Neutron Drip-Line by Projectile Fragmentation*; Michigan State University. Department of Physics and Astronomy, 2006.
40. Kwan, E.; Morrissey, D. J.; Davies, D. A.; Steiner, M.; Sumithrarachchi, C. S.; Weissman, L. Systematic Studies of Light Neutron-Rich Nuclei Produced via the

Fragmentation of ^{40}Ar. *Phys. Rev. C* **2012**, *86* (1), 014612. https://doi.org/10.1103/PhysRevC.86.014612.
41. Klimo, J.; Veselsky, M.; Souliotis, G. A.; Bonasera, A. Simulation of Fusion and Quasi-Fission in Nuclear Reactions Leading to Production of Superheavy Elements Using the Constrained Molecular Dynamics Model. *Nucl. Phys. A* **2019**, *992*, 121640. https://doi.org/10.1016/j.nuclphysa.2019.121640.
42. Wang, Y.; Guo, C.; Li, Q.; Li, Z.; Su, J.; Zhang, H. Influence of Differential Elastic Nucleon-Nucleon Cross Section on Stopping and Collective Flow in Heavy-Ion Collisions at Intermediate Energies. *Phys. Rev. C* **2016**, *94* (2), 024608. https://doi.org/10.1103/PhysRevC.94.024608.
43. Agodi, C.; Giuliani, G.; Cappuzzello, F.; Bonasera, A.; Carbone, D.; Cavallaro, M.; Foti, A.; Linares, R.; Santagati, G. Analysis of Pairing Correlations in Neutron Transfer Reactions and Comparison to the Constrained Molecular Dynamics Model. *Phys. Rev. C* **2018**, *97* (3), 034616. https://doi.org/10.1103/PhysRevC.97.034616.